

AD-A114 869

NATIONAL BUREAU OF STANDARDS WASHINGTON DC
THERMODYNAMICS OF HIGH TEMPERATURE MATERIALS. (U)
SEP 81 S ABRAMOWITZ, A CEZAIIRLIYAN, F MIES

F/G 20/13

AFOSR-ISSA-81-00012

UNCLASSIFIED

AFOSR-TR-82-0380

NL

1-12

2

3

4

5

6

7

8

9

10

11

12

13

14

15

16

17

18

19

20

21

22

23

24

25

26

27

28

29

30

31

32

33

34

35

36

37

38

39

40

41

42

43

44

45

46

47

48

49

50

51

52

53

54

55

56

57

58

59

60

61

62

63

64

65

66

67

68

69

70

71

72

73

74

75

76

77

78

79

80

81

82

83

84

85

86

87

88

89

90

91

92

93

94

95

96

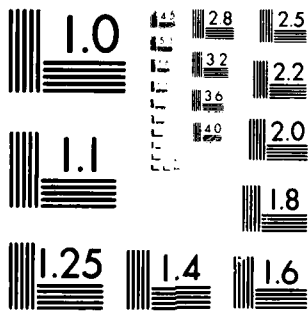
97

98

99

100

14869



MICROCOPY RESOLUTION TEST CHART
NATIONAL BUREAU OF STANDARDS-1963-A

AD A114869

DDIC FILE COPY

REPORT DOCUMENTATION PAGE		READ INSTRUCTIONS BEFORE COMPLETING FORM
1. REPORT NUMBER AFOSR-TR- 82-0380	2. GOVT ACCESSION NO. <i>AD-A114869</i>	3. RECIPIENT'S CATALOG NUMBER
4. TITLE (and Subtitle) THERMODYNAMICS OF HIGH TEMPERATURE MATERIALS		5. TYPE OF REPORT & PERIOD COVERED ANNUAL 01 OCT 81 to 01 APR 82
		6. PERFORMING ORG. REPORT NUMBER
7. AUTHOR(s) S. AB'RAMOWITZ, A. CEZA'RLIYAN, F. MIES, F. JULIENNE		8. CONTRACT OR GRANT NUMBER(s) AFOSR - ISSA-81-00012
9. PERFORMING ORGANIZATION NAME AND ADDRESS National Bureau of Standard Washington, DC 20231		10. PROGRAM ELEMENT, PROJECT, TASK AREA & WORK UNIT NUMBERS <i>6112F</i> 2306/A2
11. CONTROLLING OFFICE NAME AND ADDRESS Air Force Office of Scientific Research Bolling AFB, Washington, DC 20332		12. REPORT DATE <i>Sep 1981</i>
		13. NUMBER OF PAGES
14. MONITORING AGENCY NAME & ADDRESS (if different from Controlling Office)		15. SECURITY CLASS. (of this report) <i>Unclass</i>
		15a. DECLASSIFICATION/DOWNGRADING SCHEDULE
16. DISTRIBUTION STATEMENT (of this Report) Approved for public release; distribution unlimited.		
17. DISTRIBUTION STATEMENT (of the abstract entered in Block 20, if different from Report)		
18. SUPPLEMENTARY NOTES		
19. KEY WORDS (Continue on reverse side if necessary and identify by block number) Heat, Capacity, Electrical Resistivity, Graphite, Enthalpy Thermodynamics		
20. ABSTRACT (Continue on reverse side if necessary and identify by block number) Heat capacity and electrical resistivity of graphite have been measured in the range 2500 to 3600 K. Thermal expansion of tantalum has been measured in the range of 1500 to 3200 K. Radiance temperature (at 653 nm) of tungsten at its melting point has been determined. The enthalpy of graphite has been determined from 273 to 1173 K. The thermodynamic properties of diatomic molecules at		

**DTIC
ELECTE
MAY 25 1982
S D A**

82 05 24 028

elevated temperatures have been investigated and a formalism developed to include contributions from both the continuum states and the metastable states associated with rotational barriers. The determination of barriers to internal rotation for inorganic species has been reviewed.

1941

•

100

1. *Chlorophyll a* (Chl *a*)

DTIC

**COPY
INSPECTED**

2

100-443683

100

1997, 1998, 1999, 2000, 2001, 2002, 2003, 2004, 2005, 2006, 2007, 2008, 2009, 2010, 2011, 2012, 2013, 2014, 2015, 2016, 2017, 2018, 2019, 2020, 2021, 2022, 2023, 2024, 2025, 2026, 2027, 2028, 2029, 2030, 2031, 2032, 2033, 2034, 2035, 2036, 2037, 2038, 2039, 2040, 2041, 2042, 2043, 2044, 2045, 2046, 2047, 2048, 2049, 2050, 2051, 2052, 2053, 2054, 2055, 2056, 2057, 2058, 2059, 2060, 2061, 2062, 2063, 2064, 2065, 2066, 2067, 2068, 2069, 2070, 2071, 2072, 2073, 2074, 2075, 2076, 2077, 2078, 2079, 2080, 2081, 2082, 2083, 2084, 2085, 2086, 2087, 2088, 2089, 2090, 2091, 2092, 2093, 2094, 2095, 2096, 2097, 2098, 2099, 2100, 2101, 2102, 2103, 2104, 2105, 2106, 2107, 2108, 2109, 2110, 2111, 2112, 2113, 2114, 2115, 2116, 2117, 2118, 2119, 2120, 2121, 2122, 2123, 2124, 2125, 2126, 2127, 2128, 2129, 2130, 2131, 2132, 2133, 2134, 2135, 2136, 2137, 2138, 2139, 2140, 2141, 2142, 2143, 2144, 2145, 2146, 2147, 2148, 2149, 2150, 2151, 2152, 2153, 2154, 2155, 2156, 2157, 2158, 2159, 2160, 2161, 2162, 2163, 2164, 2165, 2166, 2167, 2168, 2169, 2170, 2171, 2172, 2173, 2174, 2175, 2176, 2177, 2178, 2179, 2180, 2181, 2182, 2183, 2184, 2185, 2186, 2187, 2188, 2189, 2190, 2191, 2192, 2193, 2194, 2195, 2196, 2197, 2198, 2199, 2200, 2201, 2202, 2203, 2204, 2205, 2206, 2207, 2208, 2209, 2210, 2211, 2212, 2213, 2214, 2215, 2216, 2217, 2218, 2219, 2220, 2221, 2222, 2223, 2224, 2225, 2226, 2227, 2228, 2229, 2230, 2231, 2232, 2233, 2234, 2235, 2236, 2237, 2238, 2239, 2240, 2241, 2242, 2243, 2244, 2245, 2246, 2247, 2248, 2249, 2250, 2251, 2252, 2253, 2254, 2255, 2256, 2257, 2258, 2259, 2260, 2261, 2262, 2263, 2264, 2265, 2266, 2267, 2268, 2269, 2270, 2271, 2272, 2273, 2274, 2275, 2276, 2277, 2278, 2279, 2280, 2281, 2282, 2283, 2284, 2285, 2286, 2287, 2288, 2289, 2290, 2291, 2292, 2293, 2294, 2295, 2296, 2297, 2298, 2299, 2300, 2301, 2302, 2303, 2304, 2305, 2306, 2307, 2308, 2309, 2310, 2311, 2312, 2313, 2314, 2315, 2316, 2317, 2318, 2319, 2320, 2321, 2322, 2323, 2324, 2325, 2326, 2327, 2328, 2329, 2330, 2331, 2332, 2333, 2334, 2335, 2336, 2337, 2338, 2339, 2340, 2341, 2342, 2343, 2344, 2345, 2346, 2347, 2348, 2349, 2350, 2351, 2352, 2353, 2354, 2355, 2356, 2357, 2358, 2359, 2360, 2361, 2362, 2363, 2364, 2365, 2366, 2367, 2368, 2369, 2370, 2371, 2372, 2373, 2374, 2375, 2376, 2377, 2378, 2379, 2380, 2381, 2382, 2383, 2384, 2385, 2386, 2387, 2388, 2389, 2390, 2391, 2392, 2393, 2394, 2395, 2396, 2397, 2398, 2399, 2400, 2401, 2402, 2403, 2404, 2405, 2406, 2407, 2408, 2409, 2410, 2411, 2412, 2413, 2414, 2415, 2416, 2417, 2418, 2419, 2420, 2421, 2422, 2423, 2424, 2425, 2426, 2427, 2428, 2429, 2430, 2431, 2432, 2433, 2434, 2435, 2436, 2437, 2438, 2439, 2440, 2441, 2442, 2443, 2444, 2445, 2446, 2447, 2448, 2449, 2450, 2451, 2452, 2453, 2454, 2455, 2456, 2457, 2458, 2459, 2460, 2461, 2462, 2463, 2464, 2465, 2466, 2467, 2468, 2469, 2470, 2471, 2472, 2473, 2474, 2475, 2476, 2477, 2478, 2479, 2480, 2481, 2482, 2483, 2484, 2485, 2486, 2487, 2488, 2489, 2490, 2491, 2492, 2493, 2494, 2495, 2496, 2497, 2498, 2499, 2500, 2501, 2502, 2503, 2504, 2505, 2506, 2507, 2508, 2509, 2510, 2511, 2512, 2513, 2514, 2515, 2516, 2517, 2518, 2519, 2520, 2521, 2522, 2523, 2524, 2525, 2526, 2527, 2528, 2529, 2530, 2531, 2532, 2533, 2534, 2535, 2536, 2537, 2538, 2539, 2540, 2541, 2542, 2543, 2544, 2545, 2546, 2547, 2548, 2549, 2550, 2551, 2552, 2553, 2554, 2555, 2556, 2557, 2558, 2559, 2560, 2561, 2562, 2563, 2564, 2565, 2566, 2567, 2568, 2569, 2570, 2571, 2572, 2573, 2574, 2575, 2576, 2577, 2578, 2579, 2580, 2581, 2582, 2583, 2584, 2585, 2586, 2587, 2588, 2589, 2590, 2591, 2592, 2593, 2594, 2595, 2596, 2597, 2598, 2599, 2600, 2601, 2602, 2603, 2604, 2605, 2606, 2607, 2608, 2609, 2610, 2611, 2612, 2613, 2614, 2615, 2616, 2617, 2618, 2619, 2620, 2621, 2622, 2623, 2624, 2625, 2626, 2627, 2628, 2629, 2630, 2631, 2632, 2633, 2634, 2635, 2636, 2637, 2638, 2639, 2640, 2641, 2642, 2643, 2644, 2645, 2646, 2647, 2648, 2649, 2650, 2651, 2652, 2653, 2654, 2655, 2656, 2657, 2658, 2659, 2660, 2661, 2662, 2663, 2664, 2665, 2666, 2667, 2668, 2669, 2670, 2671, 2672, 2673, 2674, 2675, 2676, 2677, 2678, 26

SECURITY CLASSIFICATION OF THIS PAGE (When Data Entered)

Thermodynamics of High Temperature Materials

**Annual Report for the Period
1 October 1980 - 30 September 1981**

**AIR FORCE OFFICE OF SCIENTIFIC RESEARCH
AFOSIR-ISSA - 81-00012**

**Approved for public release;
distribution unlimited.**

82 05 24 028

Abstract

Heat capacity and electrical resistivity of graphite has been measured in the range 2500 to 3600 K. Thermal expansion of tantalum has been measured in the range of 1500 to 3200 K. Radiance temperature (at 653 nm) of tungsten at its melting point has been determined. The enthalpy of graphite has been determined from 273 to 1173 K. The thermodynamic properties of diatomic molecules at elevated temperatures has been investigated and a formalism developed to include contributions from both the continuum states and the metastable states associated with rotational barriers. The determination of barriers to internal rotation for inorganic species has been reviewed. Some studies of reactions of $M(g)$ with $SO_2(g)$ using infrared matrix isolation techniques are described.

AIR FORCE OFFICE OF SCIENTIFIC RESEARCH (AFSC)
NOTICE OF TRANSMITTAL TO DTIC

This technical report has been reviewed and is
approved for public release IAW AFR 190-12.
Distribution is unlimited.

MATTHEW J. KEMPER
Chief, Technical Information Division

RESEARCH ON THERMOPHYSICAL PROPERTIES BY DYNAMIC TECHNIQUES

A. Cezairliyan, A.P. Miiller, and M.S. Morse

The progress in research on thermophysical properties by dynamic techniques has been in the following three areas:

1. Measurements of the heat capacity and the electrical resistivity of graphite in the temperature range 2500 to 3600 K.
2. Measurement of the thermal expansion of tantalum in the range 1500 to 3200 K by a transient (subsecond) interferometric technique.
3. Measurement of the radiance temperature (at 653 nm) of tungsten at its melting point.

1. Measurements of the Heat Capacity and the Electrical Resistivity of Graphite in the Temperature Range 2500 to 3600 K

Disagreements exist between the limited number of experimental results for the thermal properties of graphite above about 1500 K reported in the literature. Most of the reported measurements were performed on different grades of graphite, which complicates their evaluation and poses the question whether the differences were due to measurement errors or were really indicative of differences in the graphite grades.

As an attempt to elucidate this problem, a program was initiated for the systematic and accurate measurement of selected properties of various grades of graphite at high temperatures. The results of the first phase, namely the measurements of heat capacity, electrical resistivity and hemispherical total emittance of three grades of graphite in the temperature range 1500 to 3000 K and in vacuum were presented in an earlier publication [1]. The results on heat capacity were within 2 percent for all three grades of graphite (Poco AXM-5Q, Poco DFP-2, and pyrolytic) in the above temperature range. The high vapor pressure of graphite had limited the performance of measurements to temperatures below 3000 K.

The objective of the present investigation is to extend the measurements to temperatures above 3000 K. In order to achieve this, experiments were conducted with the specimen in a pressurized gas (argon) environment at 4 MPa (about 40 atm.). The details of the dynamic technique used for the measurements are given in the literature [2,3]. The major addition in the present work is the high pressure cell which has feed-throughs for proper electrical connections to the specimen and two optical windows for pyrometer sighting and for optical alignment. A schematic diagram of the pressure cell and the specimen support stand is shown in Fig. 1.1.

The measurements were performed on 5 tubular specimens (3 of Poco DFP-2 and 2 of Poco AXF-9Q1) fabricated from graphite rods which, according to the manufacturer, were 99.99+ pure. Three experiments were conducted on each specimen. The first experiment was performed with the

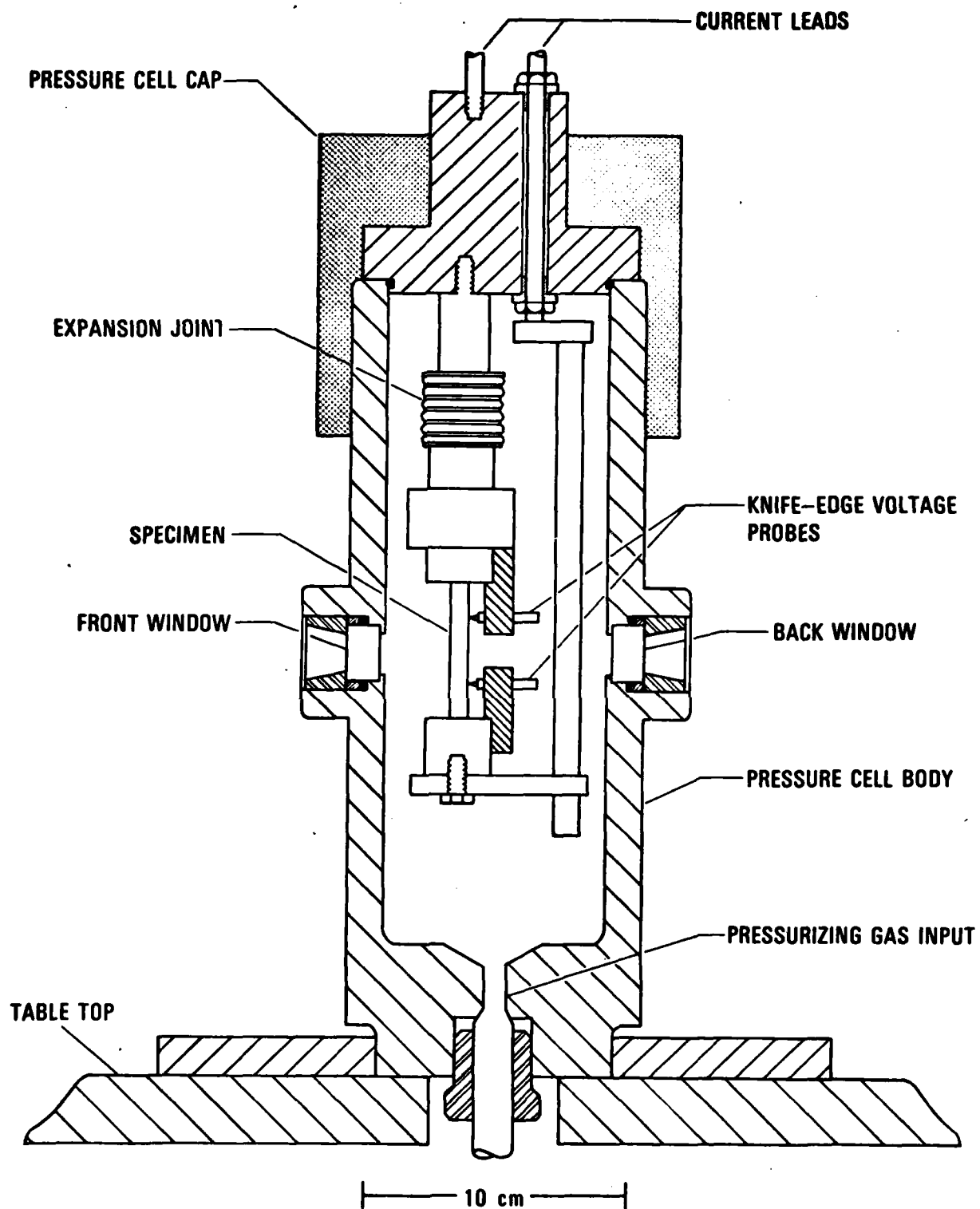


Figure 1.1. Schematic Diagram of the High-Pressure Cell and the Specimen Support Stand.

specimen in an argon atmosphere at atmospheric pressure in the temperature range 2500 to 3000 K. The second experiment, performed to determine the effect of pressure on the measurements, was conducted with the specimen in an argon environment at 4 MPa in the same temperature range. The third experiment was performed with the specimen in argon at 4 MPa in the temperature range 3100 to 3600 K. Typical heating rates for the specimens were: $1000 \text{ K}\cdot\text{s}^{-1}$ at 2500 K, $3000 \text{ K}\cdot\text{s}^{-1}$ at 3200 K, and $5800 \text{ K}\cdot\text{s}^{-1}$ at 3600 K. Duration of the current pulses was approximately 270 ms in the lower temperature range and approximately 300 ms in the higher range.

The differences in the heat capacity results among the two types of graphite were small and the data from all 15 experiments (on five specimens) were combined and fit to a polynomial function in temperature. The best fit was determined by the standard deviation was obtained with a linear function. The function for heat capacity (standard deviation: 0.7%) that represents the results in the temperature range 2500 K to 3600 K is:

$$C_p = 22.46 + 1.371 \times 10^{-3} T \quad (1)$$

where T is in K and C_p in $\text{J}\cdot\text{mol}^{-1}\cdot\text{K}^{-1}$. The heat capacity of graphite computed using Eq. (1) is given in Table 1. In the computations of heat capacity the atomic weight of graphite was taken as 12.011.

Electrical resistivity of the graphite specimens was determined from the same experiments that were used to calculate heat capacity. However, unlike heat capacity, there were differences in the electrical resistivity of the two grades of graphite. The results for each grade were separately fit to a linear function in temperature. The functions for electrical resistivity that represents the results for each grade of Poco graphite in the temperature range 2500 to 3600 K are:

$$\begin{aligned} &\text{Poco (DFP-2) graphite (standard deviation: 0.3\%)} \\ &\rho = 618.10 + 0.17349 T \quad (2) \end{aligned}$$

$$\begin{aligned} &\text{Poco (AXF-9Q1) graphite (standard deviation: 0.4\%)} \\ &\rho = 618.50 + 0.15946 T \quad (3) \end{aligned}$$

where T is in K and ρ is in $\mu\Omega\cdot\text{cm}$. The electrical resistivity of each grade of graphite computed using Eqs. (2) and (3) are given in Table 1.

Table 1

Heat capacity and electrical resistivity of graphite

Temperature (K)	Heat Capacity (J·mol ⁻¹ ·K ⁻¹)	Electrical Resistivity (μΩ·cm)	
		DFP-2	AXF-9QT
2500	25.89	1051.9	1017.2
2600	26.02	1069.2	1033.1
2700	26.16	1086.6	1049.0
2800	26.30	1103.9	1065.0
2900	26.44	1121.3	1080.9
3000	26.57	1138.6	1096.9
3100	26.71	1156.0	1112.8
3200	26.85	1173.3	1128.8
3300	26.98	1190.7	1144.7
3400	27.12	1208.0	1160.7
3500	27.26	1225.4	1176.6
3600	27.40	1242.7	1192.6

Estimates of errors in measured and computed quantities lead to the following estimates of possible maximum errors in the properties: heat capacity, 2% at 2500 K and increasing to 3% at 3600 K; electrical resistivity, 1% at 2500 K and increasing to 2% at 3600 K.

Only a limited number of experimental heat capacity results for graphite at temperatures above 2000 K were found in the literature. In addition to this, most of them were for different grades of graphite. Thus, it is questionable whether there is a common base for comparison. In order to provide continuity, results reported in the literature at temperatures above 2000 K are presented in Fig. 1.2.

The heat capacity results of the present work are in a reasonably good agreement (about 1% on the average) with those reported earlier [1] for the same grade of graphite in the overlapping temperature range 2500 to 3000 K). The smoothed results of Rasor and McClelland [4] are average values, as given by the authors, representing data on four grades of graphite (3474 D, 7087, GBH, and GBE). Their actual data have a scatter of approximately 5 percent about their smooth curve. In the temperature range 2500 to 3500 K the results of Rasor and McClelland are on the average about 3 percent higher than those of the present work. However, at temperatures above 3500 K the values reported by Rasor and McClelland increase rapidly. The results reported by Sheindlin et al. [5] are in agreement, within 1% on the average, with those reported earlier [1] in the temperature range 2000 to 2500 K. However, above 2500 K, their results indicate a sharp increase in heat capacity reaching a value of $29.6 \text{ J}\cdot\text{mol}^{-1}\cdot\text{K}^{-1}$ at 3000 K which is about 11 percent higher than the present work result and a value of $42.7 \text{ J}\cdot\text{mol}^{-1}\cdot\text{K}^{-1}$ at 3600 K which is about 56 percent higher than the present work result. The sharp increase in the heat capacity reported in the above two investigations is in contrast to the results of the present work. There is no obvious explanation for this difference, except that graphite evaporation might have affected the results reported in the literature.

Electrical resistivity of graphite is sensitive to the graphite grade and also shows considerable variations for specimens from different lots of the same grade. Thus, the only meaningful comparison of the present work results is with those measured earlier on the same grade of graphite [1]. It may be seen from Fig. 1.3 that the agreement is better than 2% in the overlapping temperature range (2500 \pm 3000 K).

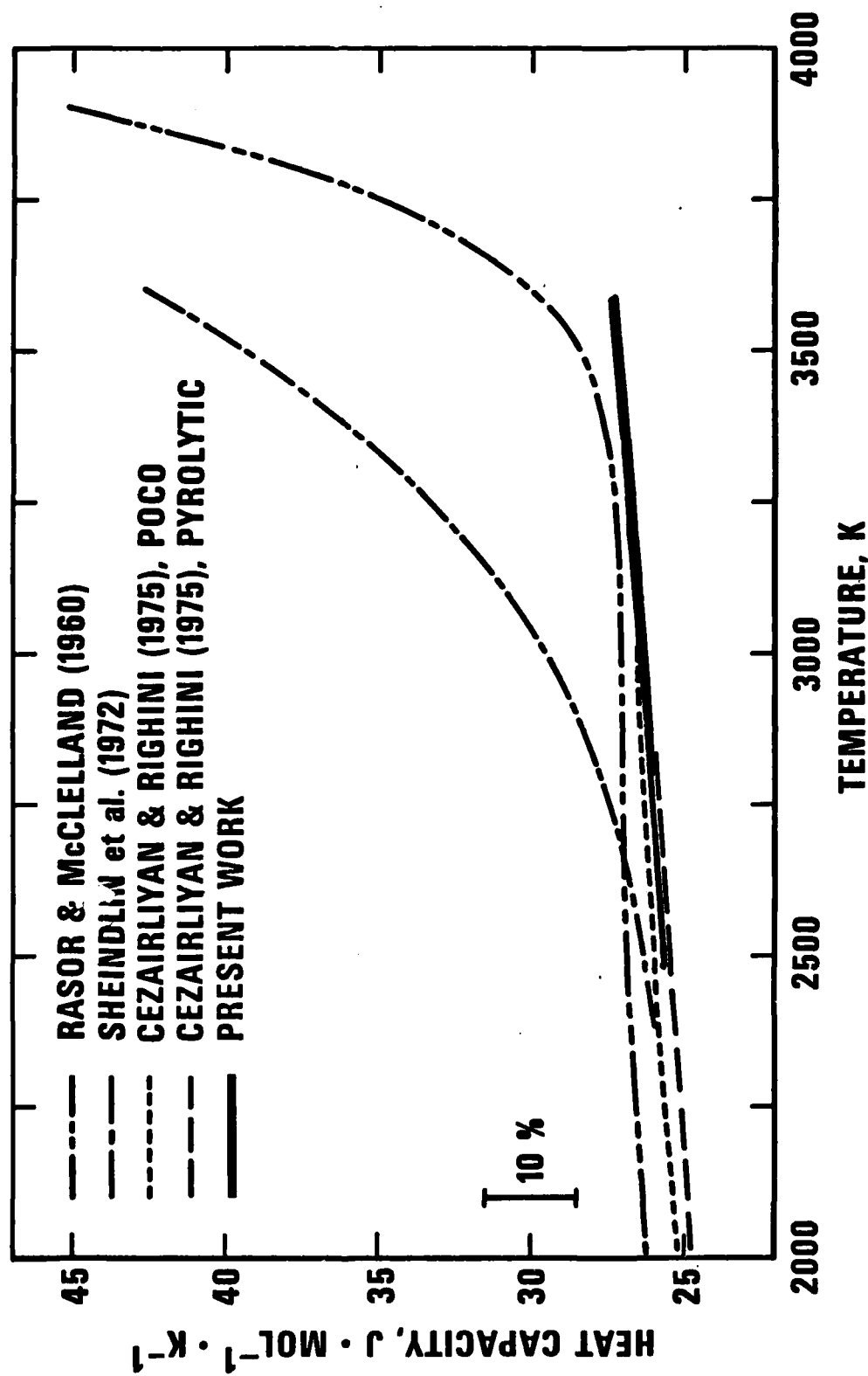


Figure 1.2. Heat Capacity of Graphite at High Temperatures Reported in the Literature.

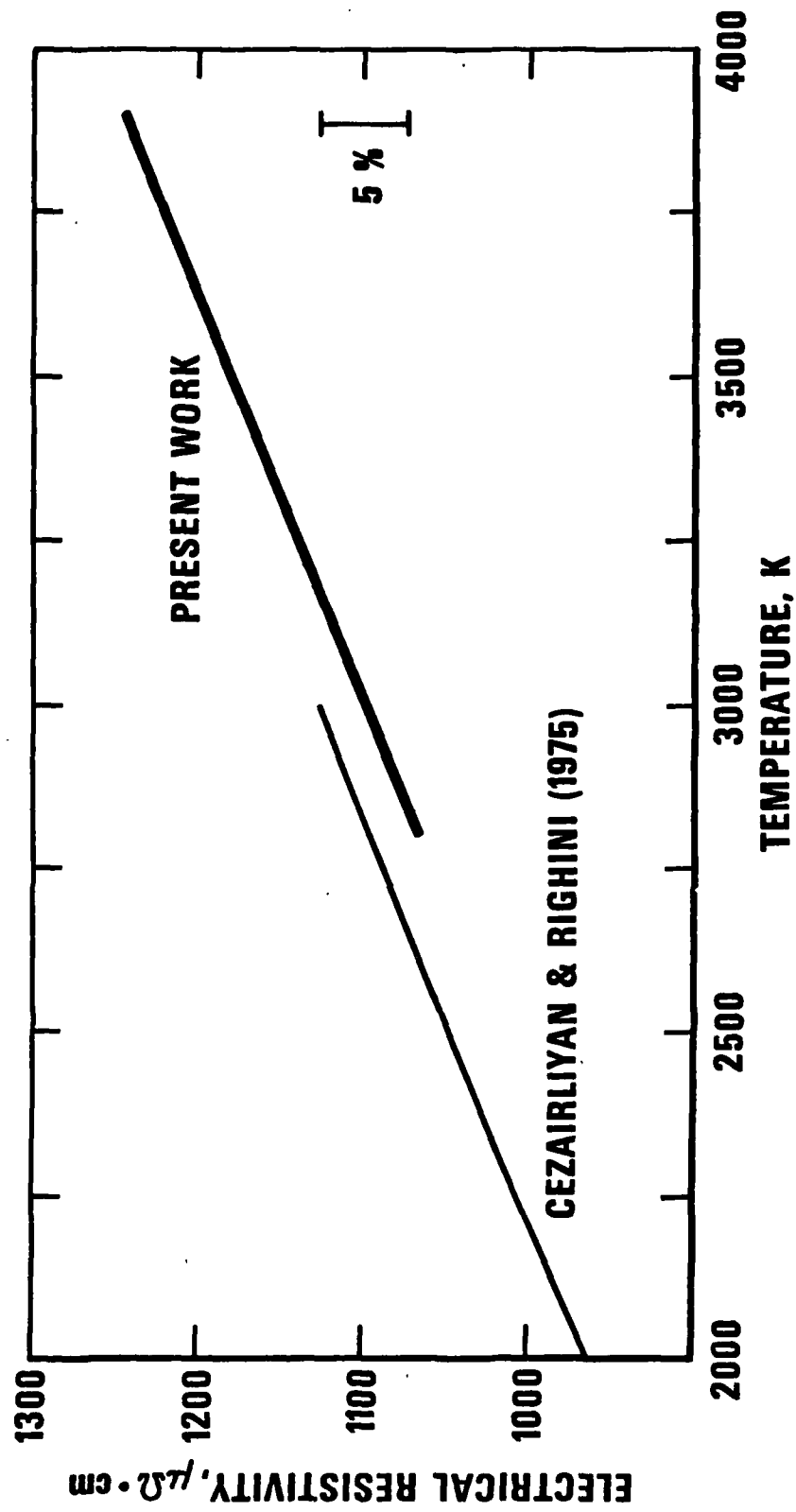


Figure 1.3. Electrical Resistivity of Graphite at High Temperatures Reported in the Literature.

With the present system and operating conditions it was not possible to extend the measurements to temperatures significantly above 3600 K. Above 3600 K, the smooth heating curve (temperature versus time), as obtained from the pyrometer output, showed discontinuities typical of interference of graphite vapor with radiation from the specimen. In order to extend the measurements to temperatures above 3600 K, work is planned to perform the measurements with the specimen under an inert gas environment at pressures higher than that used so far, at least up to 20 MPa.

References

1. Cezairliyan, A., and Righini, F., Rev. Int. Htes. Temp. et Réfract., 12, 124 (1975).
2. Cezairliyan, A., J. Res. Nat. Bur. Stand. (U.S.) 75C, 7 (1971).
3. Cezairliyan, A., Morse, M.S., Berman, H.A., and Beckett, C.W., J. Res. Nat. Bur. Stand. (U.S.) 74A, 65 (1970).
4. Rasor, N.S., and McClelland, J.D., J. Phys. Chem. Solids 15, 17 (1960).
5. Sheindlin, A.E., Belevich, I.S., and Kozhevnikov, I.G., High Temperature 10, 897 (1972).

2. Measurement of the Thermal Expansion of Tantalum in the Range 1500 to 3200 K by a Transient (Subsecond) Interferometric Technique

There has been an increasing need in recent years for thermal expansion data on refractory materials at temperatures above the limit of accurate steady-state experiments. Steady-state techniques such as push-rod dilatometry, x-ray diffractometry or twin-telemicroscope methods are generally limited due to problems associated with heat losses, chemical reactions, evaporation, etc., which become especially severe at temperatures above 2000 K. To overcome these difficulties, a unique transient interferometric technique has been developed recently [1,2] at the National Bureau of Standards for the purpose of measuring thermal expansion of solids at temperatures primarily in the range 1500 K and the melting point of the specimen.

The basic method involves rapidly heating the specimen from room temperature to the maximum temperature of interest in less than one second by the passage of an electrical current pulse through it, and simultaneously measuring the specimen temperature by means of a high-speed photoelectric pyrometer and the shift in the fringe pattern produced by a Michelson-type interferometer. The polarized beam from a He-Ne laser in the interferometer is split into two component beams, one which undergoes successive reflections from optical flats on opposite sides of the specimen, and one which serves as the reference beam.

In this report, we briefly summarize the results of measurements performed during FY81 on the thermal expansion of tantalum at temperatures between 1500 and 3200 K. The purpose of these experiments was twofold: (1) to assess the operational characteristics of the interferometric system over a large temperature range, particularly at temperatures approaching the melting point, and (2) to obtain accurate expansion values for tantalum at temperatures where considerable disagreement exists among data reported in the literature.

The experiments were performed on four specimens, each fabricated in the form of a precision-machined tube (with optical flats) containing a small sighting hole for direct pyrometric measurement of blackbody temperature. In a typical experiment, the specimen was resistively

pulse-heated in a vacuum environment (~ 1 mPa) from room temperature to the desired temperature in about 800 ms. The analog signals from the pyrometer and the interferometer were recorded during the experiment by means of digital storage oscilloscopes. The recorded data was then transferred to a minicomputer for subsequent computation of specimen temperatures and fringe shifts.

The linear expansion of a specimen was determined at each recorded temperature from the cumulative fringe shift which, for the range 1500 to 3200 K, varied from about 165 to 480 fringes. The expansion/temperature data pairs for the four specimens were combined and then fitted by a polynomial function of temperature by means of the least-squares method. The function that represents the results for linear thermal expansion of tantalum (standard deviation = 0.2%) in the temperature range 1500 to 3200 K is

$$\Delta l/l_0 = 5.141 \times 10^{-4} + 1.445 \times 10^{-6} T + 4.160 \times 10^{-9} T^2 - 1.309 \times 10^{-12} T^3 + 1.901 \times 10^{-16} T^4 \quad (1)$$

where T is in K and l_0 is the specimen length at 20°C (nominally 6.1 mm for all specimens). The smoothed results, as defined by Eq. (1), are given (in percent) at intervals of 100 K in Table 1.

The results for each specimen were also fitted by a quartic polynomial in temperature by means of the least-squares method. As shown in Fig. 2.1, the deviation of the smoothed results for the individual specimens from those represented by Eq. (1) varies from about 0.2% at 2000 K to about 0.4% at 3000 K.

The major source of error in our results arises in the determination of specimen temperature. It is estimated that the error in temperature is about 5 K at 2000 K and about 10 K at 3000 K which correspond to uncertainties in $\Delta l/l_0$ of about 0.3% and 0.5% at the respective temperatures. The maximum uncertainty in the fringe count is believed to vary from about 0.5 fringe at 2000 K to about 1 fringe at 3000 K which correspond to an uncertainty in $\Delta l/l_0$ of approximately 0.2% over the entire temperature range. A further uncertainty of about 0.2% arises in determining the specimen length at "room" temperature (20°C). Therefore, the maximum error in our reported values of linear expansion is estimated to be about 1% at 2000 K and not more than 2% at 3000 K.

Table 1. Smoothed results for linear thermal expansion of tantalum.

Temperature, K	$\Delta l/l_0$, %	Temperature, K	$\Delta l/l_0$, %
1500	0.859	2400	1.616
1600	0.936	2500	1.710
1700	1.015	2600	1.807
1800	1.096	2700	1.908
1900	1.178	2800	2.012
2000	1.261	2900	2.121
2100	1.347	3000	2.234
2200	1.434	3100	2.353
2300	1.524	3200	2.478

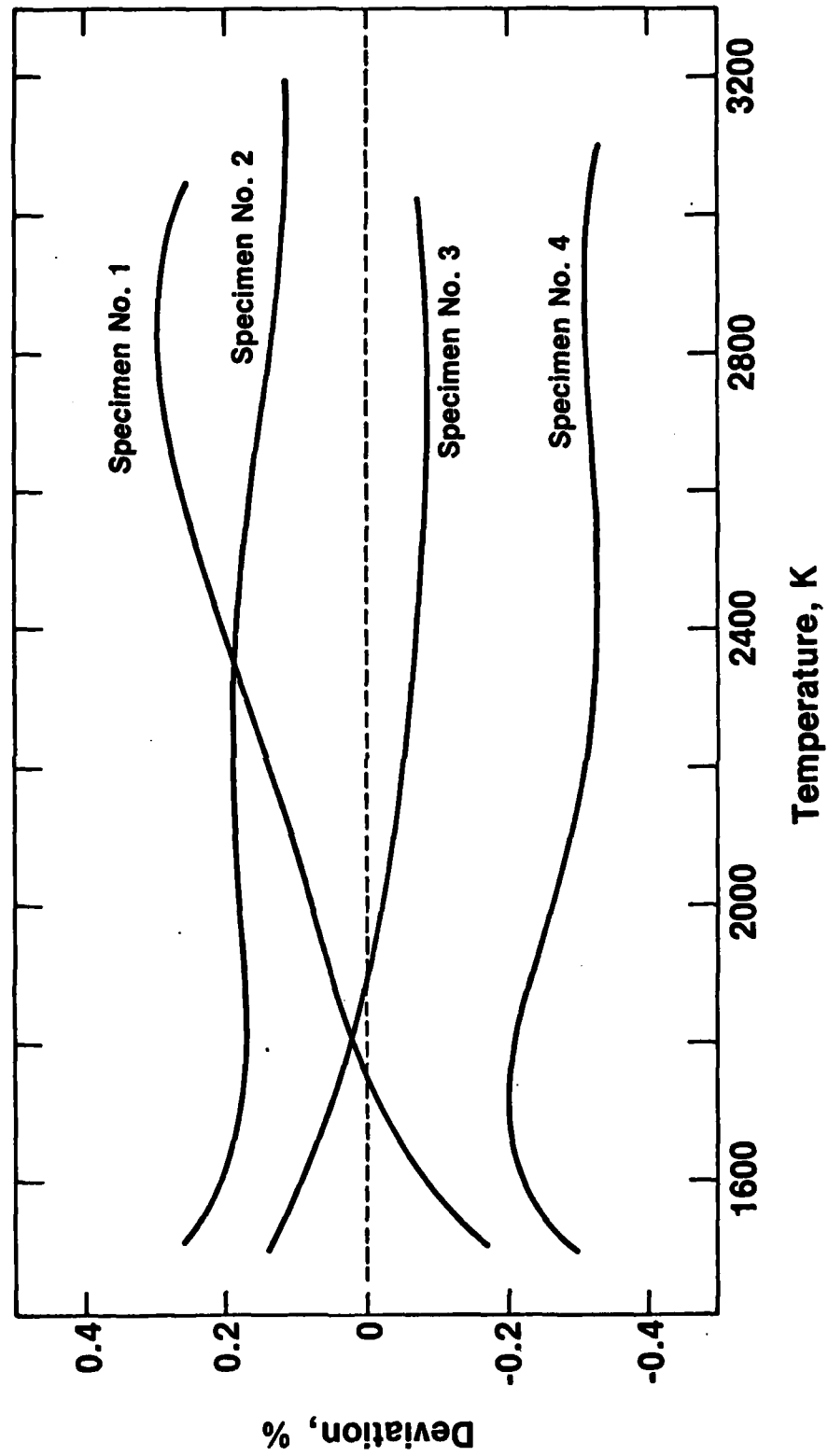


Figure 2.1. Deviation of the smooth results for the individual specimens from the least-squares fit [represented by Eq. (1)] to the combined data for the four specimens.

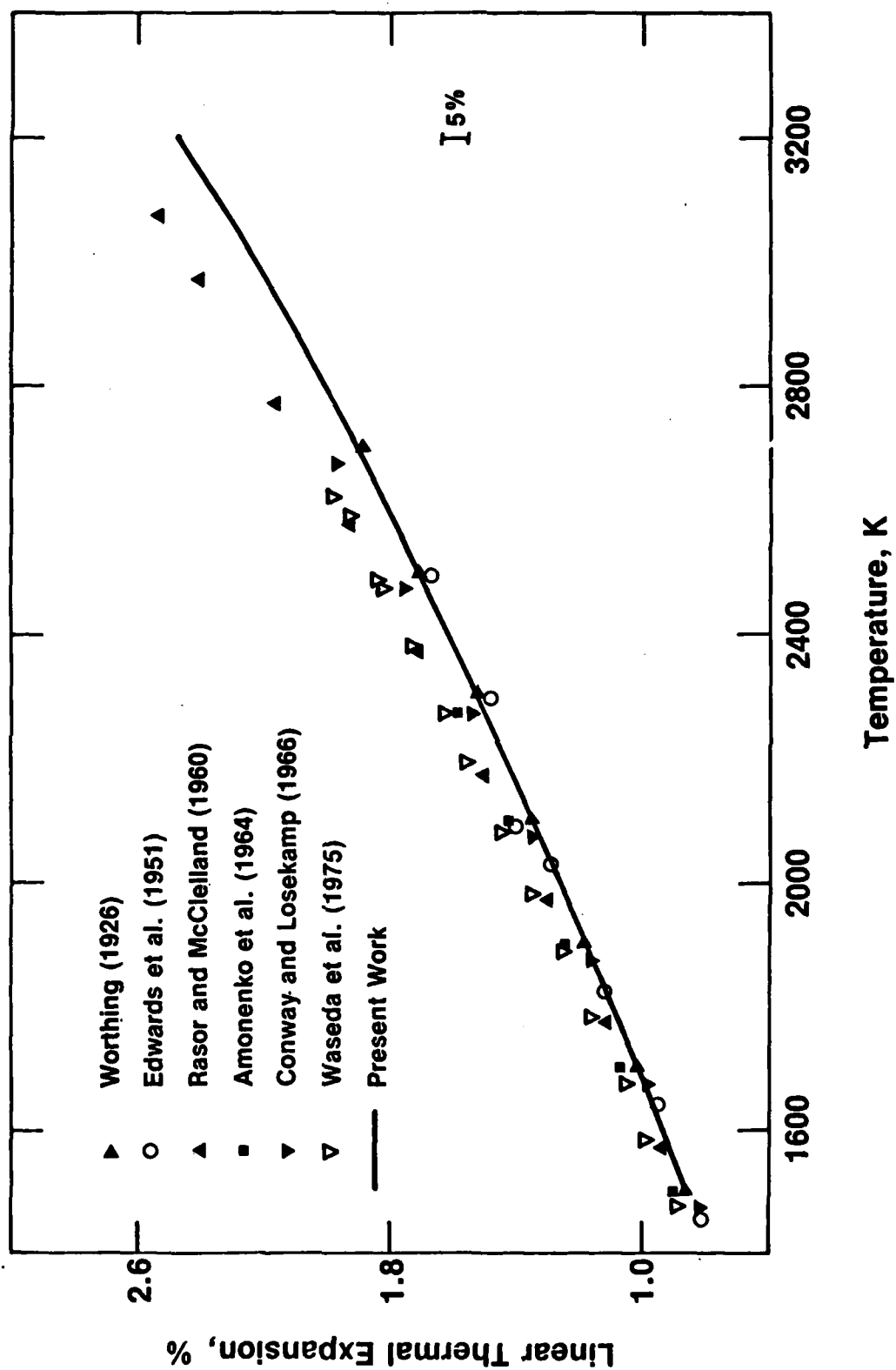


Figure 2.2. Linear thermal expansion of tantalum: present work and data reported in the literature.

The results of the present work are compared in Fig. 2.2 with expansion values reported in the literature. Worthing [3], Rasor and McClelland [4] and Conway et al. [5] obtained their expansion data using the twin-telemicroscope method. The values of expansion reported by Edwards et al. [6] and Waseda et al. [7] were measured by x-ray diffraction techniques. Amonenko et al. [8] obtained their data by conventional dilatometry. The data disagree by as much as 10% throughout the entire temperature range but do not show any significant bias towards a given steady-state measurement technique. The data reported by Worthing and by Edwards et al. are in rather good agreement with the results of the present work. The expansion values determined by Conway and Losekamp agree with those of the present work within the combined experimental errors of the two investigations. However the expansion results reported by the remaining investigators are considerably higher than our results.

In summary the results of the present study show that our transient interferometric technique is capable of measuring thermal expansion of metals at temperatures between 1500 K and their melting points with an estimated error of less than 2%.

References

1. Miller, A.P., and Cezairliyan, A., in "Thermal Expansion 6," I.D. Peggs, ed. (Plenum Press, New York, 1978) p. 131-143.
2. Miller, A.P., and Cezairliyan, A., in "Thermal Expansion of Solids," to be published by CINDAS of Purdue University.
3. Worthing, A.G., Phys. Rev. 28, 190-201 (1926).
4. Rasor, N.S., and McClelland, J.D., J. Phys. Chem. Solids 15, 17-26 (1960).
5. Conway, J.B., and Losekamp, A.C., Trans. Met. Soc. AIME 236, 702-709 (1966).
6. Edwards, J.W., Speiser, R., Johnston, H.L., J. Appl. Phys. 22, 424-428 (1951).
7. Waseda, Y., Hirata, K., and Ohtani, M., High Temp.- High Pressures 7, 221-226 (1975).
8. Amonenko, V.M., Vyugov, P.N., and Gumenyuk, V.S., High Temp. (USSR) 2, 22-24 (1964).

3. Measurement of the Radiance Temperature (at 653 nm) of Tungsten at its Melting Point

With the increased interest in high temperature applications, accurate temperature measurements in high temperature systems has become important. A major problem is the difficulty associated with reference points in temperature calibrations. The best conventional reference points are blackbody furnaces operating at the melting point of selected metals. Because of the serious problems associated with systems exposed to high temperatures for prolonged periods of time, the practical limit for blackbody furnaces is 2000 K. During recent years, we have been investigating the possibility of establishing secondary reference points at high temperatures based on the surface radiance temperature of metals during melting. Our earlier work on radiance temperature measurements at the melting point of selected refractory metals, such as niobium [1], molybdenum [2], tantalum [3], indicates reliability and reproducibility of such measurements.

The present work involved the measurement of radiance temperature (at 653 nm) of tungsten at its melting point. Since tungsten has the highest melting point among the elements, the results are of particular interest to the high temperature field.

The measurements were performed on 23 tungsten specimens of 99.9+ purity. Before the experiments, the surfaces of a number of specimens were treated with an abrasive. Two different grades of abrasive were used yielding two surface roughnesses (approximately 0.2 and 0.4 μm in roughness).

All the experiments were performed with the specimen in an argon environment at atmospheric pressure. The heating rates for different specimens were in the range 1100 - 5400 $\text{K}\cdot\text{s}^{-1}$. Variation of the radiance temperature as a function of time for two typical experiments is shown in Fig. 3.1.

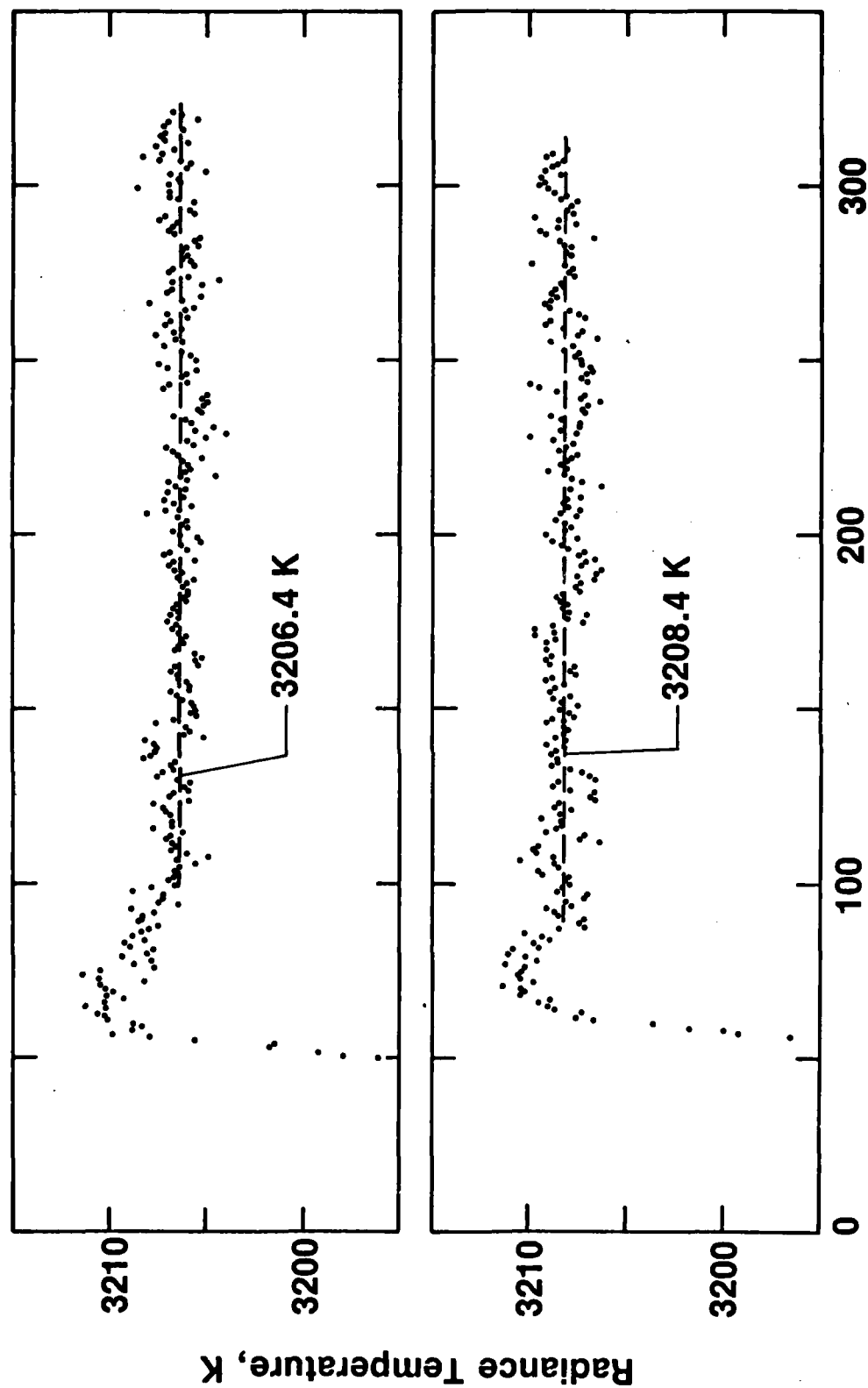
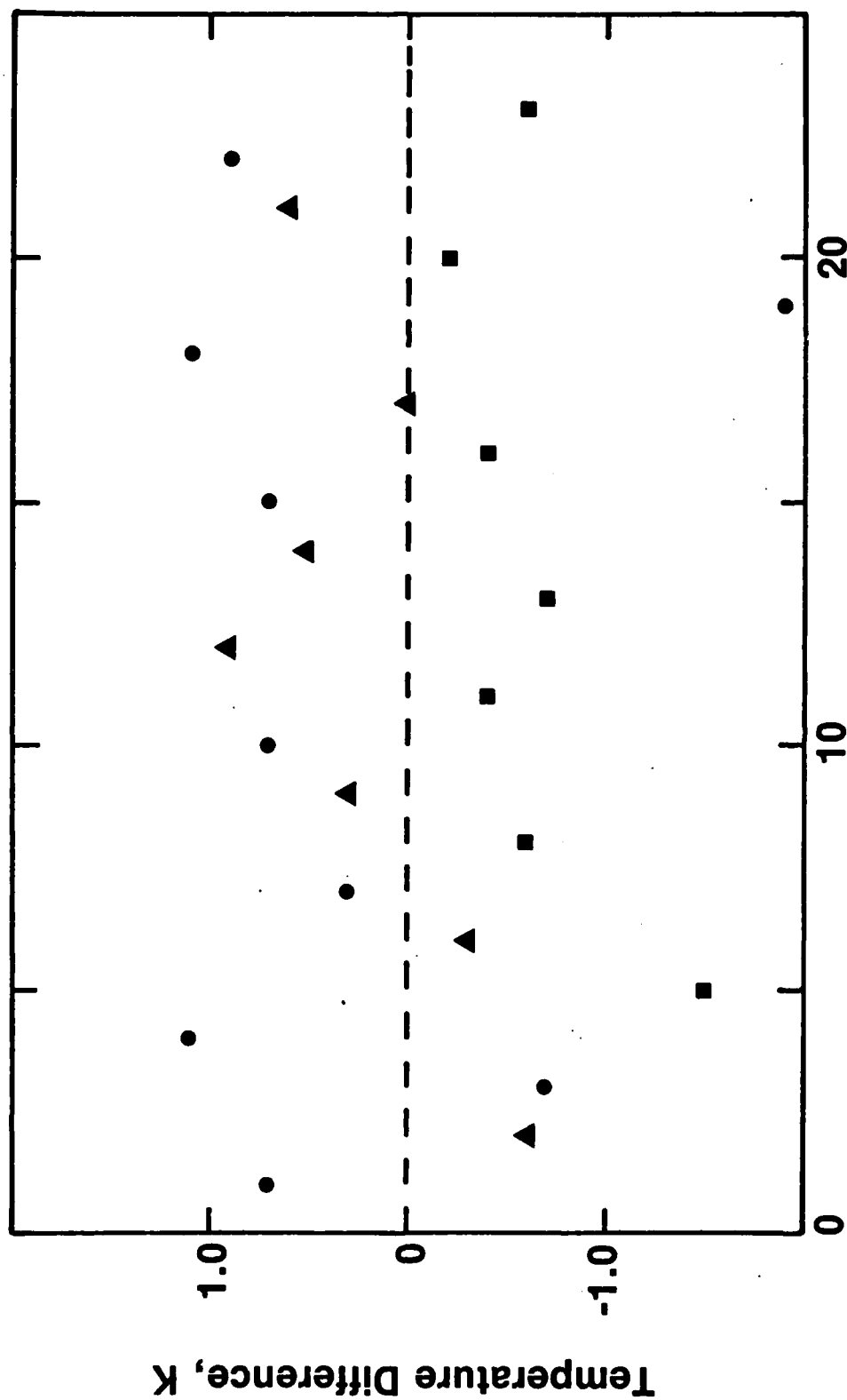


Figure 3.1. Variation of radiance temperature (at 653 nm) of tungsten as a function of time near and at its melting point during typical experiments on two specimens each treated with a different abrasive, yielding surface roughnesses of approximately 0.2 μm (upper) and 0.4 μm (lower).



Experiments in Chronological Order

Figure 3.2. Difference of the average radiance temperature at the melting plateau for each specimen from the average value 3207.9 K for all the specimens. The symbols ●, ■, ▲ refer to experiments in which the surface roughnesses were about 0.1 ("as received" condition), 0.2 and 0.4 μm , respectively.

It may be seen that, regardless of the differences in the initial surface conditions, radiance temperature at the melting plateau is approximately the same for the two specimens. The same conclusion is reached for all other specimens. For each specimen, the plateau temperatures were averaged to yield a single temperature for that specimen. The standard deviation of these averages ranged from 0.7 to 0.9 K. Fig. 3.2 shows the departure of the average radiance temperature for each specimen from the average for all the specimens. The overall average for 23 specimens yielded a value of 3208 K for the radiance temperature (at 653 nm) of tungsten at its melting point with a standard deviation of 0.8 K. There is no evidence of any significant bias with respect to initial surface roughness of the specimen or the heating rate of the specimen. The total error in the measured radiance temperature is estimated to be not more than 10 K.

The results on tungsten have confirmed the earlier results on other refractory metals that radiance temperature at the melting point of metals is reproducible and constant for a metal and is virtually independent of the initial surface conditions of the specimen and the operational conditions (heating rate, etc.) of the overall system. In conclusion, the results suggest the possibility of using the radiance temperature at the melting point of selected metals for secondary calibration and checking of optical temperature measuring equipment in high temperature systems.

References

1. Cezairliyan, A., J. Res. Nat. Bur. Stand. (U.S.), 77A, 333 (1973).
2. Cezairliyan, A., Coslovi, L., Righini, F., and Rosso, A., in Temperature Measurement 1975, B. F. Billing and T. J. Quinn, eds., Conference Series No. 26, Institute of Physics, London, 1975, p. 287.
3. Cezairliyan, A., McClure, J.L., Coslovi, L., Righini, F., and Rosso, A., High Temperatures-High Pressures 8, 103 (1976).

Enthalpy of POCO Graphite AXM-5Q1 From

273 K to 1173 K

by

David A. Ditmars

1. Introduction

Graphite is an important material in high-temperature technology, finding applications as both a standard reference material for high-temperature thermophysical properties and as a component in carbon-carbon composites for high-temperature structural components. For this reason, accurate determination of the thermophysical properties of graphite has been the subject of several investigations in recent years [1-7]. The most important thermophysical properties for the purpose of heat-transfer calculations are thermal diffusivity, thermal conductivity, and heat capacity. These are related to each other in the relation,

$$\kappa = \frac{k}{\rho C_p},$$

where κ is thermal diffusivity; k , thermal conductivity; ρ , density; and C_p , specific heat. Since each of the three thermophysical properties contained in this relation can be measured independently, the possibility exists for comparing directly-measured values for any one of these properties with corresponding values calculated, using the above relation, from direct measurements of the other two properties.

Graphite is obtainable in both natural and synthetic forms. The synthetic form is available in many different "grades". These grade designations are designations assigned by the manufacturer which specify in coded form such information on the graphite as grain size, temperature of graphitization, chemical purity, or other proprietary data.

The specific heat data for all graphite grades has shown a rather large variance, most data lying in a range $\pm 10\%$ between room temperature and 2500 K [7]. It has not been made clear whether this large variance is directly related to systematic measurement error or whether it indicates a real dependence of thermophysical properties on the method of synthesis. For this reason, it has seemed desirable to have a set of data for at least one of the thermophysical properties cited above, extending over a wide temperature range.

A very pure grade of graphite ("POCO" graphite) produced by the POCO graphite company of Decatur, Texas, and designated as grade AXM-5Q1 has been chosen by NBS as a high-temperature thermal-conductivity standard reference material. Direct measurement of the heat capacity of this material by a pulse-calorimetric technique in the temperature range 1500 to 3000 K [3,4] has been carried out earlier in the NBS Thermophysics Division. Specific-heat data on this same material obtained by other investigators have also been reported in the recent literature [5] in the temperature range 300 to 1000 K. These data were obtained by scanning calorimetry.

We have undertaken the measurement of the specific heat of graphite, grade AXM-5Q1 in the temperature range 273 to 1500 K by relative-enthalpy calorimetry using a precision Bunsen ice calorimeter and a precision adiabatic-receiving calorimeter. The aim is to provide more accurate specific-heat data below 1000 K and to bridge the present gap in the specific-heat data for this material between 1000 and 1500 K. This report gives the preliminary results on enthalpy data obtained in the temperature range 273 to 1173 K.

2. Samples

Two samples of graphite were chosen for enthalpy measurement. These graphites are designated as samples "1" and "2". Sample 1 comprised two specimens of AXM-5Q1 graphite, obtained from the lot of material reserved for the NBS thermal-conductivity SRM. Sample 2 consisted of a single specimen of AXM-5Q graphite (in principle, a grade of slightly lower purity) chosen from the same lot which was the source of the graphite specimens which were measured in the prior AGARD project of cooperative measurements on heat-transport phenomena of solids at high temperatures [1]. It had been previously noted [8] that there was a small ($< 4\%$) density variance throughout the stock of NBS graphite (sample 1). Therefore, the two specimens of sample 1 for enthalpy measurement were chosen from rods "62-end 2" and "104-end 2", which showed a representative density difference. These specimens are hereafter designated "1H-62" and "1H-104". The specimen of the sample 2 for enthalpy measurement is designated "2H". These three specimens were machined as right circular cylinders for encapsulation and enthalpy measurement. The measured specimen masses and calculated densities are given in Table 1.

Table 1
Enthalpy-measurement specimens of POCO graphite

Specimen	Grade	Calculated	Specimen
		Apparent density g cm^{-3}	Mass g
(1H-62)	AXM-5Q1	1.738	6.98047
(1H-104)	AXM-5Q1	1.706	6.82563
(2H)	AXM-5Q	1.756	7.05369

Chemical analyses on the present POCO graphite were performed by two independent analytical laboratories on specimens chosen from sample 1; one of these laboratories also included a specimen of sample 2 in their analyses.

Specimens of both samples were subjected to combustion analyses by the Galbraith Laboratories of Knoxville, Tennessee. These analysis specimens were cut from portions of the appropriate sample materials which were adjacent to the enthalpy-measuring specimens. The results of these analyses are given in Table 2. Here, the specimen nomenclature differs from that of Table 1 only in that "A" is substituted for "H".

Table 2

Combustion Analyses of POCO Graphite

Specimen	Calculated	Composition - wt %			
	Apparent Density	C	H	N	ash
	g cm^{-3}				
(1A-62)	1.731	99.66	< 0.05	0.027	0.29
(1A-104)	1.728	97.77	< 0.05	0.017	1.94
(2A)	---	99.49	< 0.05	0.012	0.48

Specimens of Sample 1 were examined in the analytical laboratories of the Union Oil Company of California^a. These specimens were chosen from different rods of Sample 1 designated rods "13-end 2" and "46-end 2". The corresponding analysis specimens are designated (1A-13) and (1A-46): Table 3 and Figures 1 and 2 present the results of porosimetric, qualitative spectrometric and absorbed gas analyses on these specimens. Mercury porosimetry analysis

^a We are indebted to Dr. M.J. Block of the Union Oil Company for his generosity and cooperation in making the facilities for these analyses available.

(Figures 1 and 2) of these specimens determined the total open porosity (OP') to be 0.08114 and 0.08053 cc/g for (1A-13) and (1A-46), respectively. These are converted to percent total volume units by the following equation

$$OP = (OP') (\rho) (100),$$

where OP is the percent open porosity and ρ is the calculated density of the graphite. The theoretical porosity is determined by the equation

$$TP = \left[\frac{1}{\rho} - \frac{1}{2.26} \right] (\rho) (100),$$

and is a measure of the porosity expected when the theoretical density of graphite (2.26 g/cc) and the observed density of the graphite artifact are taken into account. The open porosity is always less than the theoretical porosity due to the fact that some fraction of the porosity is blind and does not communicate with the outside of the piece. The difference between the theoretical porosity and open porosity is the closed porosity. Pore diameter and surface area data are also derived from porosimetry testing and are also listed in Table 3.

Elemental analyses performed on the graphite specimens were limited to hydrogen analysis and qualitative emission spectroscopy (ES) analysis of the graphite ash. These results are also presented in Table 3. An attempt was made to analyze the gas adsorbed on the graphite. A sample of graphite was ground to a fine powder and then sealed in an evacuated glass bomb. The sample was heated to about 200 °C and the off-gas was analyzed via mass spectroscopy. The major components of the off-gas were carbon dioxide, carbon monoxide, and water. Table 3 supplies further details concerning the off-gas composition.

Table 3
Porosimetric, Qualitative Spectrometric and
Adsorbed Gas Analyses of POCO Graphite

Specimen	(1A-13)	(1A-46)
Density, g/cc (calculated)	1.766	1.705
Porosimetry Data		
Pore Volume, % volume		
Theoretical	21.86	24.56
Open	14.33	13.73
Closed	7.53	10.83
Average Pore diameter, μ	1.21	1.12
Surface Area, m^2/g	0.52	0.64
Elemental Analyses		
Hydrogen, Wt %	0.005	0.022
Ash, Qualitative E.S.		
10%	Si	Si
1-10%	--	--
0.1-1%	Fe, Ca, V, Al, Pb	Fe, Al, Cu, Pb
0.1%	Mg, Sr, Cu, Cr	Mg, Cr, Cu, Ni, Mn, Sr

Adsorbed Gas Analysis

<u>Species</u>	<u>Mole %</u>	<u>Species</u>	<u>Mole %</u>
CO ₂	42.5	H ₂	0.10
H ₂ O	39.6	C ₂ H ₂	0.06
CO ^a	13.3	I-C ₅	0.06
Air	2.94	H ₂ S	0.03
CH ₄	0.48	I-C ₄	0.03
C ₃ H ₈	0.43	C ₂ H ₆	0.02
SO ₂	0.22	C ₄ H ₈	0.01
C ₂ H ₄	0.13	COS	0.01
C ₃ H ₄	0.11		

a. A maximum of 3% could be N₂.

3. Experimental Procedure

The three graphite specimens were sealed with no prior treatment in Pt-10Rh capsules containing helium gas at a pressure of approximately 0.2 atm. Relative enthalpy measurements ($H_T - H_{273.15}$) were made on each of the three encapsulated specimens in the temperature range 273-1173 K with a Bunsen ice calorimeter. The measuring apparatus and techniques have been described earlier [9-11]. Enthalpy data were obtained at nine temperatures starting at 373 K and continuing at nominal 100 K intervals. Specimen (1H-62) was measured two or three times at each temperature to enable estimation of the precision of the data series; the other specimens, not at each temperature and not as frequently. Empty capsule data obtained previously [10] for identical Pt-10Rh capsules were used in calculating the net contributions of the graphite to the gross observed heats.

In addition to the graphite enthalpy measurements, measurements were made on $\alpha\text{-Al}_2\text{O}_3$ (NBS Standard Reference Material 720) at selected temperatures to verify the overall accuracy of the measuring technique.

4. Results

The enthalpy data on the three graphite specimens is given in Table 4 and Figure 3. The relative enthalpy data of Table 4 were calculated by subtracting from the gross measured heat the capsule enthalpy, taken from [10], at the corresponding temperature and dividing by the appropriate sample mass to express the results on a unit mass basis. For the purpose of these calculations, the specimens were assumed to be 100 percent graphite. The contribution of the specimen capsule to the gross measured heats did not exceed 25 percent. Enthalpy measurements on $\alpha\text{-Al}_2\text{O}_3$ made at 373 K, 273 K, and 1173 K agreed with earlier enthalpy data on this Standard Reference Material to better than 0.15 percent.

The smoothed form for these enthalpy data will be influenced also by existing heat-capacity data on graphite from low-temperature adiabatic calorimetry and on future measurements in this laboratory on these specimens in the 1173 K to 1500 K region. In Figure 3, however, we have compared the present data with enthalpies derived from the smooth heat-capacity data presented in [7] for AXM-5Q1 graphite. Above 373 K, there is no significant difference in the enthalpy data for the three specimens. The deviations of the data for specimens (1H-104) and (2H) at 373 K, while coming in a temperature range in which the calorimeter imprecision has been historically high, are somewhat larger than anticipated. It is not yet clear whether the difference arises from random error or is due to water or other substances adsorbed on the specimens.

5. Bibliography

1. Fitzer, E., Thermophysical Properties of Solid Materials - AGARD Report No. 606, 115pp, 1973, AD-760165, (Available from NTIS).
2. West, E.D. and Ishihara, S., in Advances in Thermophysical Properties at Extreme Temperatures and Pressures, 146-151, ASME, New York (1965).
3. Cezairliyan, A. and Righini, F., Rev. int. Hts Temp. et Refract. 12, 124 (1975).
4. Cezairliyan, A., in Proc. 6th Symp. Thermophys. Prop., 279-285, ASME, New York (1973).
5. Taylor, R. E. and Groot, H., Report PRL 153 (AFOSR 77-3280) 32 pp, Purdue University, Indiana (1978).
6. Taylor, R.E. and Groot, H., High Temp. High Press 12, 147 (1980).
7. Deshpande, M.S. and Bogaard, R.H., in Proc. 17th Int. Therm. Condcy. Conf. (1981). (To be published.)
8. Hust, J., [Private communication.] (1981).
9. Ditmars, D. A., Cezairliyan, A., Ishihara, S., and Douglas, T.B., NBS Special Publication 260-55, 80pp. (1977), For sale by the Superintendent of Documents, U.S. Govt. Printing Office, Washington, D.C. 20402.
10. Ditmars, D.A. and Douglas, T.B., J. Res. Nat. Bur. Stand. (U.S.), 75A (Phys. and Chem.) No. 5, 401 (1971).
11. Douglas, T.B. and King, E.G., "High-Temperature Drop Calorimetry", Chap. 8 in Experimental Thermodynamics, Vol I, Calorimetry of non-Reacting Systems, p. 293, McCullough, J.P. and Scott, D.W., eds., (Butterworths, London, 1968).

The Thermodynamic Properties of Diatomic Molecules at Elevated
Temperatures: Role of Continuum and Metastable States

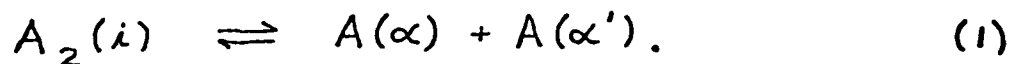
Frederick H. Mies and Paul S. Julienne

ABSTRACT

A complete quantum formulation of diatomic partition functions uses the energy-variation of the elastic scattering phase-shift to represent the phase space associated with the molecular continuum states. The resonance structure in the phase-shift, due to tunnelling through rotational barriers, gives a rigorous interpretation of the metastable states which lie behind the barrier, and we can justify the need to include such states in the evaluation of thermodynamic properties. However, we also find that it is inconsistent to merely include the metastable phase-space without considering the remaining contributions from the continuum. If either component is ignored in treating the dimer, then, of necessity, their presence will appear as the virial coefficients which cause non-ideal behavior for the atomic fragments of the molecule. Both approaches are consistent and yield a proper equation of state for the vapor. We will show quantitative agreement between the exact quantal results and the approximate classical expressions for the partition function at high temperatures. Since the classical theory automatically includes all the effects of the molecular continuum, we suggest that this is both the simplest and most unambiguous procedure for extending thermodynamic tables to elevated temperatures. Explicit calculations are presented for Li_2 and Na_2 .

I. INTRODUCTION

At elevated temperatures the equation of state and other observable equilibrium properties associated with the diatomic molecule A_2 must account for the dissociation processes,



The ensemble is divided into sub-sets of molecules $A_2(i)$ in specific ω_i -degenerate electronic states $|i\rangle$. Each state is characterized by an interatomic potential $V_i(R)$ which adiabatically correlates with a unique pair of atomic states,¹

$$V_i(R) \underset{R \rightarrow \infty}{\sim} E_\alpha(i) + E_{\alpha'}(i). \quad (2)$$

The internal partition function Q_i associated with each attractive state contains both bound $Q_i(B)$ and continuum or dissociative $Q_i(C)$ state contributions.^{2,3,4,5}

$$Q_i = Q_i(B) + Q_i(C). \quad (3)$$

At low temperatures Q_i is dominated by the finite set of stable, bound rotational (ℓ) - vibrational (v) eigenstates with discrete energies $\epsilon_{i,\ell,v} < 0$ which define $Q_i(B)$,

$$Q_i(B) = \sum_{\ell} (2\ell+1) \sum_v e^{-\epsilon_{i,\ell,v}/kT}. \quad (4)$$

It is this contribution which normally defines the molar thermodynamic parameters we associate with the stable molecule A_2 . However, at high temperatures, or for predominately repulsive potentials, we must expect

significant, if not dominant, contributions from the continuum of states with $\epsilon > 0$ which lie above the dissociative limit.

We shall examine the exact quantum mechanical expression for $Q_i(C)$,^{5,6,7}

$$Q_i(C) = \sum_l (2l+1) \int_0^\infty d\epsilon e^{-\epsilon/kT} \frac{\partial \eta_{i,l}(\epsilon)}{\pi \partial \epsilon}. \quad (5)$$

The density of molecular continuum states is related to the phase-shift⁸ $\eta_{i,l}(\epsilon)$ for the scattering of atoms $A(\alpha) + A(\alpha')$ by the electronic-rotational potential,⁹

$$V_{i,l}(R) = V_i(R) + \frac{l(l+1) \hbar^2}{m_A R^2}, \quad (6)$$

where the relative kinetic energy ϵ is measured with respect to the $R = \infty$ asymptote for $v_i(R)$,

$$V_{i,l}(R) = V_i(R) - E_{\alpha}(i) - E_{\alpha'}(i) \underset{R \rightarrow \infty}{\sim} 0. \quad (7)$$

In particular we are concerned with the role of metastable rotational-vibrational levels, $\epsilon_{i,l,m} > 0$, which are predicted to exist behind the rotational barriers^{3,4,5} in Eq. (6), and we shall segregate $Q_i(C)$ into two components,

$$Q_i(C) = Q_i(M) + Q_i(F), \quad (8)$$

where,

$$Q_i(M) = \sum_l (2l+1) \sum_m e^{-\epsilon_{i,l,m}/kT}. \quad (9)$$

This finite set of predissociating levels is often combined with $Q_i(B)$ to define the thermodynamic properties^{10,11} of the dimer A_2 , and

there has been some confusion as to whether this procedure is legitimate. We shall show that this approach can be justified on rigorous quantum mechanical grounds in terms of the resultant resonance structure^{5,8,12,13} contained in the phase-shift $\eta_{i,l}(\epsilon)$. However, we also contend that the residual contributions contained in what has been termed the free-continuum^{3,5} component $Q_i(F)$ cannot be neglected.

Although $Q_i(B)$ and $Q_i(M)$ are always positive, $Q_i(F)$ can be of either sign depending on v_i and T , and it is inconsistent to neglect the free continuum when defining the properties of A_2 . We will propose that the most accurate, and by far the simplest course is to use the complete classical theory for Q_i at high temperatures. The partition function is directly related to the second virial coefficient B_i for potential v_i ,

$$Q_i = -q_{tr}(m_A/2) B_i, \quad (10)$$

where $q_{tr}(m)$ is an abbreviated notation for the translational partition function per unit volume for particles of mass m ,

$$q_{tr}(m) \equiv \left(\frac{2\pi m kT}{h^2} \right)^{3/2}. \quad (11)$$

The simple classical expression for B_i ,^{2,3,5,6,7}

$$B_i = 2\pi \int_0^\infty \left(e^{-U_i(R)/kT} - 1 \right) R^2 dR, \quad (12)$$

contains all three contributions to Q_i , i.e.,

$$B_i = B_i(B) + B_i(M) + B_i(F), \quad (13)$$

and therefore there is no bias introduced into the evaluation of the thermodynamic variables. We have already shown⁵ that the classical

theory yields quantitative agreement with the quantal theory once kT exceeds the vibrational spacings.

Equation (1) implies that a total number of atoms N confined in some volume V at temperature T will partition into two portions N_A and N_{AA} which must satisfy the conservation of mass

$$N = N_A + 2 N_{AA} . \quad (14)$$

These entities which we refer to as 'monomers' and 'dimers' are defined by the particular regions of phase space, or partition functions $(p.f.)_A$ and $(p.f.)_{AA}$, that we choose to assign to the particles. Implicit in all thermodynamic tabulations^{10,11,14} is the assumption that the center-of-mass motion of the atoms A and the molecules A_2 behave as ideal gases, such that the equation of state is

$$\begin{aligned} P/kT &= N_A/V + N_{AA}/V \\ &= N/V - N_{AA}/V. \end{aligned} \quad (15)$$

Given the equilibrium constant K_{eq} ,

$$\frac{N_{AA}}{N_A^2} = \frac{(p.f.)_{AA}}{(p.f.)_A^2} = \frac{K_{eq}}{V}, \quad (16)$$

we can express (15) as an infinite power series in (N/V) ,

$$\frac{P}{kT} = \frac{N}{V} - K_{eq} \left(\frac{N}{V}\right)^2 + 4 K_{eq}^2 \left(\frac{N}{V}\right)^3 + \dots \quad (17)$$

which is comparable to the usual virial expansion^{2,3,5,6,7}

$$\frac{P}{kT} = \frac{N}{V} + \langle B \rangle \left(\frac{N}{V}\right)^2 + \langle C \rangle \left(\frac{N}{V}\right)^3 + \dots \quad (18)$$

with the result that

$$\langle B \rangle \equiv -K_{eq} \quad (19)$$

Note however that the molecular dimer contributes to all virial coefficients and $\langle C \rangle$ is negligible only if $(K_{eq} N/V) \ll 1$. In fact Eq. (17) is not convergent unless $(K_{eq} N/V) \leq 1/8$, and for strongly bound molecules it is preferable to employ Eq. (15) which describes both low and high temperature limits exactly.

The decomposition of the internal partition function Q_i into bound (B), metastable (M), and free-continuum (F) components in Eqs. (3) and (8) leads to a similar separation of the equilibrium constant

$$K_{eq} = K_{eq}(B) + K_{eq}(M) + K_{eq}(F) \quad (20)$$

and the dimer concentration

$$N_{AA} = N_{AA}(B) + N_{AA}(M) + N_{AA}(F) \quad (21)$$

in Eq. (16). Thus we can cast the equation-of-state into several equivalent forms

$$\frac{P}{RT} = \frac{N_A}{V} + \frac{[N_{AA}(B) + N_{AA}(M) + N_{AA}(F)]}{V} \quad (22a)$$

$$= \frac{N_A}{V} \left(1 + \frac{N_A K_{eq}(F)}{V} \right) + \frac{[N_{AA}(M) + N_{AA}(F)]}{V} \quad (22b)$$

$$= \frac{N_A}{V} \left(1 + \frac{N_A}{V} K_{eq}(C) \right) + \frac{N_{AA}(B)}{V}, \quad (22c)$$

all subject to the constraint imposed by Eq. (14). Obviously by modifying the activity of the monomer concentration,⁵ from ideal in Eq.

(22a) to an imperfect gas with a second virial equal to $-K_{eq}(F)$ in Eq. (22b) and $-K_{eq}(C)$ in Eq. (22c), we can obtain different interpretations of the residual molecular dimer concentrations. This points to the basic problem inherent in the use of tabulated thermodynamic data to calculate equilibrium properties at high temperatures. Unless $K_{eq}(F)$ and $K_{eq}(M)$ are negligible we must be cognizant of the specific regions of phase space that have been included in the definition of the species A_2 . This supports the virtue of using the unambiguous expression in Eq. (12) to calculate K_{eq} .

The quantum theory of diatomic thermochemistry is discussed in section II with specific application to the alkali dimers¹⁵ shown in Fig. 1. Scattering theory is used to analyze the metastable and continuum contributions to the partition functions in section III. Explicit calculations of equilibrium constants for Li_2 and Na_2 are presented and discussed in section IV. A brief summary and recommendations for calculating high temperature thermodynamic variables are contained in Section V.

II. QUANTUM THEORY OF DIATOMIC THERMOCHEMISTRY

The 'free' atoms A and the diatomic molecule A_2 in Eq. (1) are uniquely defined by their partition functions. However we must fulfill two constraints if we hope to convert the resultant functions into observable physical properties of the equilibrated gas, such as the equation of state⁶

$$\frac{P}{kT} = N_A \frac{\partial \ln(p.f.)_A}{\partial V} + N_{AA} \frac{\partial \ln(p.f.)_{AA}}{\partial V}. \quad (23)$$

First we must insure that the portions of phase space assigned to N_A and N_{AA} in Eq. (16) do not overlap. This condition is automatically satisfied by the definition of the phase-shift⁸ we will employ in Eq. (5).

Second, we should be convinced that together the two partition functions encompass the entire phase space accessible to the N particles in Eq. (14). The interactions between $A+A_2$ and A_2+A_2 must ultimately modify the activities of N_A and N_{AA} at high pressures. However our concern is with strongly bonded dimers with deeply attractive ground states as represented by the alkali $X^1\Sigma_g^+$ potentials in Fig. 1, and it is reasonable to assume there is a wide regime where Eq. (23) is an accurate representation of the system. In any case, our goal in this paper is not to perform a complete analysis of the alkali vapors, but rather to obtain a complete understanding of the entity we commonly refer to as the diatomic molecule A_2 . Our intent is to develop a proper interpretation of the intrinsic thermodynamic variables that are conventionally associate with a given diatomic species^{5,14} and to

delineate the role of continuum states at high temperatures.

We begin by assigning the following partition function^{6,7,16,17} to the population of free atoms N_A ,

$$(p.f.)_A = V q_{tr}(m_A) \omega_A(T), \quad (24)$$

where ω_A is the electronic partition function for the atom

$$\omega_A(T) = \sum_{\alpha} \omega_{\alpha} e^{-E_{\alpha}/kT} \quad (25)$$

$$\approx \omega_0. \quad (26)$$

The ground state is denoted by $\alpha=0$, such that $E_0 \equiv 0$. The subtleties involved in the convergence of Eq. (25), together with the treatment of the ionization continua^{17,18} at high temperatures will be ignored. This would merely distract us from our primary goal of interpreting the nature of A_2 . For the alkali atoms, with a doubly degenerate $^2S_{1/2}$ ground state, we shall assume $\omega_A = \omega_0 = 2$.

Note that the entire volume V is assumed to be accessible to the center of mass motion of the atom in Eq. (24) which we treat as a point particle, i.e., as an ideal gas. The total Hamiltonian H_{AA} for the interaction of two atoms $A + A$ is equivalent to the Hamiltonian for the diatomic molecule A_2 for all interatomic distances \vec{R} .^{9,1} Therefore all two-body imperfections in the vapor are contained in the dimer partition function,

$$(p.f.)_{AA} = V q_{tr}(2m_A) Q_{tot} \quad (27)$$

when the total internal partition function

$$Q_{tot} = \sum_i \omega_i e^{-(E_{\alpha}(i) + E_{\alpha'}(i))/kT} Q_i \quad (28)$$

$$\approx Q_1 + 3Q_3 \quad (29)$$

is summed over the complete set of molecular electronic states i implied by Eqs. (1)-(3). The subset of molecular states $i(\alpha, \alpha')$ which dissociate into a particular pair of atoms $A(\alpha) + A(\alpha')$ satisfy the constraint,

$$\sum_i \omega_i(\alpha, \alpha') = \omega_\alpha \cdot \omega_{\alpha'}. \quad (30)$$

A pair of ground state alkali atoms, with $\omega_0 \omega_0 = 4$, correlates with the singly degenerate $X^1\Sigma_g^+$ and the triply degenerate $b^3\Sigma_u^+$ states in Fig. 1. These states will be indexed as $i=1$ and $i=3$ respectively throughout this paper, and we shall approximate Q_{TOT} by Eq. (29), consistent with our assumption in Eq. (26). Obviously for an accurate calculation of high temperature properties this assumption must be relaxed and the complete expressions (25) and (28) must be employed.

For each electronic state $|i\rangle$ we generate a set of electronic-rotational states $|i, \ell, m_\ell\rangle$ with nuclear angular momentum quantum number ℓ , and the $(2\ell+1)$ -degenerate space-fixed projections m_ℓ . These form a complete set which spans the polar coordinates \hat{R} for the orientation of the interatomic displacement \vec{R} between the interacting atoms, and we obtain an electronic-rotational potential $v_{i, \ell}(R)$ for each individual (i, ℓ) state. For sufficiently large R the potentials will approach the non-interacting limit,^{1,9}

$$U_{i, \ell}(R) = V_{i, \ell} - E_\alpha(i) - E_{\alpha'}(i) \underset{R \rightarrow \infty}{\sim} \frac{\hbar^2 \ell(\ell+1)}{m_A R^2}, \quad (31)$$

where the centrifugal potential depends on l and the reduced mass $m_A/2$. Often we can approximate $|i, l, m_l\rangle$ as a simple product of an electronic $|i\rangle$ and rotational $Y_{l, m_l}(R)$ wavefunction

$$|i, l, m_l\rangle \approx |i\rangle Y_{l, m_l}(\hat{R}) \quad (32)$$

with the result that the electronic-rotational potentials are additive, as in Eq. (6). In the most general case, depending on the particular Hund's coupling^{1,9,18,19} of electronic-rotational angular momentum employed in $v_{i, l}(R)$, the 'electronic' potential $v_i(R)$ in Eq. (6) may differ slightly from Eq. (7) and exhibit a generally negligible residual dependence on l . However, the Hund's case (b) form in Eq. (6) is perfectly valid for the $1\Sigma_g^+$ and $3\Sigma_u^+$ potentials that we shall ultimately treat, and this form will be employed throughout this study. Some typical $v_{i, l}(R)$ potentials for $\text{Li}_2(X\Sigma_g^+)$ are shown in Fig. 2.

The radial or vibrational motion of the dimer is described by the well-behaved solutions of the Schrodinger Equation,^{1,9,12}

$$\left[-\frac{\hbar^2}{m_A} \frac{\partial^2}{\partial R^2} + \epsilon - U_{i, l} \right] R_{i, l}(\epsilon, R) = 0 \quad (33)$$

such that the total electronic-rotational-vibrational wavefunction

$$|i, l, m_l, \epsilon\rangle = |i, l, m_l\rangle R_{i, l}(\epsilon, R)/R \quad (34)$$

defines what we might call the 'internal' energy for the collision of two atoms.

$$E_{i, l} = E_\alpha(i) + E_{\alpha'}(i) + \epsilon \quad (35)$$

Below threshold for dissociation in the potential $v_{i, l}$ when $\epsilon < 0$, we

obtain a finite set of true vibrational levels which we index by $v=0,1,\dots,v_{\max}(i,l)$. These occur at discrete values of E , such that

$$E = E_{i,l,v} < 0 \quad (36a)$$

and

$$R_{i,l}(E_{i,l,v}, R) \underset{R \rightarrow \infty}{\sim} 0 \quad (36b)$$

and the total internal energy of the dimer is quantized

$$E_{i,l,v} = E_{\alpha}(i) + E_{\alpha'}(i) + E_{i,l,v}. \quad (37)$$

Obviously vibrational levels which lie above the ground state limit, i.e., $E_{i,l,v} > 0$, and asymptotically correlate with excited state atoms in Eq. (37) are subject to predissociation^{11,12,18,20} and the definitions in Eq. (36) are somewhat ambiguous. However, the fact that such levels might not be truly stationary solutions, with discrete eigenvalues, has a negligible effect on the subsequent evaluation of thermodynamic properties. This phenomenon is thoroughly analyzed in the next section and should not distract us from our course at this point.

Above the dissociation limit the relative kinetic energy E defines a continuum of wavefunctions which exhibit the asymptotic boundary condition,^{1,6,7,8,9,12}

$$R_{i,l}(E, R) \underset{R \rightarrow \infty}{\sim} \sqrt{\frac{k}{\pi E}} \sin\left(kR - \frac{\pi l}{2} + \eta_{i,l}(E)\right), \quad (38)$$

where

$$k^2 = \frac{m_A E}{\hbar^2}. \quad (39)$$

The energy-dependent elastic scattering phase-shift $\eta_{i,l}(\epsilon)$ defines the elastic-scattering cross-section^{8,21} for the collision of atoms $A(\alpha) + A(\alpha')$ with relative kinetic energy ϵ , and relative orbital angular momentum, or partial wave quantum number l ,

$$\sigma_{i,l}(\epsilon) = \left[\frac{\omega_i}{\omega_{\alpha(i)} \omega_{\alpha'(i)}} \right] \frac{4\pi(2l+1)}{k^2} \sin^2 \eta_{i,l}(\epsilon). \quad (40)$$

Well-defined numerical procedures^{22,23} are available for evaluating the phase-shift from Eqs. (33) and (38) as a continuous function of ϵ , and, in particular we can subsequently evaluate the necessary derivative $\partial \eta_{i,l} / \partial \epsilon$ to arbitrary accuracy.

It should be emphasized that we have made a severe approximation in Eqs. (33) and (38) which restricts the formal theory. We have neglected any inelastic scattering processes between the colliding atoms $A(\alpha) + A(\alpha')$ associated with the electronic state $i(\alpha, \alpha')$ and have assumed only pure elastic scattering is important. However, it is our contention, based on a scattering theory analysis of diatomic continuum states using adiabatic electronic-rotational (AER) states,¹ that a rigorous treatment of the inelastic scattering will not modify the thermodynamic observables to any significant degree. In any case, Eq. (38) is perfectly valid for the alkali ground state atoms $A(^2S_{1/2}) + A(^2S_{1/2})$ we intend to study. There is negligible coupling between the $X^1\Sigma_g^+$ and $b^3\Sigma_u^+$ continuum states, and we need only consider the two elastic scattering phase shifts,

$$\eta_{1,l} \equiv \eta_{i,l}(X^1\Sigma_g^+) \quad (41)$$

$$\eta_{3,l} \equiv \eta_{i,l}(b^3\Sigma_u^+).$$

The complete Hamiltonian for the interaction of two atoms includes the kinetic energy operator^{6,8,16} associated with the coordinate $\vec{R}_{c,m}$ which locates the center-of-mass position of the collision complex with total mass $2m_A$ within the volume V . Note that the translational partition function $q_{tr}(2m_A)V$ contributed by the center-of-mass wavefunction in Eq. (27) is approximated as a perfect gas. This is valid if we may assume that higher-order A_2+A and A_2+A_2 interactions are negligible compared to $A+A$ and do not influence the activity of the dimer. Using Eq. (27) and (24) in (23) we obtain the equation of state given by Eq. (15).

The internal partition function Q_i for each i^{th} electronic state in Eq. (28) is deconvoluted into a rotational sum

$$Q_i = \sum_l (2l+1) q_{i,l} \quad (42)$$

over the radial partition functions $q_{i,l}$ associated with each specific electronic-rotational potential $v_{i,l}(R)$ ^{5,6,7}, i.e.,

$$q_{i,l} = \sum_{v=0, v_{max}(i,l)} e^{-\epsilon_{i,l,v}/kT} + \int_0^\infty d\epsilon e^{-\epsilon/kT} \frac{\partial \eta_{i,l}(\epsilon)}{\pi \partial \epsilon} \quad (43a)$$

$$= q_{i,l}(B) + q_{i,l}(C). \quad (43b)$$

Equation (43) contains both bound $q_{i,l}(B)$ and continuum $q_{i,l}(C)$ components and measures the departure from an ideal gas. If $v_i=0$, then $q_{i,l}=0$ for all l , and $Q_i=0$. This behavior is embodied in the definition of the phase shift $\eta_{i,l}(\epsilon)$ in Eq. (38). For non-interacting atoms the $v_{i,l}$ potential reduces to the simple centrifugal potential shown in Fig. 3 and the phase-shift, which measures departure from this ideal behavior, will vanish identically.^{1,8,9} Thus, Eq. (43) should be viewed as the difference in canonical phase space introduced by the interaction potential $v_i(R)$. If all interactions vanish, then $(p.f.)_{AA}=0$, and we retrieve the proper ideal gas law $P/kT = N/V$ for point particles in Eq. (15).

Each Q_i defined by Eqs. (42) and (43) is constructed from distinct bound (B) and continuum (C) state components as expressed in Eqs. (3)-(5), and a comparable separation transfers to the total internal partition function Q_{tot} in Eqs. (28) and (29),

$$Q_{tot} = Q_{tot}(B) + Q_{tot}(C). \quad (44)$$

Since the equilibrium constant K_{eq} in Eqs. (16) is proportional to Q_{tot} ,

$$K_{eq} = \frac{Q_{tot}}{\omega_A^2 q_{btr}(m_A/2)} \quad (45)$$

we obtain the unique separation of K_{eq} and the dimer population N_{AA} expressed in Eqs. (20) and (21). The same behavior applies to the virial coefficients B_i in Eq. (10), and to the mean second-virial coefficient $\langle B \rangle$ in Eq. (19) which is seen to be a canonical average over the individual virial coefficients associated with each $v_i(R)$ potential,

$$\langle B \rangle = -K_{eq} = \sum_i \frac{\omega_i}{\omega_A^2} e^{-(E_{\alpha}(i) + E_{\alpha'}(i))/kT} B_i \quad (46)$$

$$\approx \frac{(B_1 + 3B_3)}{4} \quad (47)$$

Equation (47) applies to our specific assumptions for the alkali dimers.

The subsequent breakdown of $K_{eq}(C)$, $Q_i(C)$, $B_i(C)$ and $q_i(C)$ into metastable and free-continuum contributions requires an analysis of the quantum mechanical phase-shift derivative $\partial \eta_{i,l}(\epsilon)/\pi \partial \epsilon$.

III. CONTINUUM PHASE SHIFTS AND METASTABLE STATES

The electronic potentials calculated by Konowalow *et al*¹⁵ for Li_2 and Na_2 are shown in Fig. 1. We shall use the $X^1\Sigma_g^+$ state of Li_2 to demonstrate the contribution of the continuum phase-shifts and metastable states to the vibrational partition function in Eq. (43). Specific electronic-rotational potentials $v_{i,l}(R)$ are plotted in Fig. 2 for $l=0, 100, 130$, and 180 as the centrifugal contribution to Eq. (6) progressively 'fills' the attractive $v_i(R)$ potential until only a pure monotonically repulsive potential exists. Explicit calculations will be presented for these representative angular momentum states.

Using the Gordon algorithm^{22,23} to solve Eq. (33) we calculate that a total of $v_{\text{tot}} = (v_{\text{max}} + 1) = 42$ bound vibrational levels exist in the $v_{i,0}(R) = v_i(R)$ potential which has a dissociation energy of 8450 cm^{-1} . For $l=100$ the $v_{i,100}$ potential is only 2560 cm^{-1} attraction and supports the $v_{\text{tot}}=11$ true bound states plotted in Fig. 4. However, behind the rotational barrier at $R=R_{\text{bar}}$ for any $l>0$ we may expect a number of quasi-bound states, or metastable states^{3,5,10,11,12} to exist at certain 'eigenvalues' of the incident kinetic energy (See Fig. 3)

$$E = E_{i,l,m} > 0. \quad (48)$$

These energies can be estimated by the same procedure used to obtain the true bound states in Eq. (35) by using an approximate potential $\tilde{v}_{i,l}(R)$ in place of $v_{i,l}(R)$ in Eq. (33), such that

$$\tilde{v}_{i,l}(R) \equiv U_{i,l}(R) \quad R < R_{\text{bar}} \quad (49)$$

$$\tilde{v}_{i,l}(R) \equiv U_{i,l}(R_{\text{bar}}) \quad R \geq R_{\text{bar}}.$$

For $\ell=100$ we obtain the $m_{\text{tot}}=7$ metastable levels portrayed in Fig. 4. We know of course, that these states are ultimately 'unstable' because of tunnelling through the rotational barrier,³ and we might choose to associate an energy width with each level

$$\Gamma_{i,\ell,m} = \hbar / \tau_{i,\ell,m} \quad (50)$$

which reflects the expected lifetime $\tau_{i,\ell,m}$ of a molecule 'prepared' in such a non-stationary state.¹³ As long as

$$kT \gg \Gamma_{i,\ell,m} \quad (51)$$

we can expect that the metastable nature of the levels are of insignificant consequence and the $\epsilon_{i,\ell,m} > 0$ eigenvalues can be treated on an equal footing with the true bound states $\epsilon_{i,\ell,v} < 0$. This can be demonstrated by the exact quantum mechanical results.

The rigorous solutions of Eq. (33) for $v_{i,\ell}(R)$ yield a continuum of wavefunctions with the boundary conditions imposed by Eq. (38) whenever $\epsilon > 0$. If we were to examine the amplitude of the wavefunctions $R_{i,\ell}(\epsilon, R)$ behind the barrier we would find a negligible probability of observing a pair of atoms with an interatomic displacement $R < R_{\text{bar}}$, except in the vicinity of $\epsilon \approx \epsilon_{i,\ell,m}$. This is reflected at $R \sim \infty$ by a rapid variation of the phase-shift $\eta_{i,\ell}(\epsilon)$ which takes the following form, near a metastable, or resonant energy,^{8,12,13,21}

$$\eta_{i,\ell}(\epsilon) \underset{\epsilon \rightarrow \epsilon_{i,\ell,m}}{\approx} \eta_{i,\ell}^{\text{free}}(\epsilon_{i,\ell,m}) - \tan^{-1} \left(\frac{\Gamma_{i,\ell,m}/2}{\epsilon - \epsilon_{i,\ell,m}} \right) \quad (52)$$

Such behavior is observed in the quantum mechanical phase shift for $l=130$ in the vicinity of the $m=8$ metastable level which was calculated by the procedure in Eq. (49) to exist at $\tilde{\epsilon}_{i,130,8} = 1947.50 \text{ cm}^{-1}$. The calculated data²⁴ is plotted in Fig. 5. The width $\Gamma = .00255 \text{ cm}^{-1}$ obtained from the fit to Eq. (52) corresponds to a lifetime of 10^{-9} sec, and the position, $\epsilon_{i,l,m} = 1947.775 \text{ cm}^{-1}$, is only slightly shifted from the approximate result. Note that the phase increases by modular- π in passing from $\epsilon < \epsilon_{i,l,m}$ to $\epsilon > \epsilon_{i,l,m}$. Figure 6 shows similar behavior for the top-most resonance, $m=9$, which lies about 15 cm^{-1} below the rotational barrier at $\epsilon_{\text{bar}} = 2056 \text{ cm}^{-1}$. In this case the width obtained from Eq. (52) is $\Gamma \approx 3.2 \text{ cm}^{-1}$, with a resultant lifetime of 10^{-12} sec.

The derivative $\partial \eta_{i,l} / \partial \epsilon$ simply yields the normalized Lorentzian line shape^{8,13,21} associated with a width $\Gamma_{i,l,m}$, i.e.,

$$\frac{\partial \eta_{i,l}(\epsilon)}{\pi \partial \epsilon} \underset{\epsilon \rightarrow \epsilon_{i,l,m}}{\sim} \frac{\Gamma_{i,l,m} / 2\pi}{(\epsilon - \epsilon_{i,l,m})^2 + \Gamma_{i,l,m}^2 / 4}, \quad (53)$$

and the contribution to the continuum partition function (31) in the vicinity of any resonance is bounded by unity, i.e.,

$$\int_{\epsilon_{i,l,m} - \Delta}^{\epsilon_{i,l,m} + \Delta} d\epsilon e^{-\epsilon/kT} \frac{\partial \eta_{i,l}}{\pi \partial \epsilon} \underset{\Delta, kT \gg \Gamma_{i,l,m}}{\approx} e^{-\epsilon_{i,l,m}/kT} \quad (54)$$

Note that similar considerations will apply to any metastable or predissociating state contributing to the dimer partition functions, and not merely to rotational predissociation through centrifugal barriers; the only restriction to consider is the criterion in Eq. (51). It should also be emphasized that the role of metastable molecules in

equilibrium properties is independent of the lifetime of the state, and is not contingent on any dynamic assumptions,^{3,4} such as requiring the collision frequency between free atoms to exceed the predissociation rate. This can be appreciated by examining the nature of the phase-shift more closely.

Scattering theory²¹ predicts that two colliding atoms $A(\alpha') + A(\alpha)$ progressing on the molecular potential $v_i(R)$ with orbital angular momentum l , and relative kinetic energy ϵ , will experience a 'delay time' or collision lifetime $(\Delta t)_{i,l,\epsilon}$ relative to two non-interacting atoms with the same dynamic variables, such that

$$(\Delta t)_{i,l,\epsilon} = 2\hbar \frac{\partial \eta_{i,l}}{\partial \epsilon} . \quad (55)$$

Thus the continuum partition function $q_{i,l}(C)$ in Eq. (43) may be expressed as follows,²⁵

$$q_{i,l}(C) \equiv \int_0^\infty e^{-\epsilon/kT} \frac{(\Delta t)_{i,l,\epsilon}}{h} d\epsilon . \quad (56)$$

A positive delay time means a positive contribution to the partition function and a higher density of states compared to the free atom interactions. This is particularly evident in the vicinity of a resonance where Eq. (53) predicts a peaked, positive delay time

$$(\Delta t)_{i,l,\epsilon} \underset{\epsilon \rightarrow \epsilon_{i,l,m}}{\sim} \frac{4\hbar}{\Gamma_{i,l,m}} \equiv 4\tau_{i,l,m} \quad (57)$$

which increases with the lifetime of the metastable state. In contrast, a negative delay time, as occurs for a repulsive hard-core potential, imposes a negative contribution on $q_{i,l}(C)$, which is, in fact, equivalent to the net loss of phase space associated with the

excluded volume defined by the interaction potential.

For real potentials, such as in Fig. 2, there will be both negative and positive contributions due to the repulsive and attractive regions of interaction. However, we may use the analysis in Eqs. (53) and (54) to isolate the dominant positive contribution of the resonance states to the continuum partition function, i.e.,

$$\begin{aligned}
 q_{i,l}(c) &= \sum_m e^{-E_{i,l,m}/kT} + \int_0^\infty d\epsilon e^{-\epsilon/kT} \frac{\partial \eta_{i,l}^{\text{free}}(\epsilon)}{\pi \partial \epsilon} \\
 &= q_{i,l}(M) + q_{i,l}(F). \quad (58)
 \end{aligned}$$

The 'free-continuum' component $q_{i,l}(F)$ embodies all the remaining non-resonant energy dependent contributions of $\eta_{i,l}(\epsilon)$ between the resonances for $\epsilon \leq \epsilon_{\text{bar}}$ in Fig. 4, as well as the entire $\eta_{i,l}(\epsilon)$ dependence above the rotational barrier.³ Unless one is devising experiments in which the dimer metastable states are directly 'observable' the only pertinent quantity in the analysis of the thermodynamic properties is the total continuum partition function $Q_i(c)$ and this deconvolution into components is only for our convenience.

If the interaction $v_i(R)$ between two atoms vanishes only continuum solutions to Eq. (33) exist and the asymptotic form of the radial function in Eq. (38) is equivalent to the spherical Bessel function ^{1,8,9,12,21} $j_l(kr)$ for the partial wave l , where the phase shift is identically zero. Thus the phase-shift for an arbitrary potential is a measure of the deviation from the ideal gas, or point particle, interaction which leads to the definition of the delay time in Eq. (55).

The boundary condition in Eq. (36) is indeterminate by modular π ,

and we must convert the principal value of $\eta_{i,l}(\epsilon)$ obtained from the numerical solution of Eq. (33) into a continuous, analytic function of $\epsilon > 0$ which can be differentiated and used in Eq. (56). Levinson's theorem^{5,8,12,26,27} demonstrates that the change in the phase shift between $\epsilon=0$ and $\epsilon=\infty$ is simply related to the total number of bound states $v_{\text{tot}}(i,l)$ that exist in the $v_{i,l}(R)$ potential,

$$\eta_{i,l}(0) - \eta_{i,l}(\infty) = \pi v_{\text{tot}}(i,l), \quad (59)$$

and, since $\eta_{i,l}(\infty)=0$ for molecular potentials v_i which are typically finite at $R=0$, we require a threshold value of $\eta_{i,l}(0) = \pi v_{\text{tot}}(i,l)$. The actual threshold behavior for a potential which approaches $v_i \sim -CR^{-6}$ at large R is known to be^{8,26,27}

$$\begin{aligned} \eta_{i,l} &\underset{\epsilon \rightarrow 0}{\sim} \pi v_{\text{tot}}(i,l) + \mathcal{O}(k^{2l+1}) \quad \text{for } l=0,1 \\ &\underset{\epsilon \rightarrow 0}{\sim} \pi v_{\text{tot}}(i,l) + \mathcal{O}(k^4) \quad \text{for } l \geq 2 \end{aligned} \quad (60)$$

and we could analytically continue the numerically derived phase shifts to obtain a unique value of $\eta_{i,l}(\epsilon)$ for all ϵ .

Fortunately we have found an excellent approximation, based on the WKB approximation,^{5,28} which supplies a simple, analytic, single-valued estimate of $\eta_{i,l}(\epsilon)$ at any energy.

$$\begin{aligned} \eta_{i,l}^{\text{WKB}}(\epsilon) &\underset{\substack{\epsilon > 0 \\ U_i \neq 0}}{=} \left(\frac{m_A}{\hbar^2}\right)^{1/2} \left[\int_0^\infty dR \sqrt{\epsilon - U_{i,l}(R)} \right. \\ &\quad \left. - \int_0^\infty dR \sqrt{\epsilon - \frac{l(l+1)\hbar^2}{m_A R^2}} \right] + \frac{\pi}{4} \delta_{0,l}. \end{aligned} \quad (61)$$

The symbol \int_0^∞ is meant to indicate the exclusion of all non-classical regions of phase space from the integrals, which occurs whenever $\sqrt{\quad}$ becomes imaginary. When used in Eq. (56) and summed over ℓ in Eq. (42), this approximation is equivalent to the classical contribution of $B_i(C)$ to Eqs. (12) and (13). In the following plots we will compare both $\eta_{i,\ell}$ and $\eta_{i,\ell}^{\text{WKB}}$ and find extraordinary agreement except right at threshold, and in the vicinity of resonances. As already seen in Figs. 5 and 6, Eq. (61) transforms the step-like increases in $\eta_{i,\ell}(\epsilon)$ at $\epsilon \approx \epsilon_{i,\ell,m}$ into a smoothly varying function. This is equivalent to reversing the procedure in Eq. (54) and substituting a continuous function to represent the resonant contribution to the partition functions. The final results will be equivalent whenever $kT > (\epsilon_{i,\ell,m+1} - \epsilon_{i,\ell,m})$, and thus we can quantitatively justify the use of the classical theory.

The phase-shift for $\ell=0$ is plotted in Fig. 7. It falls fairly rapidly from its threshold value of 42π , introducing a large negative contribution to Eq. (56). At extremely large energies the phase actually becomes negative as the repulse core of the $v_{i,0}$ potential in Fig. 2 becomes dominant, and then slowly progresses to zero as $\epsilon \rightarrow \infty$. A simple physical interpretation of the negative contribution near threshold is that the rapid acceleration of the atoms as they pass over

the deeply attractive well causes the atoms to spend less time in this region of phase space, i.e., $\langle \Delta t \rangle_{i,l,\epsilon} < 0$, compared to free atoms. It is interesting to note that, at infinite temperature, there is an exact cancellation of the positive bound state contribution

$$q_{i,l}(B) \underset{kT \rightarrow \infty}{\sim} U_{tot}(i,l) \quad (62)$$

and the negative continuum state contribution predicted by Levinson's theorem,

$$q_{i,l}(C) \underset{kT \rightarrow \infty}{\sim} -U_{tot}(i,l) \quad (63)$$

such that $q_{i,l}$ in Eq. (43) is identically zero. In any case it should be apparent that neglect of the continuum phase space in estimating $q_{i,0}$ at high temperature will overestimate the magnitude of the partition function. This is demonstrated in Fig. 8 where the various contributions of $q_{i,l}(B)$, $q_{i,l}(M)$ and $q_{i,l}(F)$ for $\text{Li}_2(X^1\Sigma_g^+)$ are plotted as a function of l for $T = 6000^\circ\text{K}$. A similar plot for $\text{Li}_2(^3\Sigma_u^+)$ is shown in Fig. 9. These quantities were actually calculated using the WKB theory but the results are in quantitative agreement with the quantum values.

It should be pointed out that, for homonuclear molecules with

nuclear spin $I=0$, only even values of ℓ satisfy the antisymmetrization of the total dimer wavefunction,¹⁹ and alternate values of ℓ are missing from the summation in Eq. (42). This effect is equivalent to the ubiquitous 'symmetry factor' $\sigma=2$ which is used to reduce the magnitude of the classical partition functions for homonuclear species.^{6,7,16,} The fact that Li has a nuclear spin $I=1$ gives rise to the same complications that occur in the $D_2(X^1\Sigma_g^+)$ state^{16,19} with an alternating weighting of 2/3:1/3 assigned to ℓ =even and ℓ =odd eigenvalues respectively. However, the evaluation of statistical properties at high temperatures is quite insensitive to this subtlety and we shall simply sum over even values of ℓ with a weighting of unity.

The phase shift for $\ell=100$ is shown in Fig. 10 and should be examined in comparison to Fig. 4. The threshold value 11π reflects the presence of $v_{\text{tot}}=11$ bound states in the $v_{i,100}(R)$ potential. There is a rapid increase in the phase to a value $\eta_{i,100} \simeq 18\pi$ at the top of the rotational barrier at $\epsilon \simeq 1000 \text{ cm}^{-1}$, concomitant with the 7 metastable states which are predicted to exist behind the barrier. The WKB phase shift predicts a smooth monotonic increase from threshold to $\epsilon = 1000 \text{ cm}^{-1}$. The actual quantum mechanical phase shift behaves as in Fig. 5 and remains relatively flat, with an abrupt series of step-like increases by modular- π at each metastable resonance position. Above $\epsilon = 1000 \text{ cm}^{-1}$ both phases coincide and contribute first positive, $\frac{\partial \eta}{\partial \epsilon} < 0$, and their negative, $\frac{\partial \eta}{\partial \epsilon} > 0$, components to the integral in Eq. (56). The resultant $q_{i,100}(H)$ and $q_{i,100}(F)$ contributions at $T=6000^\circ$ can be seen in Fig. 8.

The phase for $\ell=130$ in Fig. 11 must obviously start at $\eta_{i,\ell}(0)=0$

since the potential in Fig. 3 is seen to support no bound states below threshold. There is a negligible increase in phase until the minimum in the $v_{i,130}$ potential becomes accessible at $\epsilon \approx 706 \text{ cm}^{-1}$ and then there is a rapid rise to 9π as the nine metastable states contribute to the scattering. Again we have plotted the smoothly varying WKB phase which smooths the step-like quantum phase. We shall argue that, for kT large compared to the metastable spacings, the monotonic function, which leads to exact agreement with the classical partition function, is an adequate approximation.

Finally, we present the $\ell=180$ phase in Fig. 12. As seen in Fig. 2 this potential supports neither bound, nor metastable states, and we obtain a smoothly varying phase-shift which predominately makes positive contributions to the partition function due to the deeply attractive well in the $v_i(R)$ electronic potential.

The calculated electronic partition functions for the singlet, Q_1 , and triplet, Q_3 , states of Li_2 and Na_2 are presented in Tables I and II. The tabulated ratios $Q_i(M)/Q_i(B)$ and $Q_i(F)/Q_i(B)$ give a measure of the importance of the various components of the continuum states as the temperature is increased. Obviously these dissociative states are most significant in the shallow $b^3\Sigma_u^+$ potential, but the neglect of $Q_i(M)$, or $Q_i(F)$ can not be justified even for the strong, chemically bonded $X^1\Sigma_g^+$ state.

IV. DISCUSSION OF RESULTS

Given the partition functions for Li_2 and Na_2 we can derive the usual thermodynamic variables for these molecules. We have compared our calculations to the JANAF tables⁵ and find substantial deviations at temperatures above 2000°K . We concluded that any tabulations of thermodynamic properties, such as the JANAF tables, which rely on a Dunham expansion of the molecular term values must ultimately fail at high temperatures. In particular the anharmonicity substitutes a spuriously high density of discrete states in place of the true continuum states. These meaningless states tend to over estimate the molar entropy and enthalpy. This fault is especially evident in the tabulated molar heat capacity C_p which often increases monotonically to unrealistically high values. More sophisticated calculations¹⁰ which attempt to evaluate the finite sums over bound, Eq. (4), and metastable, Eq. (9), states yield substantially more reliable results, but this approach still suffers from the neglect of the free-continuum contribution $Q_i(F)$ in Eq. (8). This can be seen in Tables I and II.

In this discussion we shall consider the one observable parameter that is derivable from the thermodynamic analysis; the equilibrium constant K_{eq} , or equivalently the second virial coefficient $\langle B \rangle = -K_{\text{eq}}$. We can not measure the molar Gibb's free energy, or enthalpy, or entropy of an isolated alkali dimer. However we can confine a prescribed number of atoms N in a volume V at temperature T and measure the total pressure P of the resultant vapor. Thus we can obtain the total population of dimers from the equation of state (15) and the constraint in Eq. (14)

$$N_{AA} = N_{AA}(N, V, T) = P_{AA} V / RT = (N - PV / RT). \quad (64)$$

Given our definition of the dimer embodied in our construction of the partition functions (24) and (27) we may equate K_{eq} in Eq. (16) to directly measurable quantities.

$$K_{eq} \equiv RT K_P = \frac{RT P_{AA}}{(P - P_{AA})^2}. \quad (65)$$

The various components of K_{eq} in Eq. (20) manifest themselves directly in the predicted dimer population (21) and make explicit contributions to the observable equation of state (22).

The solid curves in Fig. 13 present K_{eq} for Li_2 and Na_2 when the entire contribution of singlet and triplet ground states are included in Eq. (47). These are calculated using the classical expression in Eq. (12). This is the equilibrium constant we would expect to extract from Eq. (65) assuming that no excited electronic states of the atoms and molecules influence our observations of N_{AA} in Eq. (64). Actually electronic excitations seem to influence the thermodynamics above about $4000^{\circ}K^{29,30}$ and our results at higher temperatures must be viewed as only a partial analysis of the real alkali vapor. The calculations in the range $1000-3000^{\circ}K$ should be quite reliable and are summarized in Table III.

The dashed curve in Fig. 13 is the resultant $K_{eq} (^1\Sigma_g^+)$ obtained if we exclude the $^3\Sigma_u^+$ contribution B_3 in Eq. (47). In this case Eq. (16) only yields $N_{AA} = N_{AA} (^1\Sigma_g^+)$ and, analogous to Eq. (22), imperfections due to the missing triplet contribution $N_{AA} (^3\Sigma_u^+) \approx -3B_3 N_A^2 / (4V)$ must yield non-ideal behavior in the monomer component of the equation of

state. The effect is particularly pronounced in the Na_2 vapor, where the large negative contribution due to the free-continuum component $Q_3(F)$ in Table II causes a 48% reduction in K_{eq} at $10,000^\circ\text{K}$. Fortuitously this just about cancels the positive $Q_1(F)$ contribution due to the attractive singlet state and it might seem reasonable to use the usual approximation^{5,10} $Q_{tot} \approx Q_1(B) + Q_1(M)$ and neglect all free-continuum contributions entirely. However in Table I we see that $Q_3(F)$ is much reduced in Li_2 and there is never any assurance that a truncated summation over bound, or bound and metastable states, will lead to an accurate Q_{tot} . The only rigorous procedure is to completely evaluate both Q_1 and Q_3 .

Direct comparisons between this calculation and the K_p tabulated in the JANAF Tables,¹⁴ which employ Dunham type expansions for the molecular eigenvalues, are complicated by many factors, and especially by the substantial discrepancy between the H_{298}^0 predicted by the Konowalow et al¹⁵ potentials, and the old values of H_{298}^0 employed in the Tables. Since this quantity is systematically subtracted from the tabulated molar thermodynamic variables for the dimer, comparisons with the JANAF Tables are best considered in reference 5.

Obviously the thermodynamics of Li_2 is dominated by the deeply attractive $^1\Sigma_g^+$ state in Fig. 1, with $D_e = 8450 \text{ cm}^{-1}$. If we ignore this state, and only consider the equilibrium properties associated with the weakly attractive $^3\Sigma_u^+$ potential ($D_e = 292 \text{ cm}^{-1}$), we can simulate the behavior of a loosely bound dimer. This is done in Fig. 14, where the solid curve gives the equilibrium constant obtained by using $\langle B \rangle = B_3$ in

Eq. (47). The dashed curve results from excluding the continuum, and using $\langle B \rangle = B_3(B)$. The qualitative features of these calculations can be expected to mimic the equilibrium properties of, say, the group IIA dimers, Be_2 , Mg_2 , Ca_2 , and the group IIB dimers, Zn_2 , Cd_2 , Hg_2 , of the periodic table all of which have shallow $X^1\Sigma_g^+$ van-der-Waal ground states.

Because of the dominant contribution of the free-continuum component $B_3(F)$, the excluded volume introduced by the repulsive portion of the $^3\Sigma_u^+$ potential causes B_3 to become positive at 5400°K. This result could be anticipated from Fig. 8, where the individual rotational contributions to Q_3 are negative for all λ . For such a system the molar thermodynamic properties, such as $G^0 \propto \ln Q_3$, are ill defined. We could content ourselves by defining the dimer in terms of the bound-state portion of the partition function $Q_3(B)$ in Tables I and II, or possibly by the combination, $Q_3(B) + Q_3(M)$, and tabulate the resultant thermodynamic variables accordingly. However, without an understanding that the 'monomer' imperfections attributable to $B_3(F)$ make a dominant contribution to Eq. (22b) we could not hope to use the thermodynamic tables to predict the observable properties of the vapor.

After this elaborate analysis of diatomic thermodynamics, let us ask what constraints we should place on the use of current thermodynamic tabulations, and what aspects of this polemic can be ignored?

Obviously at low to intermediate temperatures, when $Q_{\text{tot}}(B) \gg Q_{\text{tot}}(C)$, we can ignore the entire continuum and metastable problem. At all pressures the conventional spectroscopic analysis, using the Dunham expansion, should be adequate.

At higher temperatures the importance of the continuum states depends on the ratio N_{AA}/N_A . At elevated pressures, with large departures from the ideal gas law $PV = NkT$, the deviations from the JANAF predictions can be substantial. Particularly if our goal is to obtain a quantitative description of the equation of state our only course is to follow the prescriptions in this paper and evaluate accurate Q_i partition functions using Eq. (12). Of course in this case the analyses must be extended to include assessments of higher order interactions in the vapor. For instance, it is known³¹ that the alkali trimers are significantly bound. However, this only emphasizes the need for accurate evaluation of the dimer equilibrium, especially if we hope to use apparent departures from the expansion in Eq. (15) to estimate these higher-order effects.

At high temperatures and modest pressures, when $2N_{AA}/N_A$ is appreciably less than one, we would still require accurate partition functions to obtain a reliable equation of state. However, if the thermodynamics is to be used merely to predict concentrations of specific internal quantum states $A_2(i, \ell, v)$ with electronic-rotational-vibrational energy $E_{i, \ell, v}$, i.e.,

$$N_{AA}(i, \ell, v) = N_A^2 \left\{ \frac{e^{-E_{i, \ell, v}/kT} \omega_i (2\ell+1)}{\omega_A^2 q_{tr}(m_A/2)} \right\}, \quad (66)$$

small deviations of $N_A = N [1 - 2N_{AA}/N]$ from $N_A \approx N$ may often be ignored, or adequately corrected using existing thermodynamic data. However, we now require accurate evaluation of the molecular eigenvalues $E_{i, \ell, v}$, and at high temperatures we can expect an appreciable percentage of dimer molecules to exist in the continuum states associated with the partition

functions $q_{i,l}(C)$ and $Q_i(C)$ in Eqs. (43) and (5). In the case of van-der-Waals type molecules, such as the $^3\Sigma_u^+$ state of Li_2 , this temperature is not remarkably high, and, as seen in Table I, even for the deeply attractive $^1\Sigma_g^+$ ground state of Li_2 approximately 15% of the molecules are metastable, and 12% exist in the free-continuum at 6000°K .

V. SUMMARY AND RECOMMENDATIONS

At high temperatures the metastable state partition function, $Q_{\text{tot}}(\text{M})$, and the free-continuum partition function, $Q_{\text{tot}}(\text{F})$, are important components in the total internal partition function, $Q_{\text{tot}} = Q_{\text{tot}}(\text{B}) + Q_{\text{tot}}(\text{M}) + Q_{\text{tot}}(\text{F})$, for a diatomic molecule. We could choose to represent the dimer simply in terms of the finite set of true molecular bound states which define $Q_{\text{tot}}(\text{B})$, but then we must be cognizant of the fact that all continuum contributions to the molecular phase space, $Q_{\text{tot}}(\text{C}) = Q_{\text{tot}}(\text{M}) + Q_{\text{tot}}(\text{F})$, have merely been transferred to a new definition of the monomer which can cause marked imperfections in the activity of what we now choose to call the atom population.

Although the metastable component $Q_{\text{tot}}(\text{M})$ is always positive, the remaining contributions of the continuum, $Q_{\text{tot}}(\text{F})$, can be either positive or negative with a magnitude that can match or exceed $Q_{\text{tot}}(\text{M})$. Thus there is no assurance that a dimer defined by the combination of bound and metastable states, $Q_{\text{tot}}(\text{B}) + Q_{\text{tot}}(\text{M})$, will yield any superior results.

The safest course is to use the total partition function Q_{tot} to define the thermodynamic properties of the dimer since there is never any doubt that the monomer is properly described as a perfect gas. In any case it is imperative to use a mutually consistent scheme when defining the dimer partition function for diverse species. Otherwise substantial errors can be introduced into the calculation of equilibrium distributions in mixed vapors.

We offer two recommendations for the calculation of thermodynamic properties at high temperatures:³³

- 1) All high temperature calculations should begin with the interatomic potentials $v_i(R)$ for each electronic state included in the partition function. The spectroscopic parameters obtained from an expansion of observed term values can be used as input to, say, an RKR potential³² for the state. However, it is imperative to use potentials, such as in Fig. 2, which properly represent the dissociation process and therefore introduce the correct density of states for the molecular continua.
- 2) We have shown⁵ that the classical approximation to the partition function is extremely accurate at high temperatures. The simplest course is to use the electronic potentials $v_i(R)$ in the classical expressions and numerically evaluate the complete partition function Q_i in Eq. (12). This result contains all contributions to the molecular phase space, including the metastable and free-continuum components. The monomer is then rigorously represented as an ideal gas, and all imperfections are embodied in our definition of the dimer. For shallow van-der-Waal potentials, where Q_i may become negative, there will be some subtleties in this procedure. However, the analysis we have presented⁵ in terms of virial coefficients for the monomer can rigorously handle this occasional difficulty.

ACKNOWLEDGEMENT

This work is supported in part by the Air Force Office at Scientific Research, Contract No. AFCSR-ISSA-80-0012.

References

1. F. H. Mies, *Molec. Phys.* 41, 973 (1980)
2. T. L. Hill, *J. Chem. Phys.* 23, 617 (1955)
3. D. E. Stogryn and J. O. Hirschfelder, *J. Chem. Phys.* 31, 1531 (1959)
4. S. K. Kim and J. Ross, *J. Chem. Phys.* 42, 263 (1965)
5. F. H. Mies and P. S. Julienne, submitted *J. Res. Nat. Bur. Stand.*
6. O. K. Rice, Statistical Mechanics Thermodynamics and Kinetics (W. H. Freeman, San Francisco, 1967) chapters 8, 11, 16.
7. J. O. Hirschfelder, C. F. Curtiss and R. B. Bird, Molecular Theory of Gases and Liquids (Wiley, New York, 1954) chapter 6
8. N. F. Mott and H. S. W. Massey, The Theory of Atomic Collisions (3rd Ed., Oxford, London, 1965)
9. F. H. Mies, *Molec. Phys.* 41, 953 (1980)
10. R. C. Feber and C. C. Herrick, U.S. AEC LA 3597 (1966)
11. L. V. Gurvich, I. V. Veits, V. A. Medvedev, G. A. Khachkuruzov, V. S. Yungman, G. A. Bergman et al, "Termodinamicheskie Svoistva Individual'nykh Veshchestv", (Thermodynamic Properties of Individual Substances), V. P. Glushko, gen. ed., Vol. 1, part 1 (1978) Izdatel'stvo "Nauka" Moscow
12. F. H. Mies and P. S. Julienne, in preparation
13. U. Fano, *Phys. Rev.* 124, 1866 (1961)
14. D. R. Stull and H. Prophet, JANAF Thermodynamic Tables, (2nd Ed., Nat. Stand. Ref. Data Ser., Nat. Bur. Standards 37, 1971)
15. D. D. Konowalow and M. L. Olson, *J. Chem. Phys.* 71, 450 (1979); D. D. Konowalow, M. E. Rosenkrantz and M. L. Olson, *J. Chem. Phys.* 72, 2612 (1980)
16. G. S. Rushbrooke, Introduction to Statistical Mechanics (Oxford, London, 1949)
17. K. S. Pitzer, *J. Chem. Phys.* 70, 393 (1979)

18. L. D. Volyak, Thermodynamic Properties of Gases and Liquids, V. A. Rabinovich, Ed., (Committee of Standards, USSR, Translated by Israel Program for Scientific Translations, 1970, TT69-55091) p. 43
19. G. Herzberg, Spectra of Diatomic Molecules, (2nd Ed., Van Nostrand, Princeton, 1950)
20. P. S. Julienne, J. Molec. Spectros. 56, 270 (1975)
21. T.-Y. Wu and T. Ohmura, Quantum Theory of Scattering (Prentice-Hall, Englewood Cliffs, N.J. 1962)
22. R. Gordon, J. Chem. Phys. 51, 14 (1969); Methods Comput. Phys. 10, 81 (1971)
23. R. I. LeRoy and R. B. Bernstein, J. Chem. Phys. 49, 4312 (1968); R. B. Bernstein, J. Chem. Phys. 33, 795 (1960)
24. We chose a principal value for $\tan^{-1}x$ such that $\tan^{-1}(-\infty) = 0$ and $\tan^{-1}(+\infty) = -\pi$
25. This quantum expression, which replaces each microcanonical volume of phase space with an average time-delay for each energy state, bears some interesting comparisons to the ergodic and semi-ergodic problem; e.g., R. C. Tolman, The Principles of Statistical Mechanics (Oxford, London, 1938); T. L. Hill, Statistical Mechanics (McGraw-Hill, New York, 1956)
26. J. R. Taylor, Scattering Theory: The Quantum Theory of Nonrelativistic Collisions (Wiley, New York, 1972)
27. M. L. Goldberg and K. M. Watson Collision Theory (Wiley, New York, 1964)
28. L. D. Landau and E. M. Lifshitz, Quantum Mechanics: Non-Relativistic Theory (Pergamon Press, London, 1958)
29. F. W. Reiter, Z. Naturforsch. 28a, 1676 (1973)
30. R. I. Artym, High Temp. 6, 966 (1968); translated from Teplofizika Vysokikh Temp. 6, 11010 (1968)
31. C. H. Wu, J. Chem. Phys. 65, 3181 (1976); R. L. Martin and E. R. Davidson, Molec. Phys. 35, 1713 (1978)
32. R. N. Zare, A. L. Schmeltekopf, W. J. Harroff, and D. L. Albritton, J. Molec. Spectros. 46, 37 (1973)
33. These recommendations were originally proposed by C. W. Beckett³⁴ and L. Haar³⁵, but have not been properly exploited.

34. C. W. Beckett, and L. Haar, Proc. of the Joint Conference on Thermodynamic and Transport Properties of Fluids, Inst. of Mechanical Engineers, London, p. 27 (1957).
35. L. Haar, "Kinetics, Equilibria and Performance of High Temperature Systems," Proc. of the First Conference of the Western States Section of the Combustion Institute, Butterworth and Co., Limited, London, 1959.

TABLE I. Partition Functions for $\text{Li}_2(X^1\Sigma_g^+)$ and $\text{Li}_2(b^3\Sigma_u^+)$

$T(^{\circ}\text{K})$	$Q_1^{(a)}$	$\frac{Q_1(M)}{Q_1(B)}$	$\frac{Q_1(F)}{Q_1(B)}$	$Q_3^{(a)}$	$\frac{Q_3(M)}{Q_3(B)}$	$\frac{Q_3(F)}{Q_3(B)}$	$\frac{-(G^0 - H_{298}^0)}{T}$
500	9.835 (12)	0.0000	-0.0000	6.400 (3)	0.3578	0.6105	47.955
1000	2.162 (8)	0.0001	+0.0000	6.790 (3)	0.4226	0.9368	51.565
1500	8.925 (6)	0.0036	0.0005	6.755 (3)	0.4460	0.9942	54.411
2000	2.216 (6)	0.0172	0.0036	6.395 (3)	0.4580	0.8964	56.664
2500	1.078 (6)	0.0403	0.0117	5.805 (3)	0.4652	0.6956	58.502
3000	7.125 (5)	0.0679	0.0251	5.045 (3)	0.4702	0.4214	60.028
3500	5.525 (5)	0.0965	0.0431	4.155 (3)	0.4738	0.0922	61.313
4000	4.682 (5)	0.1238	0.0646	3.162 (3)	0.4764	-0.2799	62.411
4500	4.188 (5)	0.1491	0.0888	2.088 (3)	0.4785	-0.6862	63.361
5000	3.877 (5)	0.1721	0.1149	9.460 (2)	0.4802	-1.120	64.193
5500	3.671 (5)	0.1930	0.1423	-2.504 (2)	0.4815	-1.577	64.930
6000	3.531 (5)	0.2118	0.1709	-1.493 (3)	0.4827	-2.053	65.589
6500	3.434 (5)	0.2290	0.1994	-2.774 (3)	0.4836	-2.545	66.184
7000	3.366 (5)	0.2444	0.2286	-4.087 (3)	0.4846	-3.050	66.723
7500	3.320 (5)	0.2583	0.2579	-5.430 (3)	0.4852	-3.565	67.217
8000	3.288 (5)	0.2711	0.2872	-6.790 (3)	0.4859	-4.092	67.670
8500	3.268 (5)	0.2826	0.3166	-8.175 (3)	0.4865	-4.625	68.090
9000	3.257 (5)	0.2934	0.3457	-9.575 (3)	0.4868	-5.166	68.479
9500	3.253 (5)	0.3031	0.3745	-1.099 (4)	0.4873	-5.713	68.841
10000	3.253 (5)	0.3122	0.4034	-1.242 (4)	0.4878	-6.264	69.180

(a) $Q_i = Q_i(B) + Q_i(M) + Q_i(F)$, $Q_i(B) = Q_i / (1 + Q_i(M)/Q_i(B) + Q_i(F)/Q_i(B))$

(b) units cal. mole⁻¹ deg.⁻¹. Evaluated using $H_{298} = -21.480$ kcal. and assuming $Q_{\text{tot}} = Q_1 + 3Q_3$

TABLE II. Partition Functions for $\text{Na}_2(X^1\Sigma_g^+)$ and $\text{Na}_2(b^3\Sigma_u^+)$

$T(^{\circ}\text{K})$	$Q_1^{(a)}$	$\frac{Q_1(M)}{Q_1(B)}$	$\frac{Q_1(F)}{Q_1(B)}$	$Q_3^{(a)}$	$\frac{Q_3(M)}{Q_3(B)}$	$\frac{Q_3(F)}{Q_3(B)}$	$-(G^{\circ}-H_{298}^{\circ})^{(b)}$ T
500	1.074 (11)	0.0000	-0.0000	2.615 (4)	0.4697	+0.4720	56.145
1000	7.395 (7)	0.0021	+0.0001	2.138 (4)	0.5289	+0.1883	59.787
1500	9.715 (6)	0.0209	0.0025	1.257 (4)	0.5492	-0.5142	62.663
2000	4.239 (6)	0.0573	0.0118	1.316 (3)	0.5602	-1.450	64.882
2500	2.822 (6)	0.0994	0.0288	-1.155 (4)	0.5666	-2.537	66.622
3000	2.256 (6)	0.1400	0.0520	-2.556 (4)	0.5711	-3.729	68.017
3500	1.976 (6)	0.1766	0.0793	-4.039 (4)	0.5739	-4.994	69.161
4000	1.820 (6)	0.2089	0.1100	-5.585 (4)	0.5762	-6.318	70.119
4500	1.727 (6)	0.2372	0.1423	-7.180 (4)	0.5783	-7.689	70.934
5000	1.670 (6)	0.2619	0.1757	-8.810 (4)	0.5797	-9.092	71.639
5500	1.634 (6)	0.2836	0.2096	-1.048 (5)	0.5809	-10.52	72.253
6000	1.612 (6)	0.3027	0.2436	-1.216 (5)	0.5818	-11.97	72.796
6500	1.600 (6)	0.3198	0.2776	-1.386 (5)	0.5830	-13.44	73.278
7000	1.594 (6)	0.3350	0.3114	-1.558 (5)	0.5835	-14.92	73.709
7500	1.592 (6)	0.3485	0.3448	-1.731 (5)	0.5842	-16.41	74.096
8000	1.595 (6)	0.3608	0.3776	-1.904 (5)	0.5847	-17.91	74.444
8500	1.600 (6)	0.3718	0.4099	-2.078 (5)	0.5853	-19.41	74.759
9000	1.607 (6)	0.3818	0.4418	-2.253 (5)	0.5859	-20.91	75.044
9500	1.615 (6)	0.3912	0.4731	-2.428 (5)	0.5863	-22.42	75.302
10000	1.624 (6)	0.3994	0.5035	-2.602 (5)	0.5865	-23.93	75.534

(a) $Q_i = Q_i(B) + Q_i(M) + Q_i(F)$; $Q_i(B) = Q_i / (1 + Q_i(M)/Q_i(B) + Q_i(F)/Q_i(B))$.

(b) units cal. mole⁻¹ deg.⁻¹. Evaluated using $H_{298}^{\circ} = -14.666$ Kcal. and assuming $Q_{\text{tot}} = Q_1 + 3Q_3$

TABLE III. Equilibrium Constant, Enthalpy and Gibbs Energy of Formation for Li_2 and Na_2

T	$2 \text{Li}(\text{ideal gas}) \rightarrow \text{Li}_2$			$2 \text{Na}(\text{ideal gas}) \rightarrow \text{Na}_2$		
	K_{eq}	$-\Delta H_f^\circ$	ΔG_f°	K_{eq}	$-\Delta H_f^\circ$	ΔG_f°
$^\circ\text{K}$	cm^3/mol	kcal/mol	kcal/mol	cm^3/mol	kcal/mol	kcal/mol
500	1.073 (11)	24.615	-14.682	1.975 (8)	17.791	-8.425
600	2.060 (9)	24.694	-12.688	1.192 (7)	17.862	-6.545
700	1.242 (8)	24.768	-10.681	1.630 (6)	17.925	-4.653
800	1.528 (7)	24.836	-8.664	3.711 (5)	17.977	-2.754
900	3.023 (6)	24.898	-6.384	1.187 (5)	18.019	-0.848
1000	8.335 (5)	24.952	-4.607	4.810 (4)	18.051	+1.061
1100	2.925 (5)	24.998	-2.570	2.316 (4)	18.079	2.974
1200	1.229 (5)	25.033	-0.529	1.267 (4)	18.106	4.889
1300	5.937 (4)	25.060	+1.514	7.652 (3)	18.140	6.807
1400	3.197 (4)	25.078	3.559	4.987 (3)	18.186	8.727
1500	1.878 (4)	25.089	5.605	3.454 (3)	18.247	10.652
1600	1.184 (4)	25.096	7.651	2.511 (3)	18.329	12.581
1700	7.904 (3)	25.109	9.698	1.899 (3)	18.434	14.516
1800	5.538 (3)	25.112	11.746	1.483 (3)	18.562	16.458
1900	4.039 (3)	25.126	13.796	1.190 (3)	18.715	18.407
2000	3.048 (3)	25.148	15.842	9.767 (2)	18.893	20.366
2100	2.367 (3)	25.180	17.789	8.168 (2)	19.095	22.333
2200	1.885 (3)	25.225	19.945	6.942 (2)	19.319	24.311
2300	1.533 (3)	25.285	21.999	5.982 (2)	19.566	26.300
2400	1.270 (3)	25.359	24.057	5.220 (2)	19.834	28.300
2500	1.069 (3)	25.450	26.117	4.595 (2)	20.122	30.311
2600	9.125 (2)	25.557	28.182	4.085 (2)	20.429	32.335
2700	7.886 (2)	25.680	30.251	3.660 (2)	20.753	34.370
2800	6.890 (2)	25.820	32.325	3.302 (2)	21.093	36.418
2900	6.078 (2)	25.976	34.405	2.998 (2)	21.449	38.478
3000	5.408 (2)	26.148	36.490	2.736 (2)	21.821	40.551
3500	3.326 (2)	27.254	47.024	1.841 (2)	23.911	51.136
4000	2.302 (2)	28.646	57.727	1.343 (2)	26.234	62.013
4500	1.717 (2)	30.275	68.619	1.029 (2)	28.777	73.194
5000	1.347 (2)	32.088	79.703	8.171 (1)	31.514	84.669
5500	1.095 (2)	34.044	90.976	6.651 (1)	34.432	96.427
6000	9.147 (1)	36.115	102.43	5.517 (1)	37.526	108.46

Figure Captions

- Fig. 1. Potentials for various Li_2 and Na_2 electronic states calculated by Konowalow et al.¹⁵
- Fig. 2. Representative electronic-rotational potentials, $v_{i,l}(R)$, for the $X^1\Sigma_g^+$ state of Li_2 .
- Fig. 3. Schematic comparison of a typical electronic-rotational potential $v_{i,l}(R)$ and a pure centrifugal potential $\gamma_l(R) = \hbar^2 l(l+1)/m_A R^2$ associated with noninteracting, i.e., ideal, atoms. The phase-shift $\eta_{i,l}(\epsilon)$ for a pair of incident atoms with relative kinetic energy ϵ measures the departure from ideal gas scattering. A positive $\eta_{i,l}$ is associated with an increase in the number of nodes in the scattering wavefunction whenever $v_{i,l}$ is more attractive than γ_l . At energies above the crossing of these two curves we expect a negative phase-shift due to the exclusion of the interacting atoms from the phase space available to the ideal atoms.
- Fig. 4. The calculated bound, $\epsilon_{1,100,v} < 0$, and metastable, $\epsilon_{1,100,\bar{m}} > 0$, states are located in a plot of $v_{1,100}(R)$ for the $l=100$ state of $\text{Li}_2(X^1\Sigma_g^+)$. The vibrational levels $v=0,10$ define the true bound state portion $q_{1,100}(B)$ of the radial partition function $q_{1,100} = q_{1,100}(B) + q_{1,100}(C)$. The total continuum contribution $q_{1,00}(C) = q_{1,100}(M) + q_{1,00}(F)$ is

divided into two components. The finite set of virtual levels $m=1,7$ predicted to exist behind the rotational barrier $R < R_{\text{Bar}}$, and with approximate eigenvalues $0 < \epsilon_{1,100,m} < \epsilon_{\text{bar}}$, define the metastable contribution $q_{1,100}^{(M)}$. The remainder of the phase-space associated with regions to the right, and above the rotational barrier is assigned to the free-continuum component $q_{1,100}^{(F)}$.

Fig. 5. Elastic scattering phase-shift $\eta_{1,130}(\epsilon)$ in the vicinity of the predicted resonance at $\epsilon_{1,130,m} = 1949.50 \text{ cm}^{-1}$ for the $\ell=130$ rotational state of $\text{Li}_2(X^1\Sigma_g^+)$. This is the 8th resonance, $m=8$, which lies about 53 cm^{-1} below the rotational barrier for $v_{1,130}(R)$ in Fig. 2. The figure presents the exact quantum mechanical predictions for $\eta_{1,130}$. An analytic fit to $\eta = (\text{background}) - \tan^{-1} [\frac{1}{2} \Gamma_m / (\epsilon - \epsilon_m)]$ perfectly reproduces the numerical results. The extracted width $\Gamma_{1,130,8} = 0.0051 \text{ cm}^{-1}$ predicts a predissociation lifetime $\tau_{1,130,8} = 10^{-9}$ sec. for this particular metastable state.

Fig. 6. Elastic scattering phase shift $\eta_{1,130}(\epsilon)$ in the vicinity of the the top-most resonance, $m=9$, for $\ell=130$ rotational state of $\text{Li}_2(X^1\Sigma_g^+)$. Such resonances which lie close to the rotational barrier (2057 cm^{-1}) are often broad, e.g., $\Gamma \approx 3 \text{ cm}^{-1}$ and $\tau \approx 10^{12}$ sec., and are not well fitted to the simple expression used in Fig. 5. However the width is still small compared to kT and the integrated contribution to the

partition function is well represented by the WKB phase shift.

Fig. 7. Plot of $\ell=0$ phase shift for $\text{Li}_2(X^1\Sigma_g^+)$. Levinson's theorem requires a threshold value $\eta_{1,0}/\pi = 42$. The rapid fall-off, i.e., $\partial\eta/\partial\epsilon \ll 0$, will yield a large negative contribution to the molecular partition function. This curve was calculated using the WKB theory and is indistinguishable from the exact quantal results (Shown at several points) except at energies within a few cm^{-1} of threshold. Such discrepancies will have a negligible effect on high temperatures equilibrium properties.

Fig. 8. Using the classical theory, we show the contributions to q_1 , $= q_{1,\ell}(\text{B}) + q_{1,\ell}(\text{M}) + q_{1,\ell}(\text{F})$ for $\text{Li}_2(X^1\Sigma_g^+)$ at 6000°K . These components must be weighted by the rotational degeneracy $(2\ell+1)$ to obtain the total internal partition function $Q_1 = \sum_{\ell} (2\ell+1) q_{1,\ell}$.

———— total, - - - - (B), — — — (M), — — — (F).

Both the metastable (M) and bound (B) components are always positive. However, the free-continuum (F) phase space often produces a negative contribution, especially for high temperatures and for shallow potentials. Only alternate values contribute to Q_1 when the dimer is homonuclear.

Fig. 9. Contributions to $q_{3,\ell}$ for $\text{Li}_2(b^3\Sigma_u^+)$ at 6000°K . See Fig. 8 for explanation.

Fig. 10. Phase shift $\eta_{1,100}/\pi$ for $\ell=100$ state of $\text{Li}_2(X^1\Sigma_g^+)$. Quantum theory requires a threshold value $\eta_{1,100}/\pi = 11$ due to the 11 true bound states shown in Fig. 4. The rapid rise to $\eta_{1,100}/\pi$ 18 at $\epsilon=1000 \text{ cm}^{-1}$ is a result of the 7 metastable states predicted in Fig. 4. The exact quantum results (dotted) show almost step-like increases in $\eta_{1,100}$ by modular- π at each resonance energy. The WKB phase shift (solid curve) passes smoothly through this region and joins exactly with the quantum phase shift above the rotational barrier.

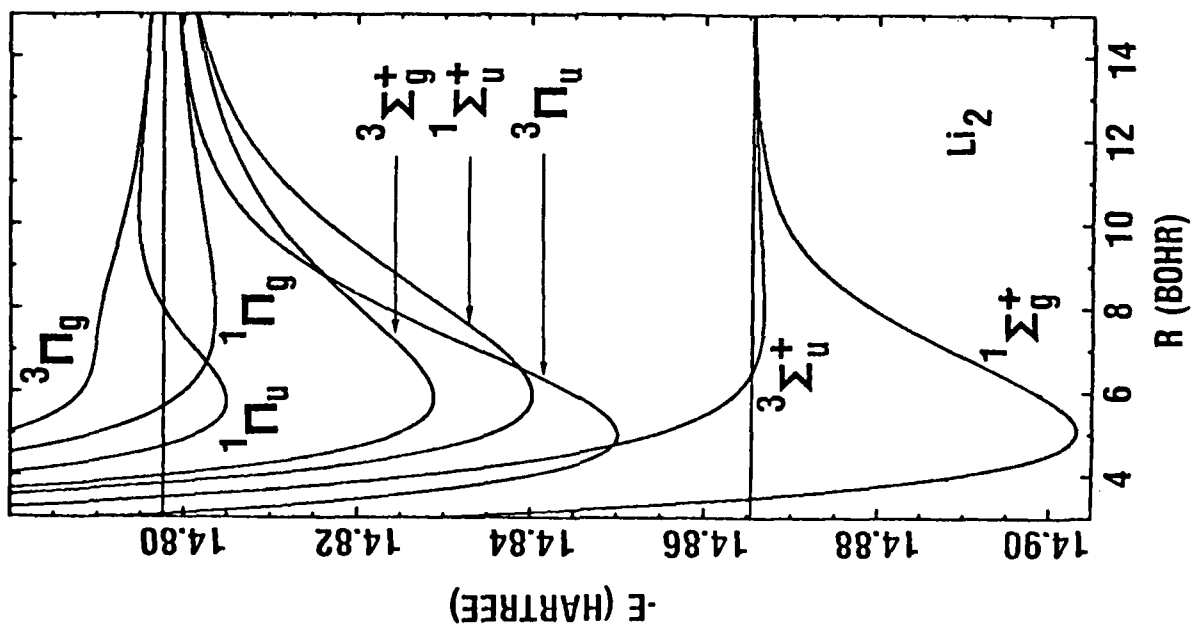
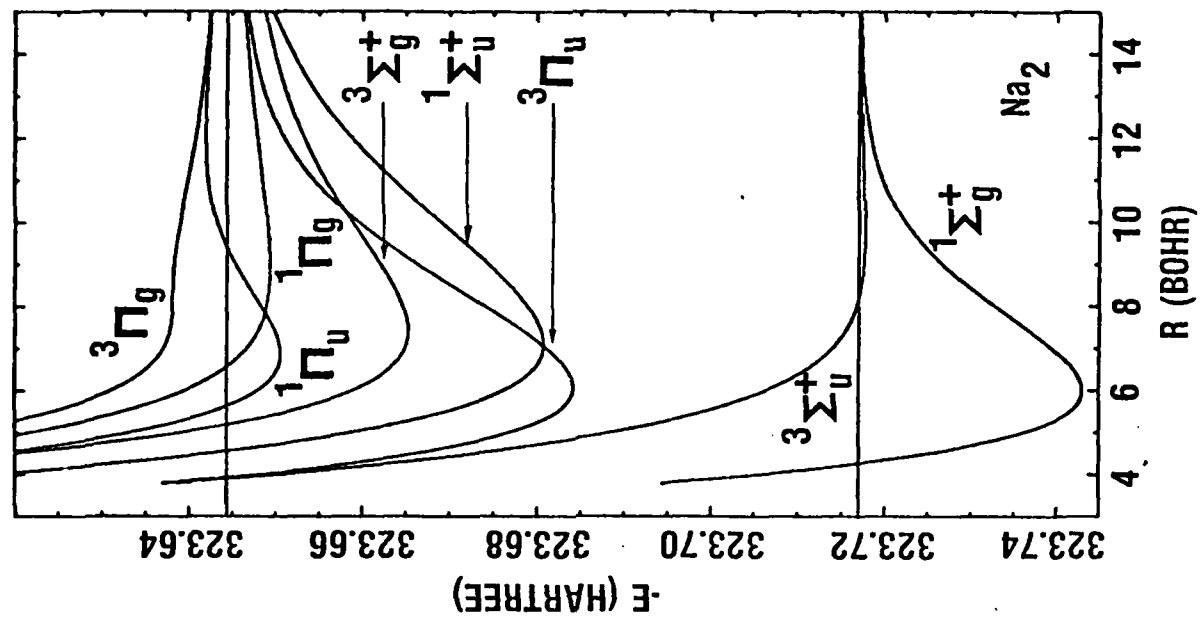
Fig. 11. Phase-shift $\eta_{1,130}/\pi$ for $\ell=130$ state for $\text{Li}_2(X^1\Sigma_g^+)$. Fig. 2 shows that $v_{1,130}(R)$ does not support any true bound states, and the threshold value must be $\eta_{1,130} = 0$. A rapid positive increase occurs between 600 cm^{-1} and 2000 cm^{-1} where the potential supports the 9 metastable states located by the step-like structure in the exact quantum phase shift (dotted).

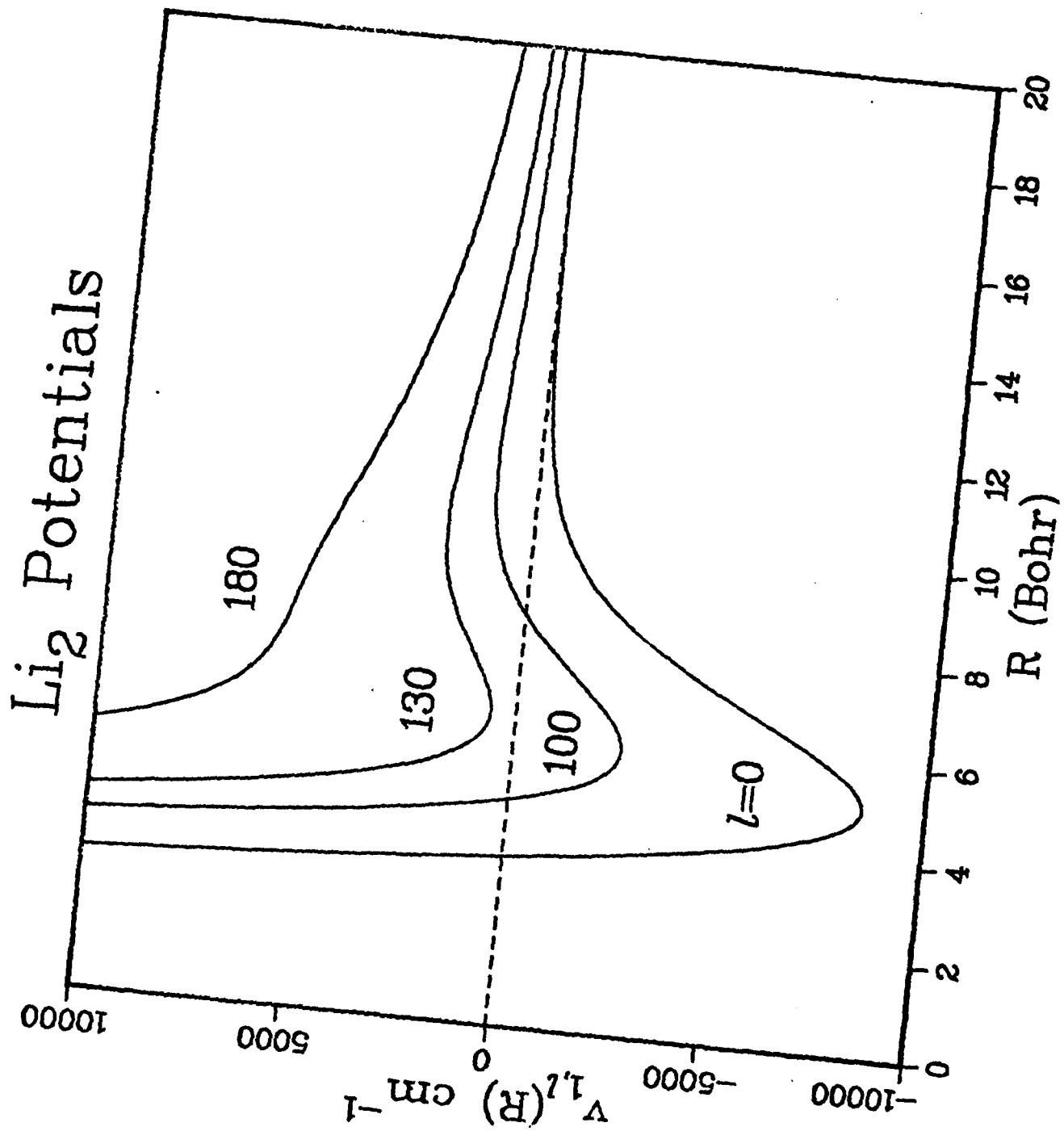
Fig. 12. Phase shift $\eta_{1,180}/\pi$ for $\ell=180$ state of $\text{Li}_2(X^1\Sigma_g^+)$. The potential $v_{1,180}(R)$ in Fig. 2 indicates that neither bound, nor metastable states exist, and $\eta_{1,180}(0) = 0$. Between threshold and $\epsilon=7000 \text{ cm}^{-1}$ there is a positive gradient, $\partial\eta/\partial\epsilon > 0$, and the resultant partition function $q_{1,180} \equiv q_{1,180}(F)$ will be positive for temperatures up to $10,000^\circ\text{K}$ and higher. Eventually the negative gradient portions of $\eta_{1,180}$ will tend to diminish $q_{1,180}$ until, for

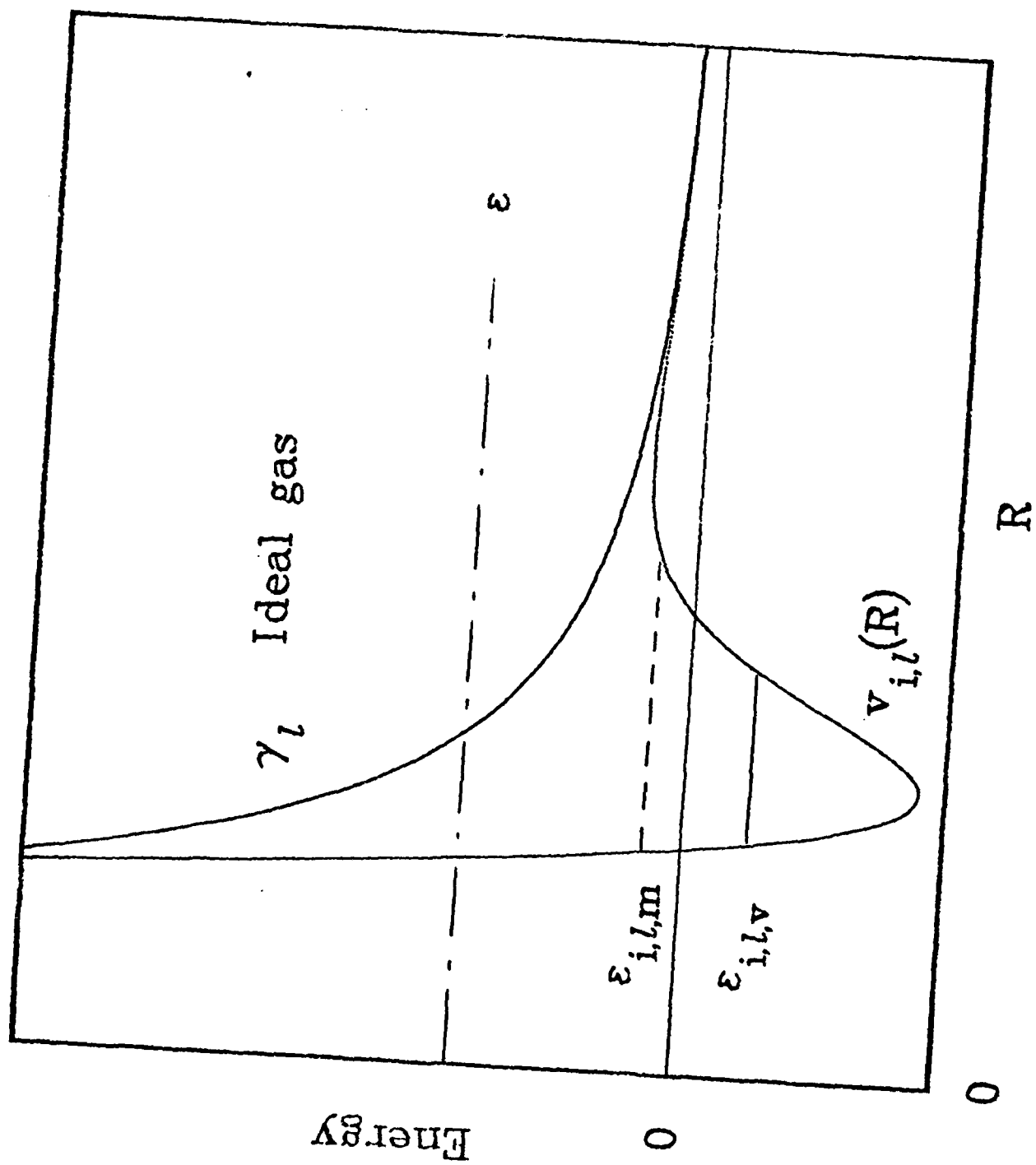
definite temperature, there is a perfect cancellation, since $\int_0^\infty d\epsilon \partial \eta / \partial \eta = 0$ as required by Levinson's theorem.

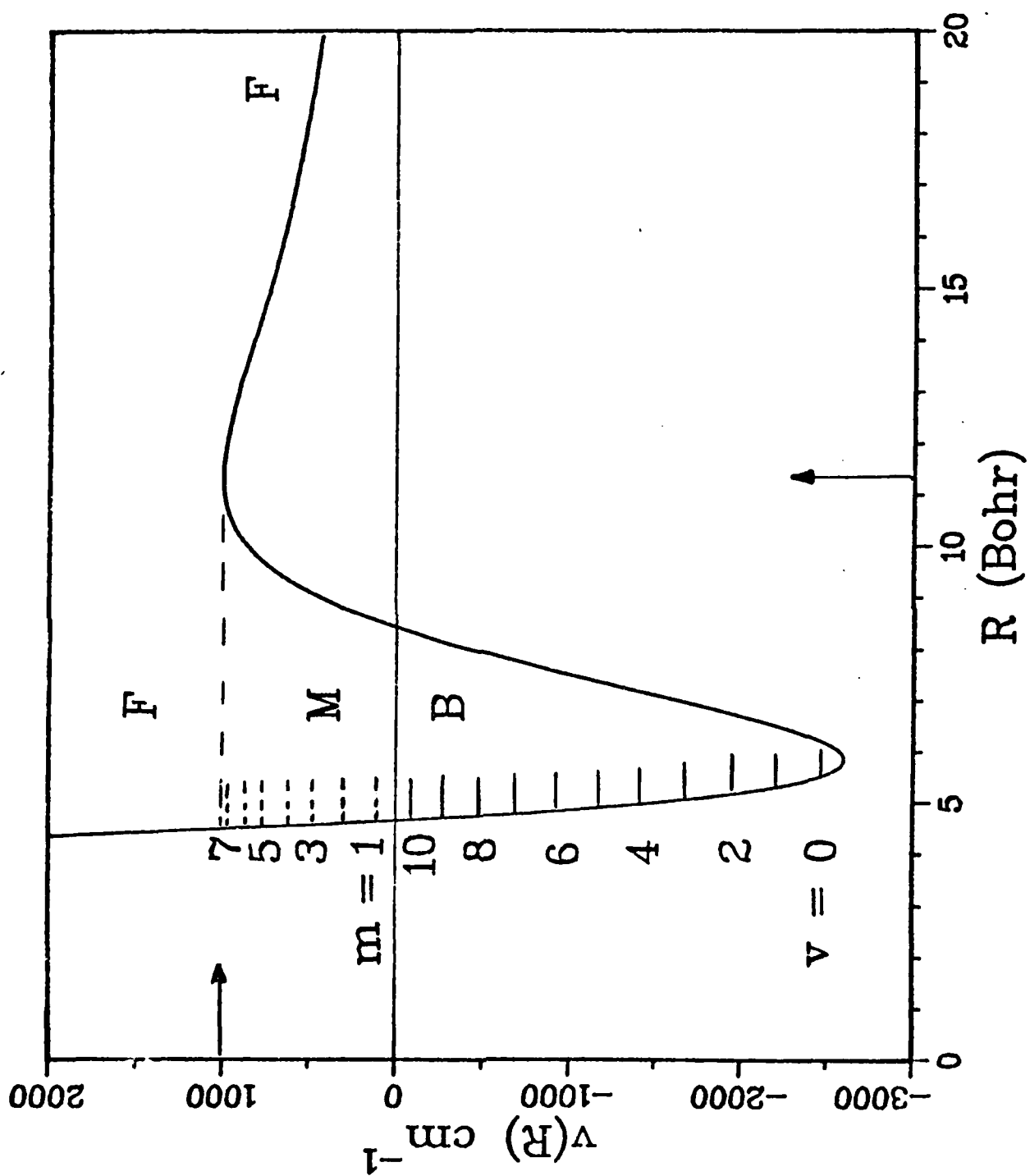
Fig. 13. Calculated equilibrium constant $K_{eg} = -\langle B \rangle$ for Li_2 and Na_2 . The solid curve is the result using the complete partition functions for both the singlet and triplet states. The dashed curve shows the effect of neglecting the $b^3\Sigma_u^+$ state. This deviation will be manifest as a residual second virial correction which must be applied to the alkali monomer if one hopes to reproduce the exact equation of state for the vapor.

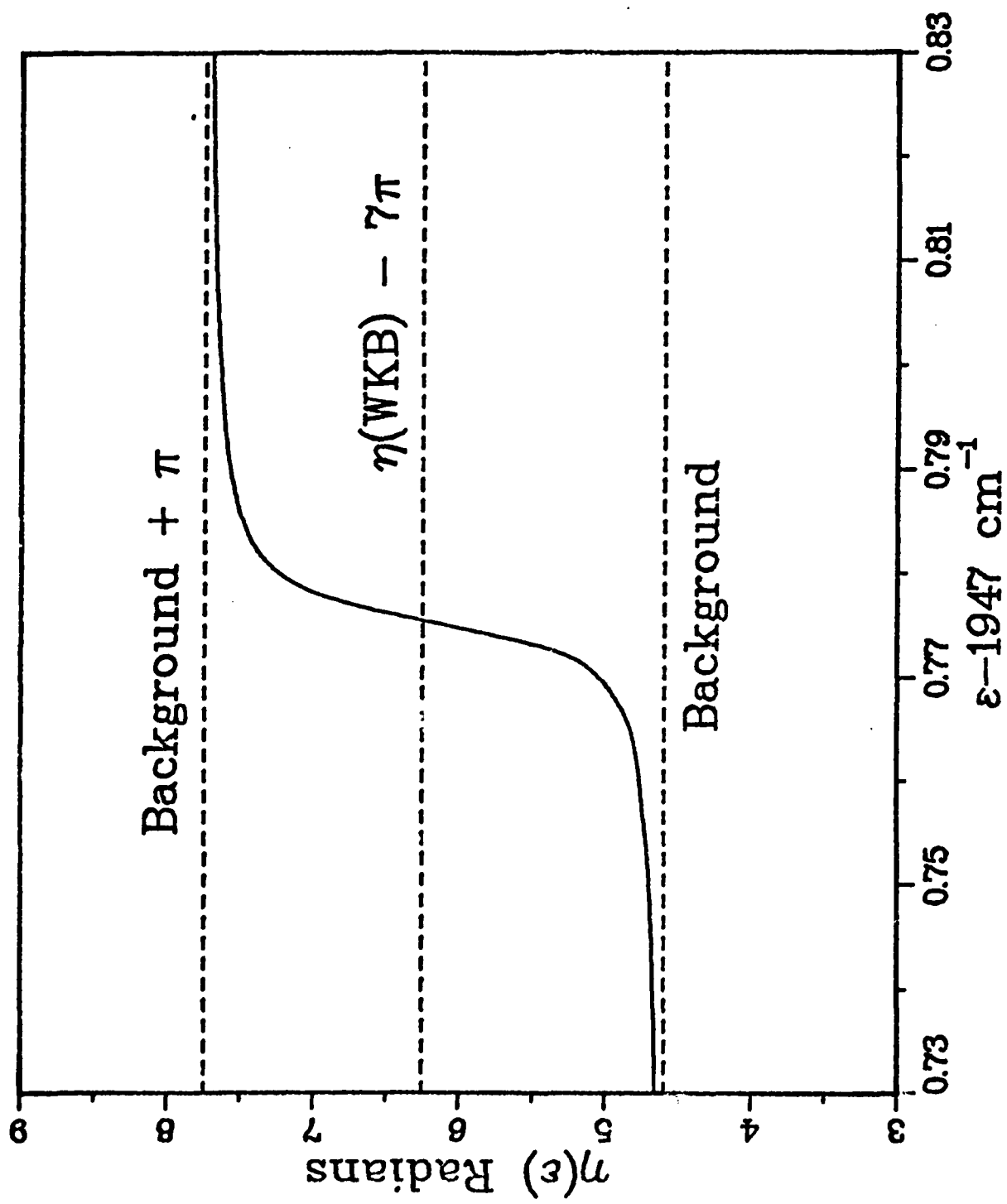
Fig. 14. Calculated equilibrium constant $K_p(^3\Sigma_u^+)$ for the triplet state of Li_2 . The solid curve is obtained by assuming $Q_{TOT} = Q_3$ and is meant to mimic the qualitative behavior we would expect for a shallow van-der-waals type dimer. The bound state contribution $K_p(B)$, shown by the dashed curve, remains position for all T , but the combined quantity $K_p = K_p(B) + K_p(C)$ predicts a negative concentration of dimers for $T > 5500^\circ\text{K}$. This effect can be properly described in terms of modified activity for the monomer.



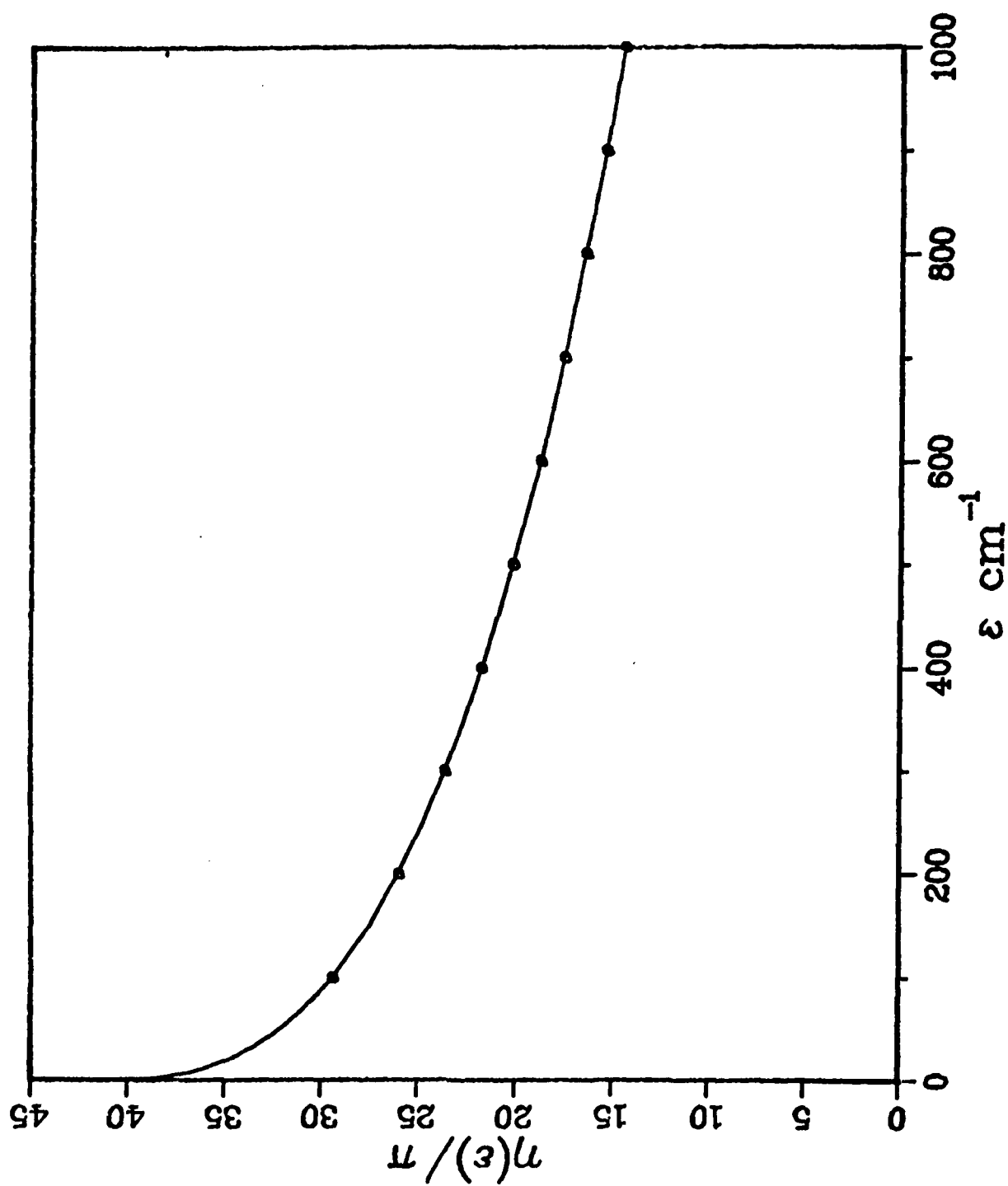


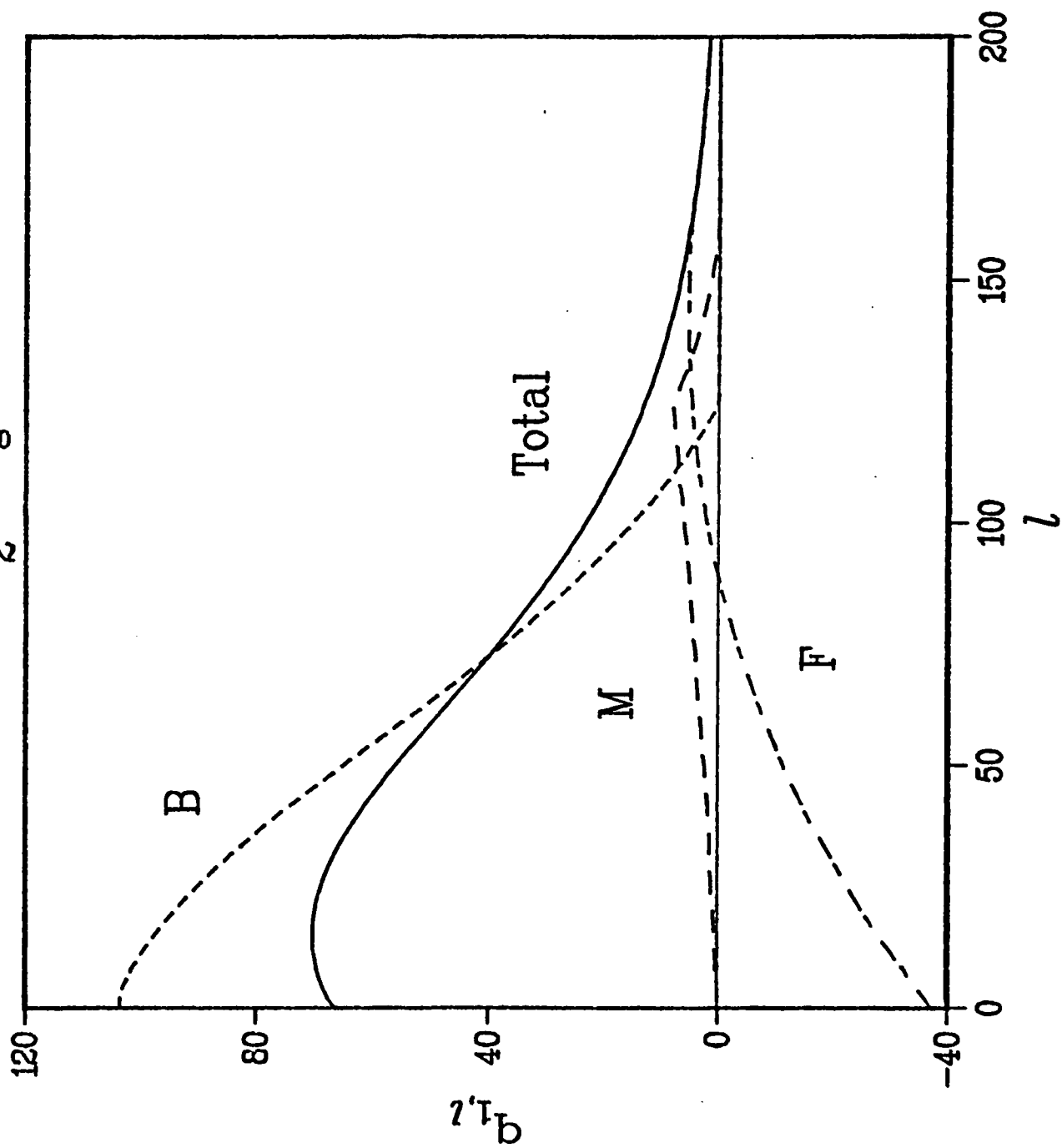
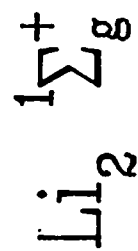


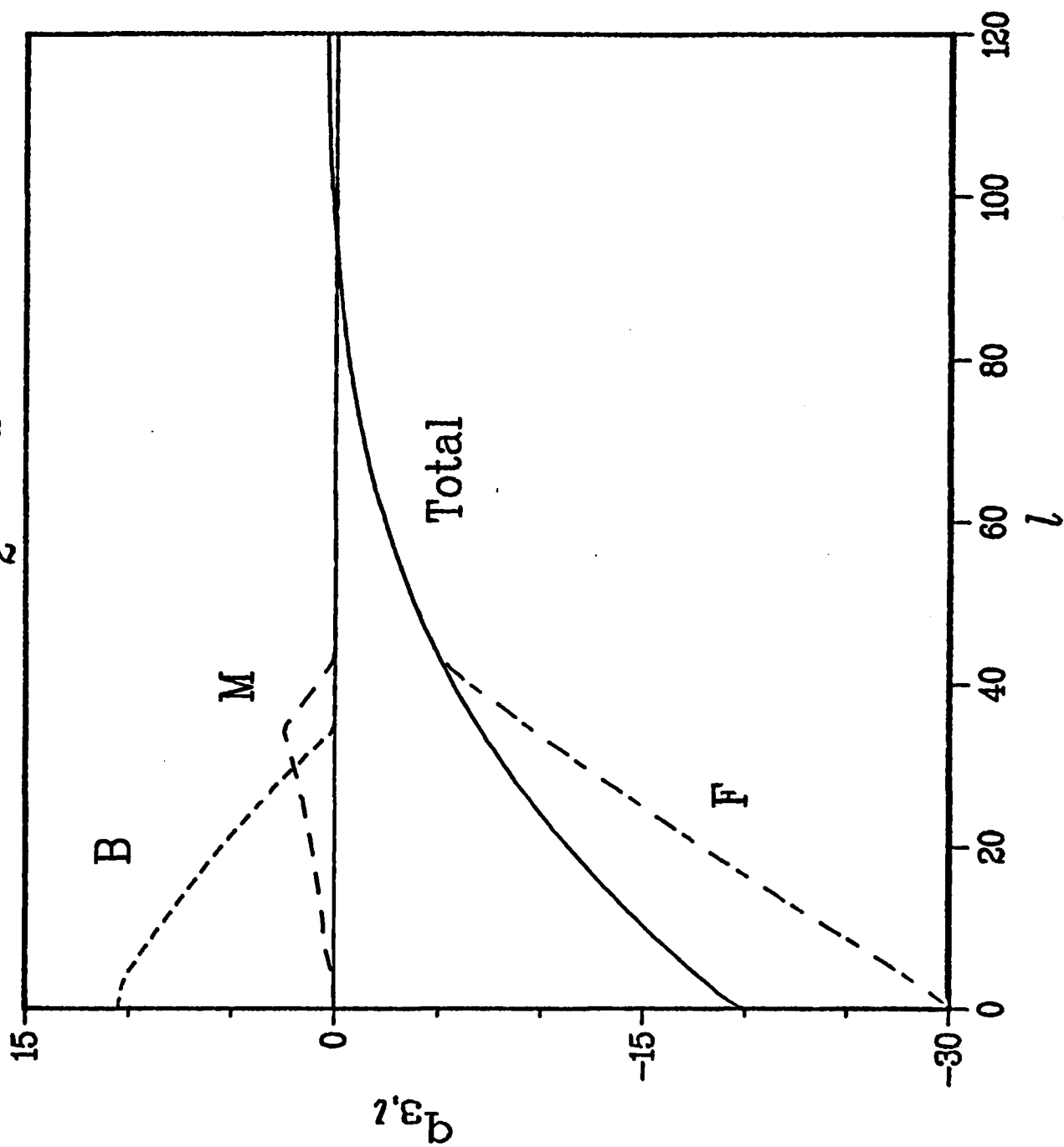
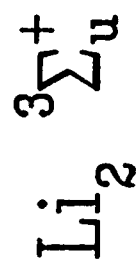




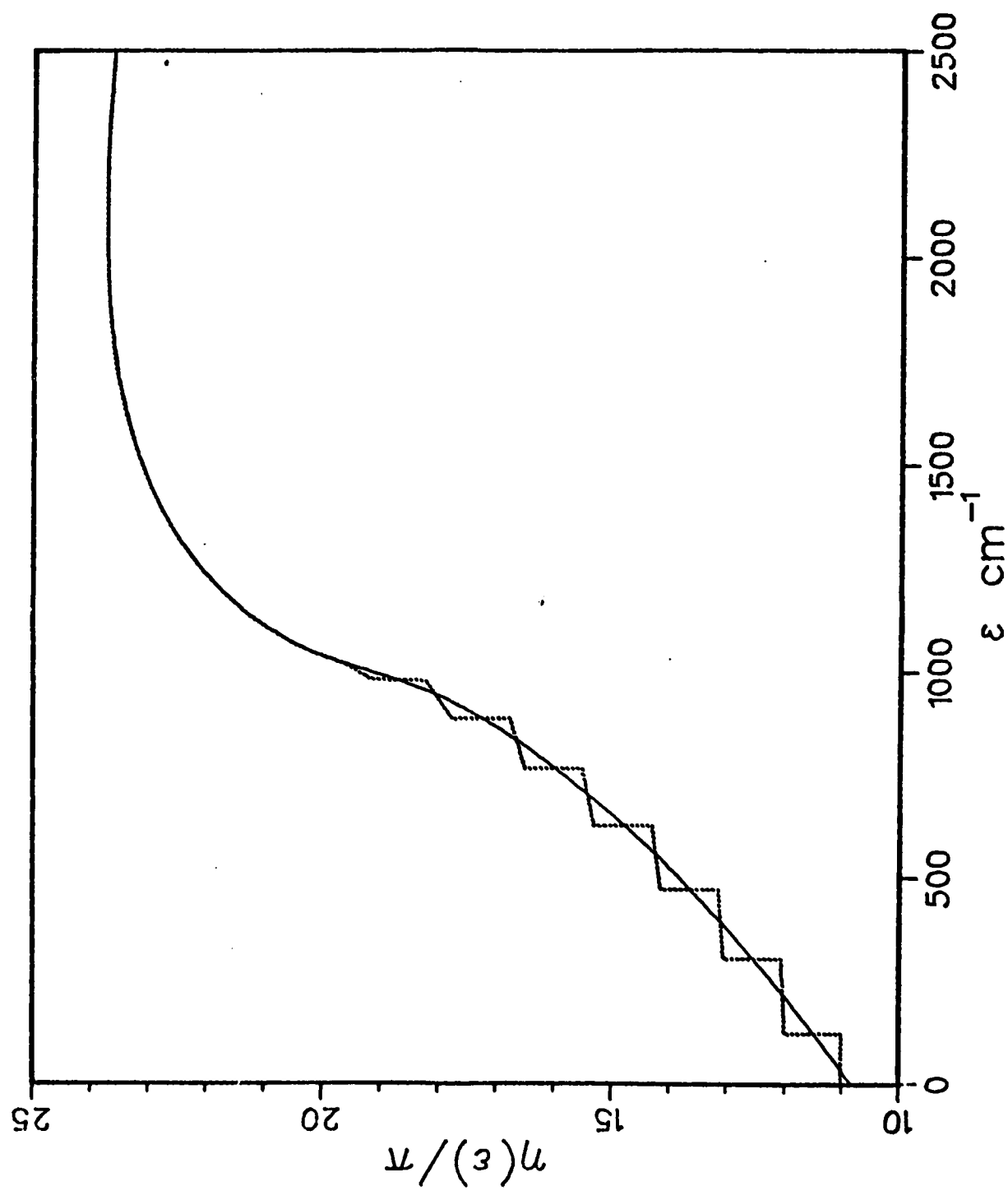
$l = 7$



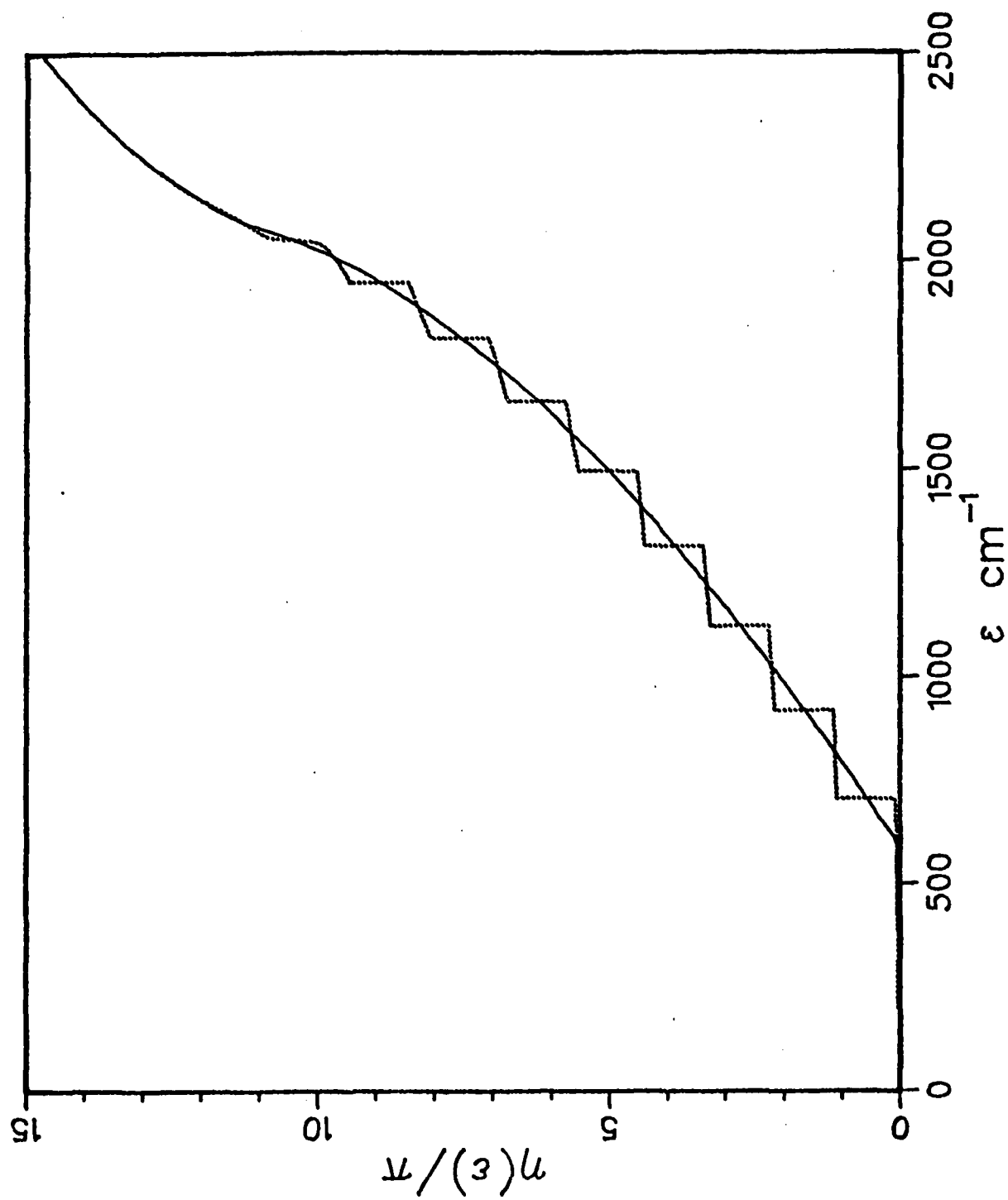




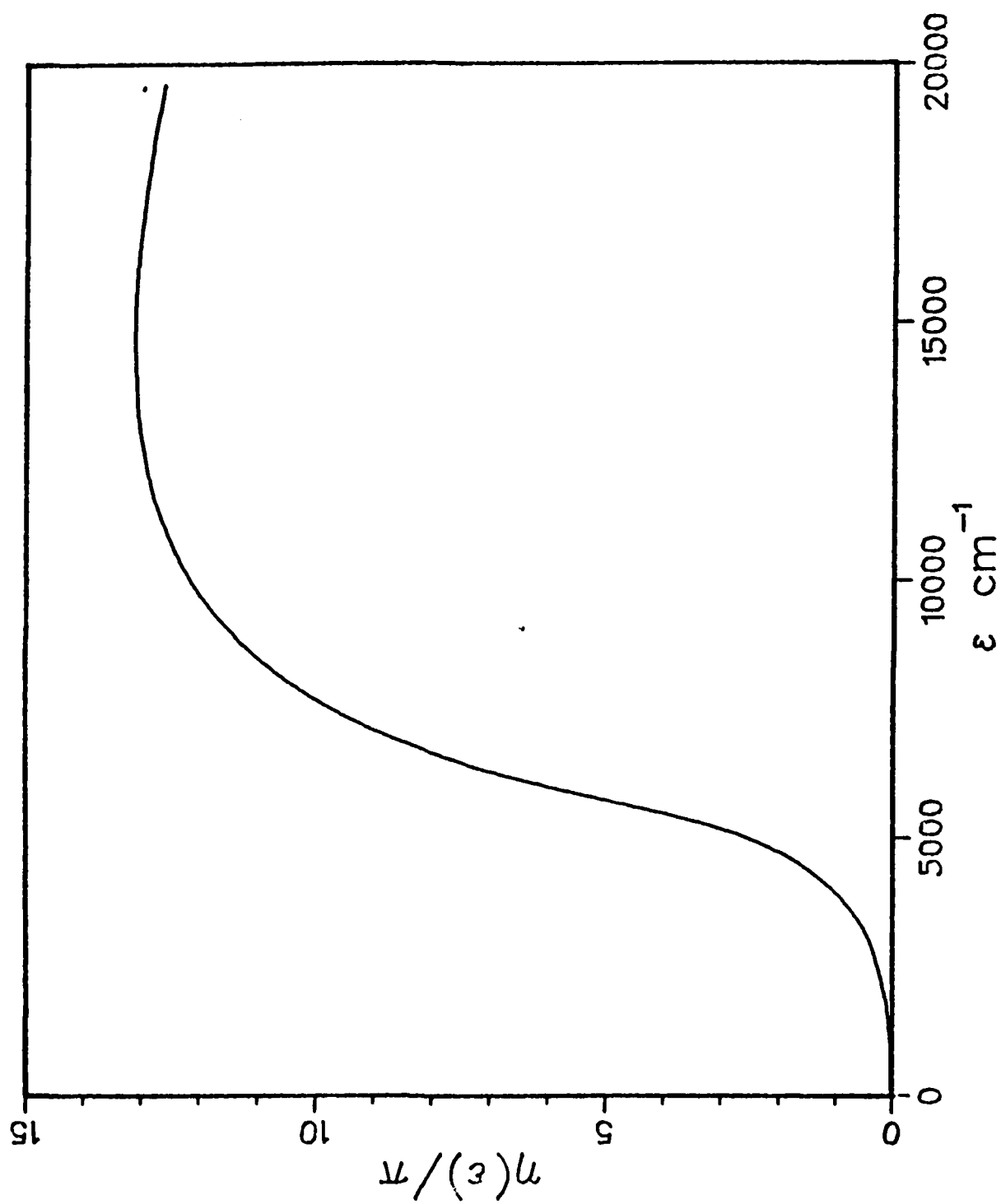
$l = 100$

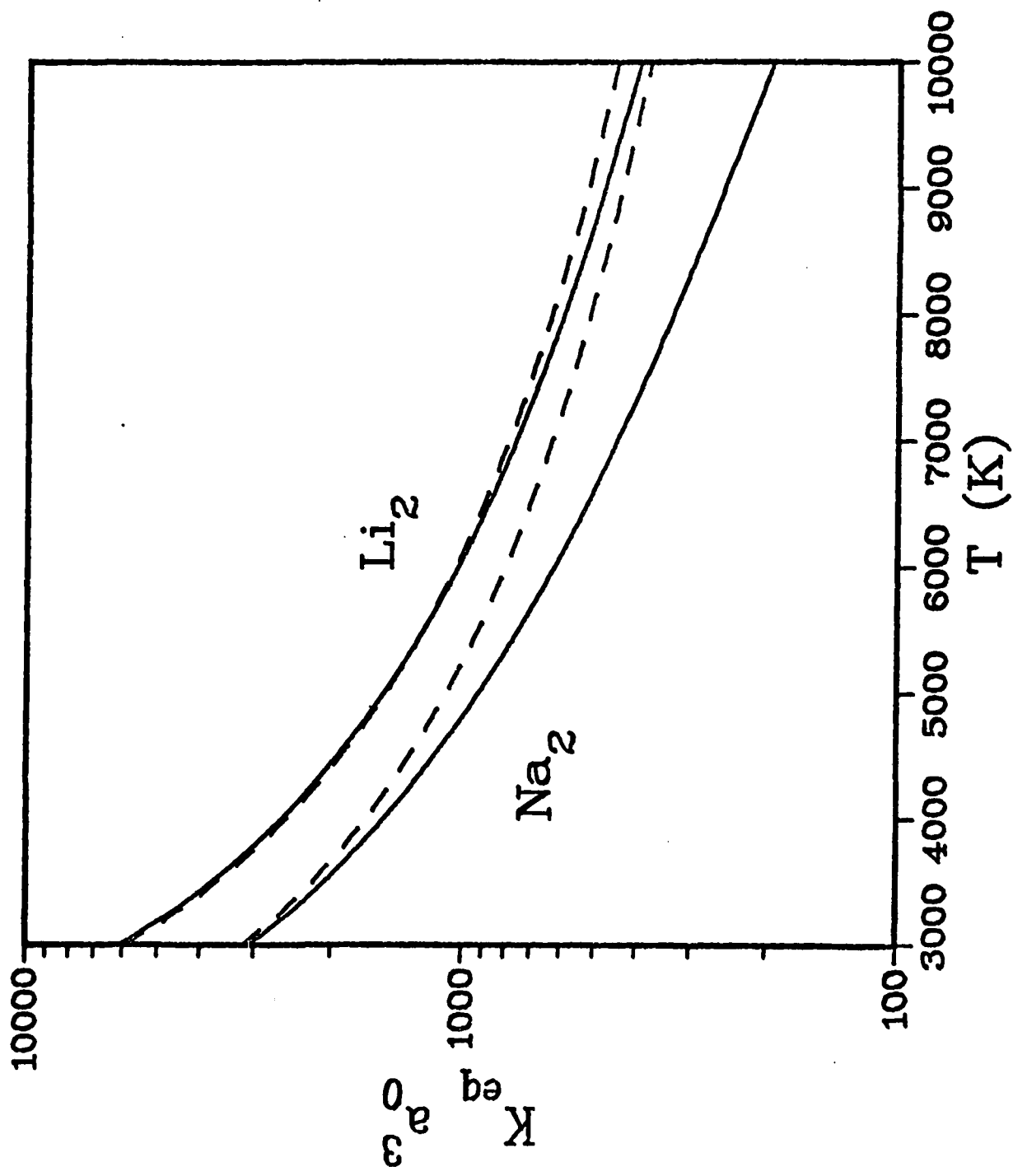


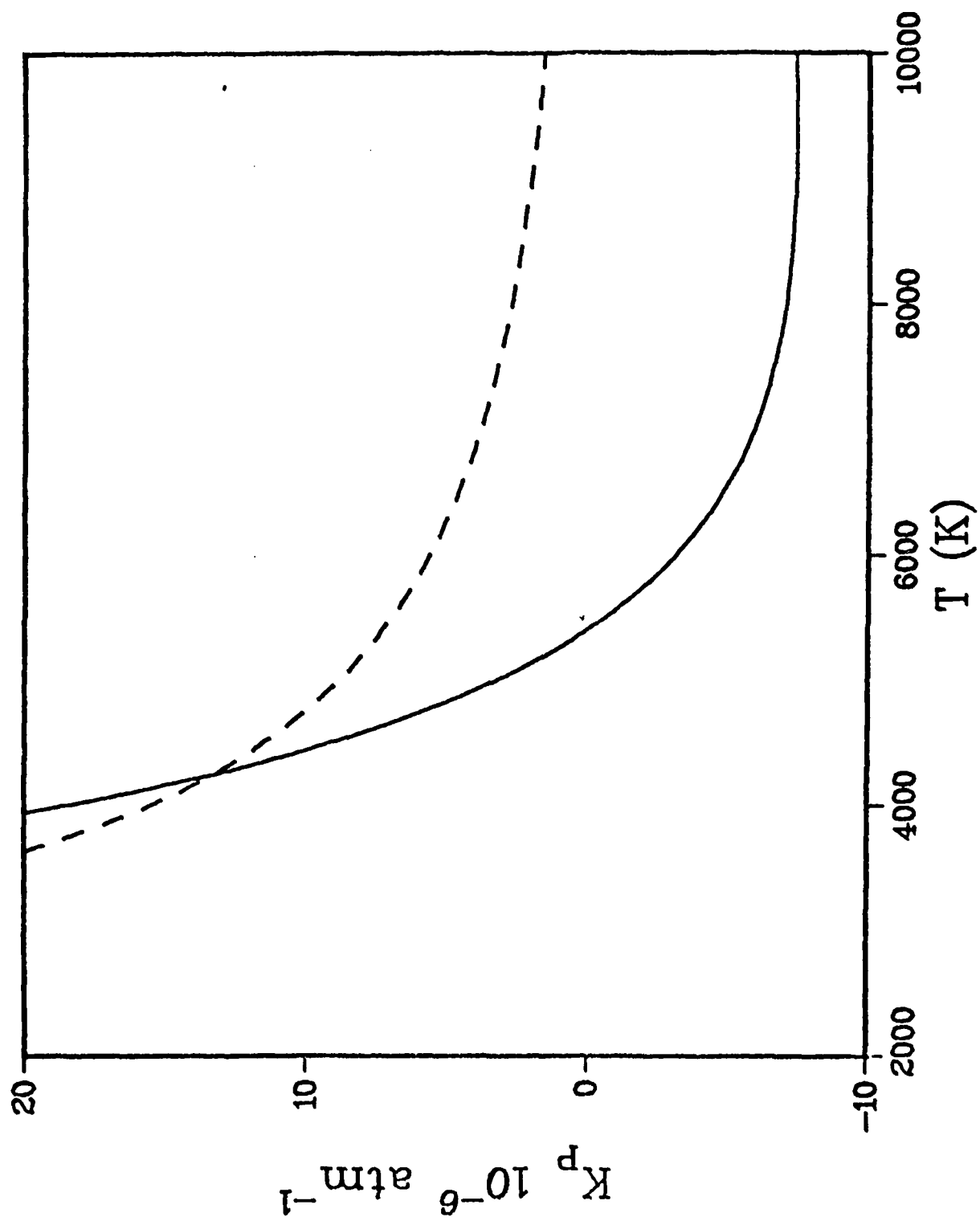
$$l = 130$$



$$l = 180$$







Barriers to Internal Rotation in Inorganic Species

Stanley Abramowitz

ABSTRACT

Barriers to internal rotation have been determined using infrared and Raman spectroscopy for some inorganic species. The determination of these barriers will be described for a high barrier (BCl_2SH) a medium barrier (PF_5 , AsF_5 and VF_5) and a low or zero energy barrier ($\text{B}(\text{CH}_3)_3$).

INTRODUCTION

The determination of the energy barriers to internal rotation and the vibrational energy levels associated with these barriers are very important for the computation of thermodynamic functions. This paper will illustrate the experimental determination of barriers to internal rotation for the species BCl_2SH (D), XF_5 where $\text{X} = \text{P}, \text{As}$ or V , and $\text{B}(\text{CH}_3)_3$. These represent a high, medium and low (zero) barrier respectively. The techniques of vibrational spectroscopy were utilized to determine the relevant vibrational energy levels. In the case of $\text{B}(\text{CH}_3)_3$ a comparison of the third law entropy with an experimentally determined entropy was made.

BCl_2SH

The BCl_2SH molecule and its deuterium analog have a planar C_s symmetry. This symmetry has $7a'$ and $2a''$ modes (1). (It should be noted that another C_s structure is possible with a σ_v plane bisecting the ClBCl angle. This structure has $6a'$ and $3a''$ vibrations.) The vibrational assignment for the BCl_2SH and BCl_2SD species is given in Table 1. (Where B and/or Cl isotope effects have been observed the frequency given is for the $^{11}\text{B}^{35}\text{Cl}_2\text{SH}$ (D) species.) This assignment was arrived at through interpretation of the infrared and Raman spectra and the boron, chlorine and hydrogen vibrational isotopic shifts. The vibrational assignment for BCl_2SH and BCl_2SD was used to calculate the force field for these species. The computed force field successfully predicts the isotopic splittings for these species (1). The off diagonal force constants were taken from BCl_3 (2). Other off-diagonal force constants were used only if they improved the overall frequency shift. The symmetry coordinates and force field and the assumed geometric structure for the BCl_2SH (D) species can be found in reference 1.

The SH (D) torsional mode shows a hot band structure in the infrared spectrum with 0-1, 1-2, 2-3, and 3-4 modes observed for both species. Spectra observed at temperatures higher than ambient verified the assignments.

These modes could be fit with either of two potentials

$$V = A(z^4 - Bz^2), \text{ where } z = 2\phi \text{ or,}$$

$$V = (V_2/2) (1 - \cos 2\phi)$$

This is because the barrier is quite high and the first potential is simply $(1 - \cos \phi)$ with a truncated power series substituted for $\cos \phi$.

The $A(z^4 - Bz^2)$ which is most useful for ring puckering modes does not require a knowledge of the molecular dimensions. This is an advantage for BCl_2SH (D) since experimentally determined bond lengths and angles are not available. The $V_2/2 (1 - \cos 2\phi)$ which requires a knowledge of the molecular dimensions is a better model for the molecular motion involved in the SH(D) torsional mode, ν_7 .

For this potential the moments of inertia are computed from the assumed molecular dimensions. Table 2 presents a summary of the calculated and observed vibrational frequencies for the torsional vibrational modes about the B-S bond. As one can see the barrier is quite high. The more physically meaningful potential, $V = (V_2/2) (1 - \cos 2\phi)$ yields a barrier of about 4200 cm^{-1} for these species.

XF_5 where X=P, As and V

All of these species have been shown to be trigonal bipyramids having D_{3h} structure. The F atom interchange in these species can be accomplished through the motions along the $\text{E}' \nu_7$ coordinate which can lead to axial equatorial interchange through a C_{4v} intermediate (3,4). It was therefore very interesting to have obtained the Raman gas phase spectra of these species in order to directly observe the hot band structure. This vibrational hot band structure must be interpreted using a doubly degenerate harmonic oscillator function (3,4).

The Hamiltonian for axial-equatorial interchange is given by

$$H = (a\hbar^2/m)^{1/2} H_D$$

where

$$H_D = [1/2 (P_x^2 + P_y^2)^2 + 1/2(x^2+y^2)-B(x^3-3xy^2)+C(x^2+y^2)^2]$$

where B and C contain a term which is a scale factor involving the reduced mass involved in the ν_7 vibration and the harmonic force constant describing the ν_7 vibration. One can produce a table of dimensionless eigenvalues for this potential (4), where the barrier for F atom interchange is $-(1/32)B^2$. The important feature of this potential is that it requires $(n + 1)$ vibrational levels where n is the vibrational quantum number.

The advantages of working with the above reduced Hamiltonian are (1) one need not calculate an explicit reduced mass and (2) there is one less potential constant to vary than in the explicit form. Thus a fit of the reduced Hamiltonian H_D to observed energy levels will yield B, C and the scale factor and the barrier to axial - equatorial interchange.

The observed and calculated ν_7 transitions for PF_5 , AsF_5 , and VF_5 are given in Tables 3, 4, and 5 respectively. The barriers decrease monotonically from about 1050 to 475 cm^{-1} . More features are observed in VF_5 than AsF_5 and more in AsF_5 than PF_5 because of the Boltzmann factor. The vibrational frequency decreases from 175 to 133 to 108 cm^{-1} in going from PF_5 to AsF_5 and VF_5 . Therefore, the largest number of vibrational levels are populated in VF_5 ; with less in AsF_5 and even less in PF_5 . Further features of the dynamics of axial - equatorial fluorine atom interchange can be found in the references cited (4).

$B(CH_3)_3$

The third law entropy of $B(CH_3)_3$ computed from the available vibrational assignment and inertial parameters assuming free rotation of the CH_3 groups is not in agreement with the experimentally measured entropy (6,7). (The

difference is such that any barrier to rotation would increase the discrepancy). Since the Raman gas phase spectrum for this species had not been previously observed a reinvestigation of the vibrational spectrum was initiated in order to better characterize the vibrational assignment. Boron trimethyl has a planar BC_3 skeleton. Conventional point group theory would indicate an average D_{3h} symmetry for freely rotating CH_3 groups with 20 normal modes. However, the observed infrared and Raman gas phase spectra showed fewer features. The observed spectra indicated that the G_{324} symmetry group based upon the molecular symmetry (MS) group theory first proposed by Longuet-Higgins (8,9) was necessary. Since the discussion of the vibrational structure in terms of the G_{324} group and its relationship to D_{3h} has not been previously given a brief discussion of the vibrational analysis follows. Finally a program developed to compute the thermodynamic functions for anharmonic oscillators was utilized. Somewhat better agreement between the computed third law entropy and that experimentally determined is obtained.

The vibrational modes of $B(CH_3)_3$ are shown in Table 6. For a D_{3h} symmetry with freely rotating methyl groups one expects 20 normal modes. The A_1' , E' and species are Raman active while the A_2'' and E'' species are infrared active. If one considers the G_{324} molecular symmetry group there are 15 normal modes of which the A_1 , I , G and E_2 are Raman active while the A_3 , I , G and E_2 are infrared active. Table 5 shows a correlation diagram between D_{3h} and G_{324} symmetries. It should be noted that G_{324} requires 8 Raman active modes and nine infrared active modes while D_{3h} symmetry requires 13 Raman active modes and 11 infrared active modes. The significant feature of the MS group is the relative simplicity of the

AD-A114 869

NATIONAL BUREAU OF STANDARDS WASHINGTON DC
THERMODYNAMICS OF HIGH TEMPERATURE MATERIALS.(U)
SEP 81 S ABRAMOWITZ, A CEZAIIRLIYAN, F MIES

F/G 20/13

AFOSR-ISSA-81-00012

UNCLASSIFIED

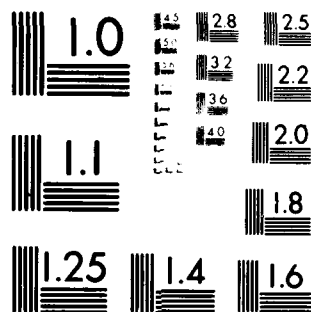
AFOSR-TR-82-0380

NL

2 2



END
DATE
FILMED
6 82
DTIC



MICROCOPY RESOLUTION TEST CHART
NATIONAL BUREAU OF STANDARDS 1963-A

expected vibrational spectrum. The observed infrared and Raman vibrational spectra confirm the M_3 symmetry group as the better representation of this molecule's symmetry. The BC_3 asymmetric stretching frequency ν_{15} for D_{3h} or ν_{14} for G_{324} symmetries respectively shows a ^{10}B - ^{11}B isotope shift of about 30 cm^{-1} . This shift is to be expected for a planar BC_3 skeleton. (The corresponding mode in the boron trihalides also show a similarly large isotope shift.) Three out of the four A_3 modes have the same P-R separation which is to be expected for these parallel transitions. As is to be expected these modes are not in the Raman spectrum. The three A_1 modes at 2916, 1291, and 678 cm^{-1} are all polarized and are absent in the infrared spectrum as required by the selection rules. The two 6 fold degenerate vibrations ν_{11} and ν_{12} have rather broad unstructured contours in both the infrared and Raman spectra. In summary the infrared and Raman spectra are consistent with a G_{324} molecular symmetry assignment. There are not enough vibrational bands observed to justify a D_{3h} assignment for the $B(CH_3)_3$ molecule. A summary of the vibrational assignment is given in Table 7.

A calculation of the third law entropy of $B(CH_3)_3$ can be made using the rigid rotor harmonic oscillator approximation and by assuming free rotation of the three methyl groups about the B-C bonds. The vibrational assignment given in Table 7 is used together with the bond distances and angles determined using electron diffraction techniques by Bartell and Carroll (10). An entropy of 67.83 cal/K at 199.92 K is computed assuming free rotation of the CH_3 groups. This compares with the measured value of $68.29 \pm 0.10\text{ cal/K}$ (1). The fact that the measured entropy is greater than that computed using spectroscopic data indicates essentially free rotation of the methyl groups. Any significant barrier to the rotation

of the methyl groups results in a lowering of the calculated entropy and therefore an increase in the discrepancy between the measured and computed entropy.

A computer program has been written to compute the effect of anharmonicity on the vibrational contribution to the entropy. In this computation all vibrational states were assumed to have a 1% anharmonicity (other values of the anharmonicity can be chosen for each vibration). This computer code obtains a state sum by counting those levels whose partition coefficient exceeds a chosen value, in this case 10^{-8} . (A choice of 10^{-11} does not effect the computed entropy.) An increase of 0.03 e.u. at 199.92K is obtained in this manner. The projected difference increases for higher temperatures.

This program will be especially useful in computing estimated errors in entropy caused by vibrational anharmonicity. It will therefore be useful for comparing third law (statistically calculated) entropies with those derived from thermodynamic measurements. By identifying expected differences the evaluation of thermodynamic data particularly for high temperature species should be expedited.

REFERENCES

1. Kirklin, D. R., Ritter, J. J., and Abramowitz, S., J. Mol. Spectroscopy, 67, 322 (1977).
2. Levin, I. W., and Abramowitz, S., J. Chem. 43, 4213 (1965).
3. Bernstein, L. S., Kim, J. J., Pitzer, K. S., Abramowitz, S., and Levin, I. W., J. Chem. Phys., 62, 3671 (1975).
4. Bernstein, L. S., Abramowitz, S., and Levin, I. W., Chem., Phys. 64, 3228 (1976).
5. Holmes, R. R. Sr., Deiters, R. M., and Hora, C. J., J. Chem. Soc. Commun. 175, 1974.
6. Furukawa, G. T. and Park, R. P. National Bureau of Standard Report 3644 (1954).
7. Woodward, L. A., Hall, T. R., Dixon, R. N., Shepard, N., Spectrochim., Acta 15, 249 (1959).
8. Longuet-Higgins, H. C., Molecular Phys. 6, 445 (1963).
9. Bunker, P. R., Molecular Symmetry and Molecular Structure, Academic Press, New York (1979).
10. Bartell, L. S., and Carroll, B. L., J. Chem. Phys. 42, 3076 (1965).

Table 1. Vibrational Assignment BCl_2SH and BCl_2SD

Vibrational Assignment	Approximate Description	BCl_2SH	BCl_2SD
ν_1	SH (D) str.	2602	1863
ν_2	BCl_2 asym. str.	994	999
ν_3	BS str.	900	900
A' ν_4	SH(D) bend	779	599
ν_5	BCl_2 sym str.	461.8	459
ν_6	ClBCl bend	255	255
ν_7	ClBS bend	230	227
A' ν_8	Cl o.o.p.	474	475
ν_9	SH(D) torsion*	386	283

* The 0-1 frequency is given.

Hot band transitions are given in Table 2.

Table 2. Observed vs. Calculated ν_9 Torsional Frequencies (cm^{-1})

$V = (V_2/2)(1 - \cos 2\phi)$					
$V = A(z^4 + Bz^2)$					
Transition	Obs'd	Calc'd.	Δ	Obs'd.	Calc'd.
$\text{BCl}_2\text{SH } F^2 = 9.581 \text{ cm}^{-1} \quad \bar{S} = 430.204 \quad V_2 = 4121.78 \text{ cm}^{-1} \quad (11.785 \text{ Kcal/mol})^1 \quad \bar{B} = -21.896 \quad V_2 = 3574.67 \text{ cm}^{-1} \quad (10.220 \text{ Kcal/mol})^1$					
$0 \rightarrow 1$	386.1	387.6	-1.5	386.1	386.1
$1 \rightarrow 2$	376.6	377.4	-0.8	376.6	377.1
$2 \rightarrow 3$	367.9	355.7	+1.1	367.9	367.4
$3 \rightarrow 4$	356.9	355.7	+1.2	356.9	356.9
$\text{BCl}_2\text{SD } F^2 = 4.790 \text{ cm}^{-1} \quad \bar{S} = 903.091 \quad V_2 = 4325.81 \text{ cm}^{-1} \quad (12.368 \text{ Kcal/mol})^1 \quad \bar{B} = -26.45 \quad V_2 = 3459.36 \text{ cm}^{-1} \quad (9.891 \text{ Kcal/mol})^1$					
$0 \rightarrow 1$	282.9	282.9	0.0	282.9	282.9
$1 \rightarrow 2$	277.8	277.9	-0.1	277.8	278.0
$2 \rightarrow 3$	272.9	272.8	+0.1	272.9	272.9
$3 \rightarrow 4$	267.5	267.5	0.0	267.5	267.5

¹ (Kcal/mol) = 4.184 kJ/mol

² Computed from assumed molecular dimensions (ref.1).

Table 3. Observed and Calculated ν_7 Transitions for PF_5

Transitions	Symmetry	Calculated (cm^{-1}) $B = 0.07$	Calculated (cm^{-1}) $B = 0.075$	Observed ^a (cm^{-1}) Raman
0 \rightarrow 1	$A_1' \rightarrow E'$	175.0	175.0	175
1 \rightarrow 2	$E_1' \rightarrow A_1'$	161.8	159.8	159
1 \rightarrow 2	$E' \rightarrow E''$	177.9	178.0	178
2 \rightarrow 3	$A_1' \rightarrow E'$	164.8	163.5	164
2 \rightarrow 3	$A_1' \rightarrow A_1'$	192.7	194.0	194
2 \rightarrow 3	$A_1' \rightarrow A_1'$	198.9	199.4	b
2 \rightarrow 3	$E' \rightarrow E'$	148.8	145.3	b
2 \rightarrow 3	$A_1' \rightarrow A_1'$	177.5	175.7	c
2 \rightarrow 3	$E' \rightarrow A_1'$	182.9	184.3	180
Barrier height (cm^{-1})	---	1139	995	---

^a The additional peaks at 168 cm^{-1} and 187 cm^{-1} probably correspond to OP and RS maximum, respectively.

^b Not observed.

^c This feature is probably obscured by 0 \rightarrow 1 transition.

Table 4. Observed and Calculated ν_7 Transitions for AsF_5 .

Transition	Symmetry	Calculated (cm^{-1}) B = 0.07	Calculated (cm^{-1}) B = 0.075	Observed (cm^{-1}) Raman
0 \rightarrow 1	$A_1' \rightarrow E'$	132.8	132.8	133
1 \rightarrow 2	$E' \rightarrow A_1'$	122.8	121.2	121
1 \rightarrow 2	$E' \rightarrow E'$	135.0	135.1	136
2 \rightarrow 3	$A_1' \rightarrow E'$	125.1	124.1	125
2 \rightarrow 3	$A_1' \rightarrow A_1'$	146.2	147.2	148
2 \rightarrow 3	$A_1' \rightarrow A_1'$	151.0	153.7	157
2 \rightarrow 3	$E' \rightarrow E'$	112.9	110.2	113
2 \rightarrow 3	$E' \rightarrow A_1'$	134.7	133.3	a
2 \rightarrow 3	$E' \rightarrow A_1'$	138.8	139.9	141
3 \rightarrow 4	$A_1' \rightarrow A_1'$	117.6	116.2	118
3 \rightarrow 4	$E' \rightarrow E'$	126.7	125.3	129
3 \rightarrow 4	$E' \rightarrow E'$	161.7	165.6	166?
3 \rightarrow 4	$A_1' \rightarrow A_1'$	96.5	93.1	b
3 \rightarrow 4	$A_1' \rightarrow E'$	105.4	102.2	b
3 \rightarrow 4	$A_1' \rightarrow E'$	140.5	142.5	143
3 \rightarrow 4	$A_1' \rightarrow A_1'$	91.7	86.6	b
3 \rightarrow 4	$A_1' \rightarrow E'$	100.7	95.7	b
3 \rightarrow 4	$A_1' \rightarrow E'$	135.8	135.9	c
Barrier height (cm^{-1})	---	864	755	---

^a Obscured by 0 \rightarrow 1.

^b Not observed.

^c Obscured by 1 \rightarrow 2($E' \rightarrow E'$).

Table 5. Observed and Calculated ν_7 Transitions for VF_5 .

Transition	Symmetry	Calculated (cm^{-1}) B = 0.08	Calculated (cm^{-1}) B = 0.09	Observed (cm^{-1})	
				Infrared ^a	Raman ^b
0 \rightarrow 1	A' \rightarrow E'	107.4	197.3	---	108
1 \rightarrow 2	E' \rightarrow A ₁ '	96.8	94.0	91.9	93
1 \rightarrow 2	E' \rightarrow E'	109.4	109.4	109.4	108
2 \rightarrow 3	A ₁ ' \rightarrow E'	99.3	97.0	98.1	100
2 \rightarrow 3 R	A ₁ ' \rightarrow A ₁ '	119.5	119.5	c	120
2 \rightarrow 3 R	A ₁ ' \rightarrow A ₁ '	126.6	131.6	c	126, 120
2 \rightarrow 3	E' \rightarrow E'	86.7	81.6	85.8	5, 83
2 \rightarrow 3	A ₁ ' \rightarrow A ₁ '	107.0	104.2	103.6	---
2 \rightarrow 3	E' \rightarrow A ₁ '	114.0	116.2	---	114
Barrier height (cm^{-1})	---	539	428	---	---

^a Reference 5.^b There are additional Raman features which can be attributed to 3 \rightarrow 4 transitions. Limitations in our calculations did not enable us to determine these transitions.^c Only Raman active.

Table 6. Correlation Table for D_{3h} - G_{324} and for $B(CH_3)_3$

Point Group			Molecular Symmetry Group			
D_{3h}			G_{324}			
Species	Vibration	Activity	Mode	Vibration	Species	Activity
A_1	1	R(p)	CH_3 stretch	1	A_1	R(p)
	2		CH_3 deformation	2		
	3		BC_3 stretch	3		
A_2'	4	IA	CH_3 stretch	4	A_4	IA
	5		CH_3 deformation	5		
	6		CH_3 rock	6		
A_2''	7	IR	CH_3 stretch	7	A_3	IR
	8		CH_3 deformation	8		
	9		CH_3 rock	9		
	10		BC_3 deformation	10		
E'	11	IR,R	CH_3 stretch	11	I	IR,R
	12		CH_3 stretch	12		
	13		CH_3 deformation	12		
	14		CH_3 deformation	13		
	15		BC_3 stretch	14		
	16		CH_3 rock	15		
	17		BC_3 deformation	15		
E''	18	IR,R	CH_3 stretch		E_2	IR,R
	19		CH_3 deformation			
	20		CH_3 rock			

Table 7. Vibrational Assignment of $B(CH_3)_3$ According to G_{324} MS Group

<u>Species</u>	<u>Vibration</u>	<u>IR</u>	<u>Raman</u>	<u>Inactive (Estimate)</u>
A_1	1		2916	
	2		1291	
	3		678	
A_2	4			2915
	5			1400
	6			900
A_3	7	2914		
	8	1303		
	9	975		
	10	326		
I	11	2984	2985	
	12	1450	1445	
G	13	867	868	
E_2	14	1184 ^a	1162	
		1154		
	15	310	314	

^a ^{10}B , ^{11}B isotopic splitting

Studies of the Reactions of $M(g) + SO_2$

S. Abramowitz and L.W. Sieck

The matrix isolated infrared spectra of the products of reactions of $M(g)$ where $M = {}^7Li, {}^6Li, Na$ and K with $SO_2(g)$ have been observed. Most of the effort has been directed towards the $Li + SO_2$ system. Absorption bands in these spectra have been assigned to a symmetric and asymmetric stretching mode of SO_2^- . There are other absorption bands in the spectra which are due to $M-SO_2$ motions. Isotopic studies utilizing $S^{18}O_2$ and $S^{16}O^{18}O$ as well as 6Li and 7Li are expected to elucidate the structure of the MSO_2 species. In particular we are hopeful that our results can indicate whether the M is bonded to the S or O_2 .

The results of this study will enable the calculation of the thermodynamic properties of the MSO_2 species. Species such as these may be important in the corrosion of turbine blades by high temperature gases containing sulfur oxide species and trace metals.

DATE
FILME
—8